Post-Seismic Deformation Related to the 2016 Central Italy Seismic Sequence from GPS Displacement Time-Series

Eugenio Mandler[1], Letizia ANDERLINI[2], Adriano Gualandi[2], Francesco Pintori[2], Enrico Serpelloni[2], and Maria Elina Belardinelli[1]

[1]University of Bologna
[2]Istituto Nazionale di Geofisica e Vulcanologia

November 24, 2022

Abstract

The 2016-2017 Central Italy earthquake sequence struck the central Apennines between August 2016 and October 2016 with Mw [?] [5.9; 6.5], plus four earthquakes occurring in January 2017 with Mw [?] [5.0; 5.5]. Here we study Global Positioning System (GPS) stations active during the post-seismic phase including near and far-field domains. We separate the post-seismic deformation from other, mainly seasonal, hydrological deformation signals present in ground displacement time-series via a variational Bayesian Independent Component Analysis technique. For each component, realistic uncertainties are provided to the related ICA-reconstructed displacement field. We study the distribution of afterslip on the main structures surrounding the mainshock, and we highlight the role played by structures that were not activated during the co-seismic phase in accommodating the post-seismic deformation. In particular, we report aseismic deformation occurring on the Paganica fault, which hosted the Mw 6.1 2009 L'Aquila earthquake, and is located further south of the 2016-2017 epicenters; and on a 2-3 km thick subhorizontal shear-zone, clearly illuminated by seismicity, which bounds at depth the west-dipping normal faults where the mainshocks nucleated. Since afterslip alone underestimates the displacement in the far-field domain, we consider the possibility that the shear zone marks the brittle-ductile transition, assuming the viscoelastic relaxation of the lower crust as a mechanism contributing to the post-seismic displacement. Our results suggest that multiple deformation processes are active in the first two years after the mainshocks.

Post-Seismic Deformation Related to the 2016 Central Italy Seismic Sequence from GPS Displacement Time-Series

E. Mandler[1],L. Anderlini[2], A. Gualandi[3],F. Pintori[3], E. Serpelloni[3] and M. E. Belardinelli[3]

1: Dipartimento di Fisica e Astronomia, Settore di Geofisica, Università di Bologna, Bologna, Italy

2: Istituto Nazionale di Geofisica e Vulcanologia (INGV), Bologna, Italy,

3: Istituto Nazionaledi Geofisica e Vulcanologia (INGV), Osservatorio Nazionale Terremoti, Italy

Authors' contacts:

Eugenio Mandler: eugenio.mandler2@unibo.it (ORCID: https://orcid.org/0000-0002-2928-0566)

Letizia Anderlini: letizia.anderlini@ingv.it (ORCID: https://orcid.org/0000-0002-9461-3320)

Adriano Gualandi: adriano.gualandi@ingv.it (ORCID: https://orcid.org/0000-0002-3100-8932)

Francesco Pintori: francesco.pintori@ingv.it (ORCID: https://orcid.org/0000-0001-7465-6297)

Enrico Serpelloni: enrico.serpelloni@ingv.it (ORCID: https://orcid.org/0000-0003-1822-403X)

Maria Elina Belardinelli: mariaelina.belardinelli@unibo.it (ORCID: https://orcid.org/0000-0002-7653-5090)

Key Points:

- We study the post-seismic deformation following the 2016-2017 Central Italy seismic sequence through GPS displacement time series

- We map the afterslip distribution on faults co-seismically activated and we investigate interaction among faults
- We infer the occurrence of multiple post-seismic deformation mechanisms including afterslip and viscoelastic relaxation

Abstract

The 2016-2017 Central Italy earthquake sequence struck the central Apennines between August 2016 and October 2016 with $Mw \in [5.9; 6.5]$, plus four earthquakes occurring in January 2017 with $Mw \in [5.0; 5.5]$. Here we study Global Positioning System (GPS) stations active during the post-seismic phase including near and far-field domains. We separate the post-seismic deformation from other, mainly seasonal, hydrological deformation signals present in ground displacement time-series via a variational Bayesian Independent Component Analysis technique. For each component, realistic uncertainties are provided to the related ICA-reconstructed displacement field. We study the distribution of afterslip on the main structures surrounding the mainshock, and we highlight the role played by structures that were not activated during the co-seismic phase in accommodating the post-seismic deformation. In particular, we report aseismic deformation occurring on the Paganica fault, which hosted the Mw 6.1 2009 L'Aquila earthquake, and is located further south of the 2016-2017 epicenters; and on a $\sim$2-3 km thick subhorizontal shear-zone, clearly illuminated by seismicity, which bounds at depth the west-dipping normal faults where the mainshocks nucleated. Since afterslip alone underestimates the displacement in the far-field domain, we consider the possibility that the shear zone marks the brittle-ductile transition, assuming the viscoelastic relaxation of the lower crust as a mechanism contributing to the post-seismic displacement. Our results suggest that multiple deformation processes are active in the first two years after the mainshocks.

1. Introduction

The 2016 Amatrice-Visso-Norcia earthquake sequence started on August, 24 when a Mw 6.0 event struck a sector of the Central Apennines (Figure 1) characterized by a narrow band of

measurable geodetic and seismic deformation rates (D'Agostino, 2014; Sani et al., 2016; Barani et al., 2017). It caused hundreds of deaths and considerable damage to the town of Amatrice and its surroundings (Pucci et al., 2017; Figure 1). The seismicity that followed the mainshock was recorded both northwest and southeast of the epicenter (Chiaraluce, Di Stefano, et al., 2017), with decreasing magnitude and frequency, until when a Mw 5.9 event occurred on October 26, about 25 km to the NW of Amatrice's earthquake epicenter, near the village of Visso (Figure 1). On October 30, the largest event of the seismic sequence (Mw 6.5) occurred near the town of Norcia, involving a portion of the fault system between the two preceding events which had previously been left unruptured (Cheloni et al., 2017). The seismic sequence continued on January, 18 2017 with four 5≤ Mw≤ 5.5 earthquakes that ruptured the Campotosto fault, southeast of the Amatrice event (Xu et al., 2017 ; Cheloni et al., 2017).

The main events show normal faulting mechanisms (http://cnt.rm.ingv.tdmt; Figure 1) in agreement with the SW-NE extension of ~3–4 mm/yr that characterizes this area (D'Agostino, 2014; Barani et al., 2017; Devoti et al., 2017), and with the presence of several NW-SE trending active normal faults (Boncio et al., 2004; Galli et al., 2008; Pizzi and Galadini, 2009).

The area has been repeatedly struck by 5.2 < Mw < 6.2 earthquakes in the last 400 years (Rovida et al., 2019; Figure 1). Fault segments responsible for the mainshocks of this seismic sequence involved a portion of a fault system as long as 80 km along strike (Figure 1; Michele et al., 2020). Importantly, the 2016 Central Italy sequence is bounded to the north by the fault system responsible for the Colfiorito 1997 seismic sequence (Chiaraluce et al., 2003; Amato et al., 1998; Boncio & Lavecchia, 2000; Ferrarini et al., 2015), and to the south by the one responsible for the 2009 L'Aquila earthquake (Chiaraluce, 2012; Lavecchia et al., 2012; Valoroso et al., 2013). Therefore these recent earthquake sequences can be interpreted in the light of a 150 km long normal fault system, made up of 10–30 km long segments, separated by crosscutting compressional structures inherited from the pre-Quaternary compressional tectonics (Pizzi and Galadini, 2009).

The bulk of geological (e.g., Civico et al., 2018; EMERGEO Working Group, 2016; Falcucci et al., 2016; Galadini et al., 2018; Pizzi et al., 2017; Villani et al., 2018), seismological (Chiaraluce, Di Stefano, et al., 2017; Papadopoulos et al., 2017; Pizzi et al., 2017; Scognamiglio et al., 2018; Tinti

et al., 2016), and geodetic (Cheloni et al., 2017; Huang et al., 2017; Lavecchia et al., 2016; Walters et al., 2018; Wang et al., 2018; Xu et al., 2017) observations, collected soon after the Amatrice mainshock, agree in showing that each mainshock broke different, slightly off-axis, segments of a SW dipping normal fault system, aligned along the Apennines chain. Moving from north to south two main normal fault segments can be detected, respectively the Mt. Vettore-Mt Bove and the Mt. della Laga (also known as the Gorzano fault), separated by the Pliocene Sibillini thrust (Figure 1).

Although the segmentation of the fault system is not unequivocally determined, the faults that ruptured during the Amatrice-Visso-Norcia sequence are rather well defined. Most of the studies (Chiaraluce, Di Stefano, et al., 2017; Cheloni et al., 2017, Cheloni et al., 2019; Xu et al., 2017; Walters et al., 2018) suggest the activation of a fault system $\sim$60-70 km-long, 157°-164° striking and 39°-50° dipping. Some studies (Xu et al., 2017; Cheloni et al., 2019) propose coseismic slip models on a single plane for the main fault, while others (Chiaraluce, Di Stefano, et al., 2017; Cheloni et al., 2017; Walters et al., 2018) divide such fault plane into 3-4 segments which are consistent in terms of strike and dip. The Amatrice event was characterized by a bilateral rupture (Lavecchia et al., 2016; Tinti et al., 2016; Cheloni et al., 2017; Xu et al., 2017; Chiaraluce, Di Stefano, et al., 2017) on the southern portion of the Amatrice-Visso-Norcia fault system between the M. Vettore and the Gorzano faults, with maximum slip $\sim$1 m . Such event may have possibly activated the Campotosto fault in the area struck by the January 2017 earthquakes (Xu et al., 2017). The Visso earthquake nucleated on the northernmost portion of the Amatrice-Visso-Norcia fault system with a maximum slip of $\sim$0.6-1 m occurring at a depth of 3-6 km (Xu et al., 2017; Chiaraluce, Di Stefano, et al., 2017; Cheloni et al., 2017; Walters et al., 2018). The Norcia earthquake filled the gap on the fault system left by the previous events with ruptures extending southwards up to the area already activated during the Amatrice event (Xu et al., 2017; Cheloni et al., 2019; Scognamiglio et al., 2018). As regards the coseismic slip distributions, most of the studies (Cheloni et al., 2017, 2019; Chiaraluce, Di Stefano, et al., 2017; Walters et al., 2018; Xu et al., 2017; Scognamiglio et al., 2018) present similar solutions in terms of slip location (Cheloni et al., 2019) and peaks of maximum slip ($\sim$2.5-3 m) in the shallower portion of the fault ($\sim$0-6 km), consistently with the observed surface ruptures (Xu et al., 2017); nevertheless some of them (Cheloni et al., 2017, 2019) allow considerable slip deeper than that. Cheloni et al. (2017, 2019),

Walters et al. (2018), Scognamiglio et al. (2018) invoke for the Norcia earthquake the activation of multiple secondary faults. In particular, a fault antithetic to the M. Vettore fault, well highlighted by the seismicity (Chiaraluce, Di Stefano et al., 2017) with a steep dipping angle (~65°), striking ~336° N (Cheloni et al., 2017, 2019; Walters et al., 2018). Cheloni et al. (2017), Walters et al. (2018) and Scognamiglio et al. (2018) include in their solution a ~210°-220°N striking, ~35° - 40° dipping additional secondary fault, possibly connecting in its deepest part with the Sibillini thrust and suggesting its reactivation (Scognamiglio et al., 2018; Cheloni et al., 2017). However, more recent studies (Cheloni et al., 2019; Pousse-Beltran et al., 2020) suggest that requiring the activation of such an oblique structure to explain the seismic sequence is an unnecessary addition of complexity, as the main fault system plus a series of antithetic faults is sufficient to explain the complex displacement pattern observed.

The comparison between the subsurface geology with the seismological data (e.g., Porreca et al., 2018) shows that most of the instrumental background seismicity recorded after the 1997 and 2009 seismic sequences is confined within the sedimentary succession, as suggested by Chiaraluce, Barchi, et al. (2017). Importantly, the normal fault system downdip extension is limited within the first 8-10 km of the upper crust, being bounded at depth by an east-dipping, ~2-3 km thick layer of seismicity that hosted a series of small to moderate aftershocks (≈Mw 4), which might be involved in the loading of the higher angle faults above and might mark the decouplement between the upper and lower crusts (Chiaraluce, Di Stefano, et al., 2017; Vuan et al., 2017). How this layer of seismicity, the position of the underlying basement (between a depth of 8 and 11 km), and the abrupt cut-off of seismicity relate is still to be understood. Following previous authors (e.g. Chiaraluce, Di Stefano, et al., 2017; Vuan et al., 2017; Michele et al., 2020) we will refer to such a thick layer of seismicity as “shear zone”.

The post-seismic phase of the 2016 Central Italy sequence has been studied by Pousse-Beltran et al. (2020), who used Interferometric Synthetic Aperture Radar (InSAR) time-series to detect and model post-seismic deformation, focusing on the near-field response (< 50 km). In such study, two subsidence areas are detected: the first one in the Castelluccio basin and the second one nearby the town of Arquata. Due to inconsistencies between the observed and the modeled displacement, poroelastic and viscoelastic mechanisms are ruled out as the main sources of the post-seismic displacement pattern (Pousse-Beltran et al., 2020). However, since subsidence in the Castelluccio

basin is poorly explained by afterslip too, they do not rule out the possibility that those mechanisms and/or the activation of the shear zone may have contributed to the displacement observed in that area. On the other hand, the logarithmic-like evolution of the displacement in the InSAR time-series in the Arquata area validates the hypothesis of afterslip as the driving mechanism (Pousse-Beltran et al., 2020). The best slip distribution they retrieve requires the activation of the M. Vettore fault (as modeled by Cheloni et al., 2017) and of an antithetic fault (as modeled by Cheloni et al., 2019; Maubant et al., 2017). Post-seismic slip reaches its maximum (~10 cm) at shallow depth (0- 2 km) below Arquata del Tronto at the edge of the coseismic asperities; slip in the Castelluccio basin reaches its maximum (~16 cm) at ~5 km depth, partly overlapping with the Norcia coseismic rupture area. In this study we consider ground displacement time-series obtained from the analysis of GPS stations distributed over a wide region, including also far-field stations, and we apply a blind-source-separation algorithm to characterize the temporal evolution and spatial features of the post-seismic deformation signal across the 2016-2017 epicentral area. This kind of analysis has proved to be effective in separating tectonic signals from other signals present in the data set that may mask it (e.g. Michel et al., 2018; Gualandi et al., 2020). The paper is organized as follows: in Section 2 we describe the GPS dataset used and the results of the Independent Component Analysis (ICA) applied to the GPS displacement time-series; in Section 3 we interpret the retrieved non postseismic signals as due to hydrological sources; in Section 4 we obtain, by inverting the GPS time series, the distribution of afterslip and show a possible viscolastic contribution to the measured geodetic, far field, displacements; in Section 5 we discuss the findings of this study and in Section 6 conclusions are drawn.

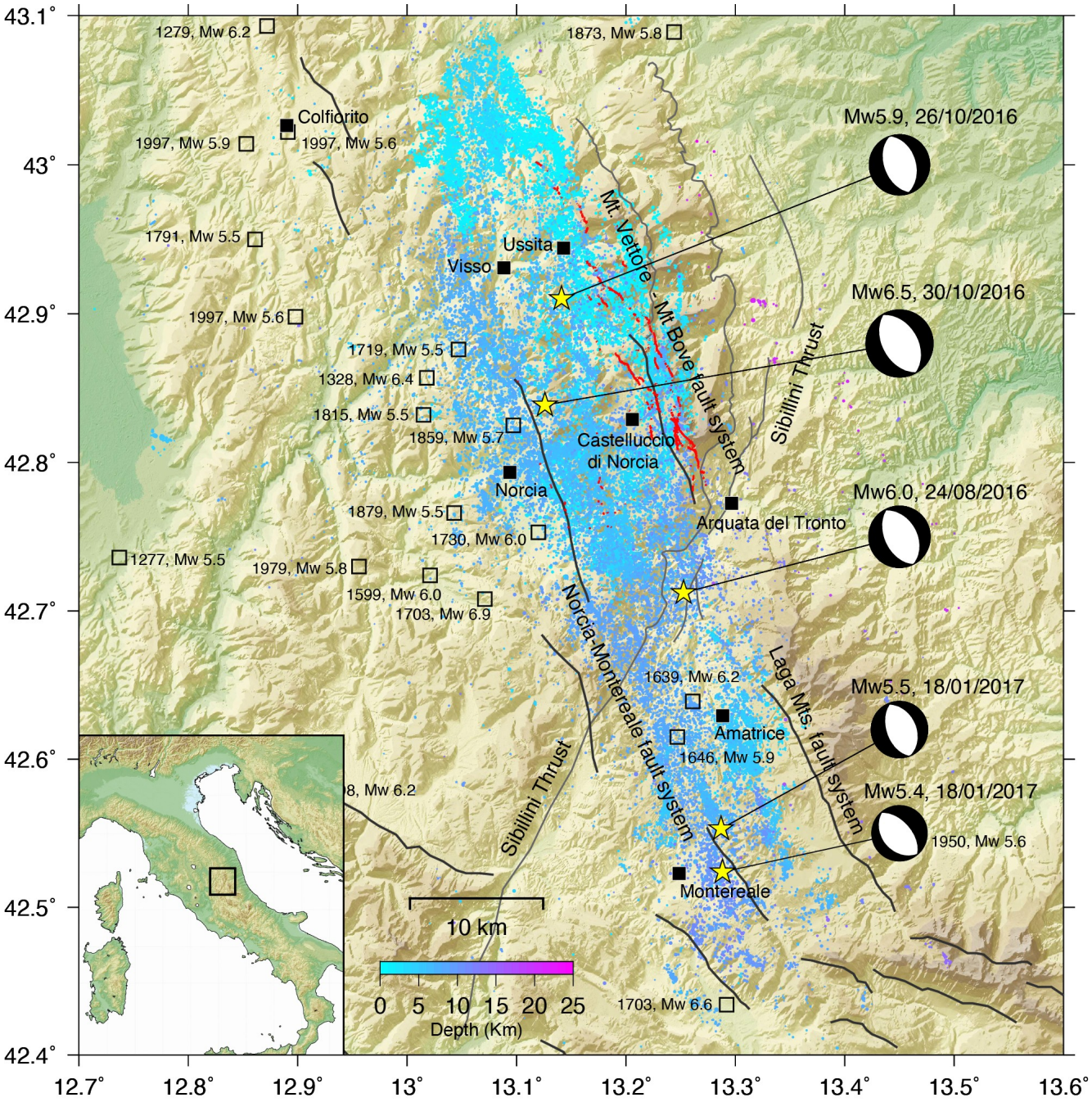

Figure 1. Map showing the major events of the 2016-2017 Central Italy sequence (yellow stars), the focal mechanism (from Michele et al., 2020) and the historical seismicity (squares), for earthquakes with equivalent 5.4≤Mw (from CPTI15, V.2.0, https://emidius.mi.ingv.it/CPTI15-DBMI15). Colored dots represent the seismicity recorded after August 24 (from Michele et al., 2020), plotted as a function of depth. The red lines represent ground ruptures associated with the Amatrice and Norcia mainshocks (from Civico et al., 2018). The black and grey lines show the

trace of the major normal faults and of the Sibillini thrust, respectively.

2. GPS Data and Time-Series Analysis

Figure 2 shows the GPS stations considered in this work. Since we are interested in measuring the continuous slow deformation process occurring after the Amatrice mainshock, we have considered mainly GPS stations with almost continuous data in the time-interval 2012-2019, which have been integrated by a few campaign-mode stations, belonging to the CaGeoNet network (Galvani et al., 2013), that have been occupied almost continuously after the Amatrice mainshock (see Cheloni et al., 2016 for details). We also included a few stations in the Adriatic off-shore, which are managed by ENI and presented by Palano et al. (2020). This data-set also includes new continuous stations installed as emergency response soon after the Amatrice and Norcia mainshocks. The position time-series have been obtained following the procedure described in Serpelloni et al. (2006, 2013, 2018), consisting in: raw phase data reduction; combination of loosely constrained network solutions and definition of the reference frame; time-series analysis, including velocity estimates, spatial filtering of common mode errors and co-seismic and instrumental offsets removal. The details of the processing and post-processing procedures are described in the supplementary material (Section S1.1.). The time-series used in this work are part of a continental-scale geodetic solution, including >3500 continuous GPS stations and the spatial filtering has been applied at a continental-scale, following Serpelloni et al. (2013, 2018), excluding all GPS stations affected by earthquakes, thus preventing the removal of the localized geophysical signals recorded by the GPS stations in the study area.

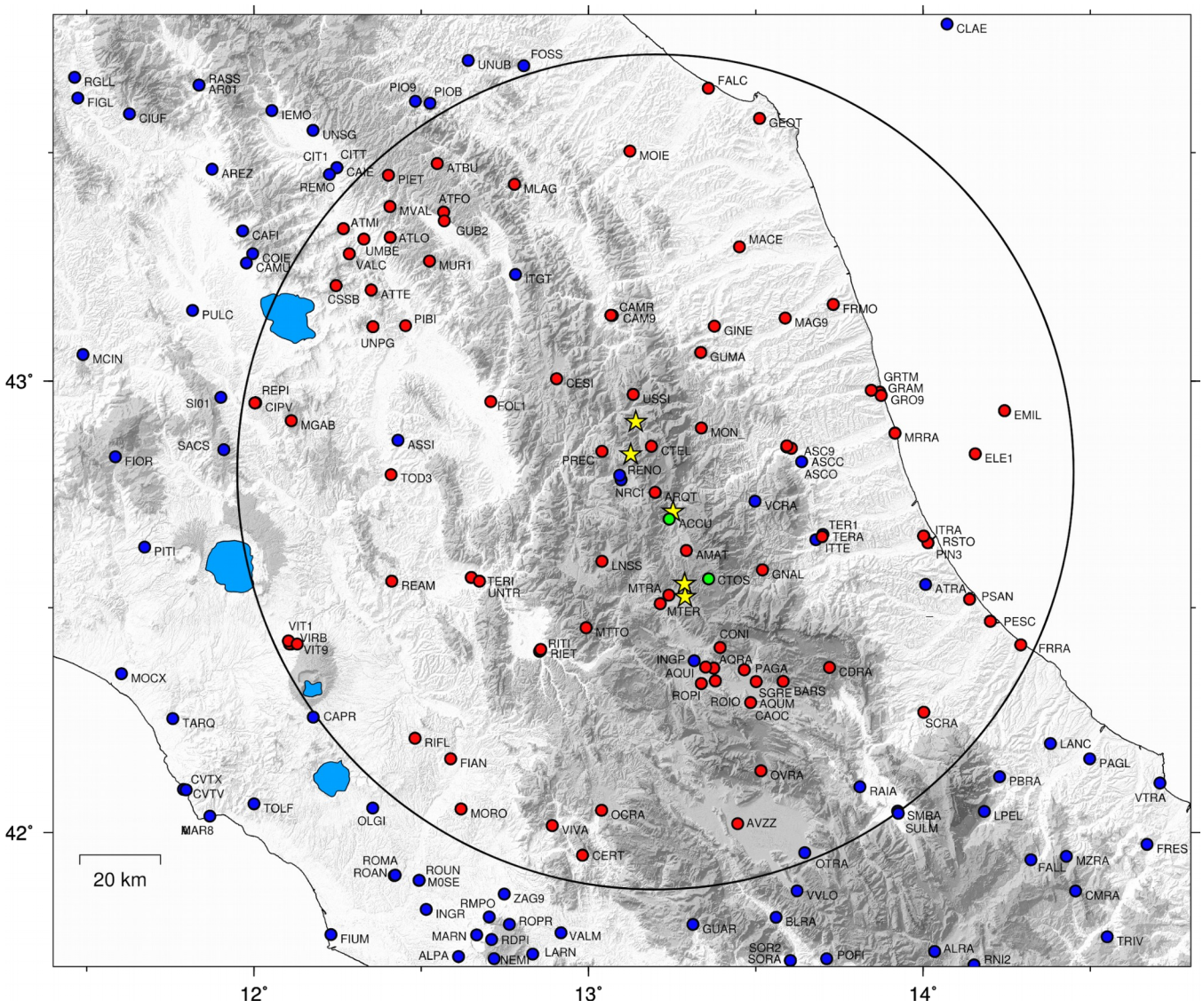

Figure 2. Colored circles show the GPS stations considered. The blue circles show the positions of the continuous GPS stations present in this area and for which we analyze the raw data as described in Section 2. Among the whole GPS network, the red circles show the position of the continuous GPS stations used in the blind source separation analysis with the vbICA method (Section 2.1), namely stations within a of radius = 100 km from the epicentral area having almost continuous observations after the Amatrice earthquake. The green circles show the position of the two non-permanent GPS stations, belonging to the CaGeoNet network, included also in the vbICA. The yellow stars show the epicenters of the mainshocks of the 2016-2017 seismic sequence, as in Figure 1.

2.1 Blind Source Separation

Given a certain number M of displacement time series relative to sensors distributed at different locations in space, we can organize the data into a spatio-temporal matrix X. In particular, we organize it in such a way that each row is a different time series, and each column represents the record at a given time or epoch. The data at our disposal has a daily sampling in time and spans the time range 2012 to 2019. The total number of stations used in the analysis is 85. Since we have three dimensional records (east, north and vertical), the matrix X has size M x T = 255 x 2525. The observations consist of the surface displacement, which are the result of multiple processes active at the same time at different spatial and temporal scales. The proper modeling of these various contributions is an active research domain of solid Earth sciences. In practice, we would like to be able to isolate the deformation relative to the various mechanisms contributing to the observations. In this sense we are facing a so-called blind source separation problem. A well established approach to deal with this problem consists in the application of multivariate statistical techniques that attempts to maximize the independence of the sources generating the observations. The techniques fall under the umbrella of the Independent Component Analysis and typically consist in a linear decomposition of the data into a mixing matrix A (MxL) and a source matrix S (LxT), with the L sources (components) being as much independent as possible. We can cast the problem in the following terms:

$$X=AS+N \quad (1)$$

where N is noise (typically Gaussian). We underline here that the equality holds if we were using a number of components L sufficient to span the whole original space where the data X lives. Most of the times a truncation is performed, i.e. $L < \min\{M,T\}$, and the right hand side is a low-rank approximation of the left hand side (e.g., Kositsky & Avouac, 2010). Moreover, we notice that we are performing a linear decomposition of the spatio-temporal matrix, i.e. the spatial and temporal information can be splitted and encoded in the matrices A and S, respectively. Each row of S contains a different source. The ICA attempts to find these sources imposing them to be statistically independent. Given the way we have built X, we are performing the decomposition in so-called T-mode, i.e. we attempt to find sources that are independent in the time domain. We underline here that one of the strengths of these techniques consists in the fact that they are data

driven and do not impose any specific prescribed functional form to the underlying sources that we want to investigate. In fact, ICA techniques belong to the so-called unsupervised learning approaches to pattern recognition.

Unfortunately, the independence condition is not straightforward to impose and approximations are introduced in order to generate a suitable cost function to minimize or maximize. Several approaches have been proposed, and here we use a variational Bayesian ICA (vbICA). It has been shown that this method is superior to other widely used ICA techniques because it offers more flexibility in the description of multimodal sources and it allows to take into account missing data (e.g., Roberts & Choudrey, 2003; Chan et al., 2003). We use the version adapted to the study of geodetic time series by Gualandi et al. (2016). We adopt a notation similar to that used in Gualandi et al. (2016), where each IC is characterized by a specific spatial distribution (U) and a temporal evolution (V). A weight coefficient Σ (in mm) is requierd to rescale the contribution of each component in order to explain the original displacement dataset. Since the vbICA belongs to the field of linear decompositions, we can write the result of the decomposition of the data matrix X as:

$$X_{MxT} = U_{MxL} \quad \Sigma_{LxL} \, V_{LxT}^{T} \tag{2}$$

U_{MxL} embeds the spatial response of the *M* time-series to the *L* sources of displacement; V_{LxT} embeds the temporal evolution of the *L* sources; Σ_{LxL} is a diagonal matrix containing the relative importance of the different ICs in explaining the displacement dataset (in mm). The configuration is such that we look for independent signals in the time domain, i.e. the sources correspond to the columns of the V matrix while the mixing matrix is given by the product $U\Sigma$. The vbICA algorithm models the probability density function of each source via a mix of Gaussian distributions (4 in this case, as suggested by Choudrey, 2002), retrieving the spatial and temporal information of the independent sources of deformation. We exclude from this analysis all stations without data after the Amatrice mainshock and stations with large data gaps (>90%) across the 2016-2017 earthquake sequence. The sufficient number of sources (L) is determined performing some statistical tests such as the χ^2, *F-test* (Kositsky & Avouac, 2010) or the *ARD test* (Choudrey, 2002; Gualandi et al., 2016). We perform the decomposition with a number of ICs *L = 3, 4, 5, 6,* and the *ARD test* limited L≤5. An estimation of the goodness of the decomposition is given by the χ^2_{red}

which is respectively 1.53, 1.48 and 1.50 for *L = 3, 4, 5*. In order to assess if these values are significantly different one another we perform the *F-test* on the χ^2. The *F-test* between the 3 ICs and 4 ICs provides *F=1.66,* while between 4 and 5 components it provides *F=0.79.* The comparison between these values and the critical value at a 95 % level of confidence (*F-critical= 1.02*) suggests to retain 4 components, and such configuration is the one we investigate.

vbICA also provides an estimate of the uncertainty associated with each independent component (IC), that however generally results to be underestimated. In order to better assess the uncertainties associated with the ICs we run a Monte Carlo simulation generating synthetic datasets resembling the original one and performing a decomposition on each synthetic dataset. From the U, Σ and V distributions we obtain a more realistic estimate of the uncertainties associated with the decomposition. We detail the procedure in Section S.1.2. of the Supporting informationl. The temporal evolution of the four ICs (V) is shown in Figure 3, together with the corresponding power spectral density. The ICA decomposition results in: *(i)* a post-seismic relaxation signal (IC1); *(ii)* two components with annual periodicity (IC2 and IC4); *(iii)* a multiannual component (IC3). From the spectral analysis it is clear that low frequencies are the most significant for the post seismic and the multiannual IC and that the dominant periodicity is about 1 year for the annual components. However the IC4 shows a second peak at low frequencies as well. The spatial response of the four ICs (U) is shown in Figure 4. From Figure 4 the NE-SW main direction of the U1 spatial pattern is rather clear, consistently with the extensional mechanisms of the seismic sequence. U2 shows a clear vertical motion, with all stations moving coherently up and down with annual periodicity, whereas U3 and U4 show more complex horizontal, and secondly vertical, spatial patterns. In the next section we will provide a physical explanation for the second, third and fourth components, whereas the first component will be discussed in Section 4.

We also investigate the pre-seismic phase, limiting the analysis to the 2015-2016.64 (i.e. the 24th of August) time-interval as in Vičič et al. (2020), in order to detect possible deformation signals that can be associated with the preparatory phase of the 2016 earthquake sequence. According to an F-test the most suitable decomposition is the one with L=4 components; we carry out the decomposition on the whole GPS network (see Figure 2). The results, reported in the supplementary material (S2), show that the temporal and spatial parts of the independent components retrieved in this time span do not highlight any localized deformation that can be

associated with a clear tectonic strain transient such as the sudden rise at the beginning of 2016 described by Vičič et al. (2020).

300

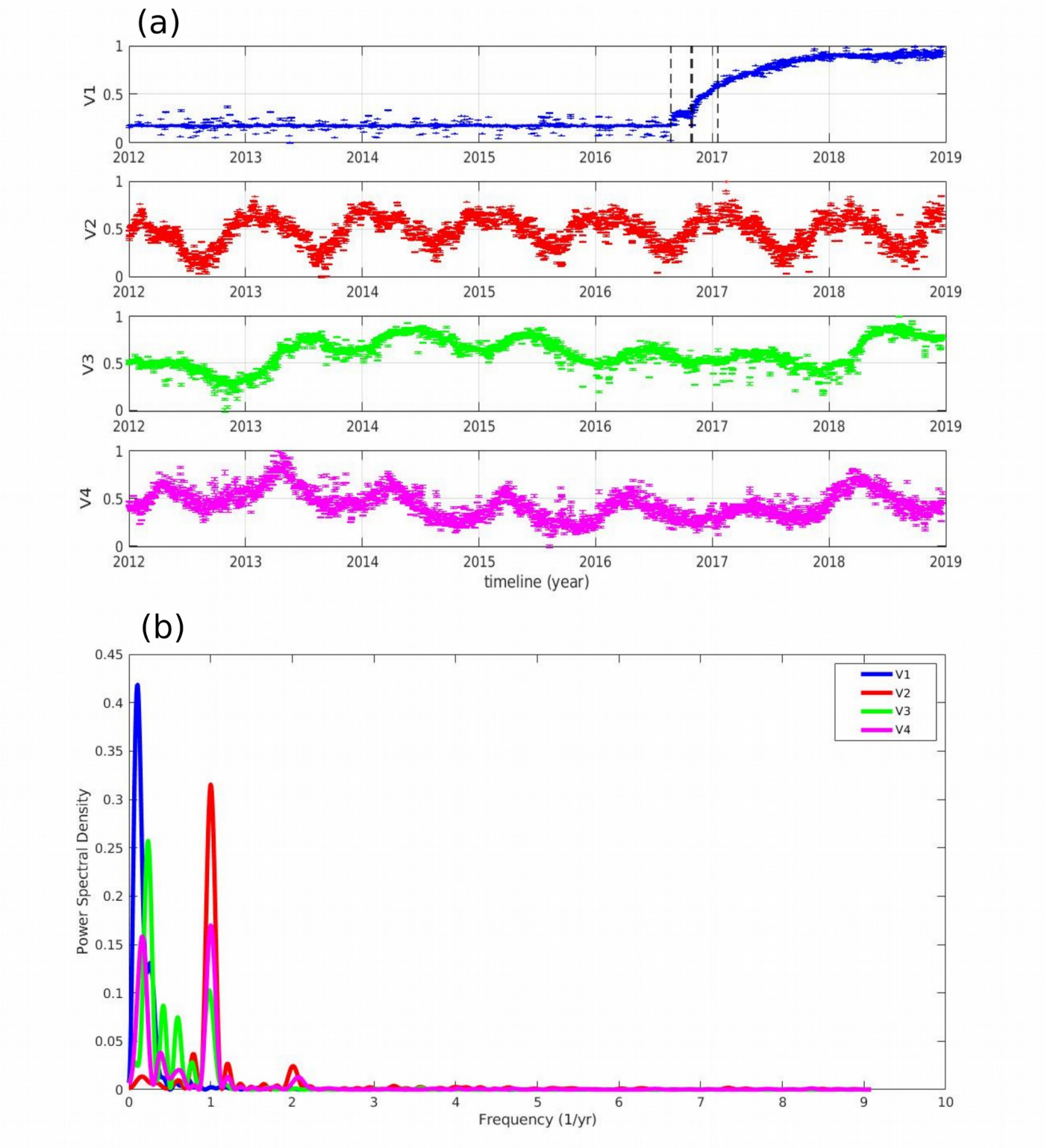

Figure 3. (a) The temporal evolution V of the four independent components (vertical dashed lines for V1 mark the Amatrice, the Visso-Norcia and the January 2017 Campotosto earthquakes) and

(b) their corresponding power spectral density plots.

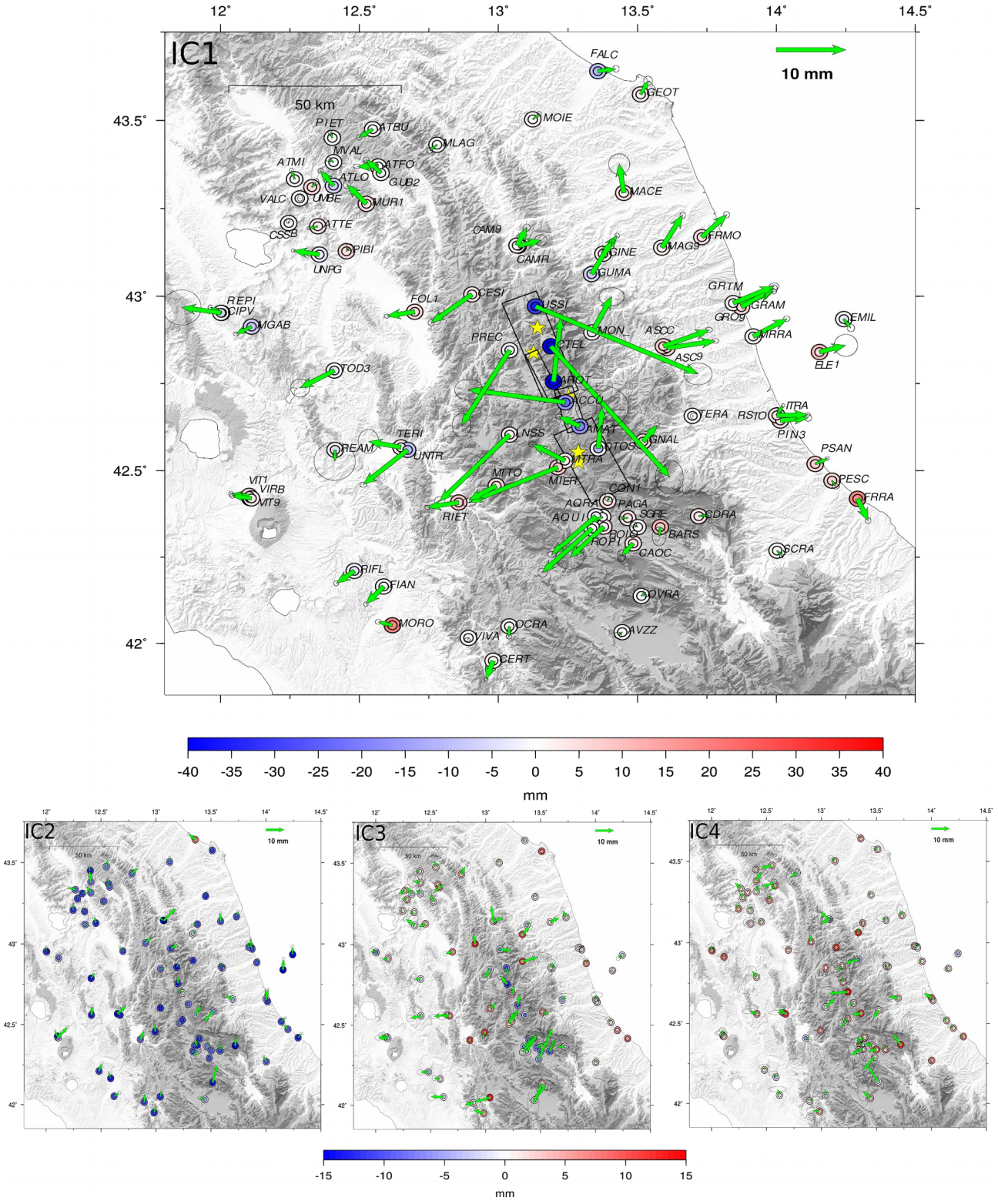

Figure 4. In Figure the dimensional spatial components (Σ U) of the IC_1 ,IC_2 ,IC_3 ,IC_4 , with the

15

corresponding temporal functions being normalized between 0 and 1 (Figure 3a). Green arrows mark the horizontal response in mm; outer colored circles mark the vertical response +σ while inner colored circles mark the vertical response -σ of the GPS stations (in mm). Yellow stars mark the location of the main events of the seismic sequence (as in Figure 1), while the black boxes in IC1 show the location of the faults responsible for the 2016-2017 sequence as in Cheloni et al. (2017, 2019).

3. Hydrological components

In this section we discuss the deformation signals associated with the second, third and fourth ICs (Figure 3 and 4), providing physical explanations for these signals. In particular, we test the hypothesis that IC2, IC3 and IC4 are associated with different hydrological processes. These processes can evenly affect the entire network or be very sensitive to the geologic features of the area; furthermore, the impact on vertical and horizontal components can be variable too. Because of the multi-annual temporal signature of IC3, separating this signal from the post-seismic deformation one is also important in order to improve the accuracies of the retrieved pre- and post-seismic displacements, particularly in case these are expected to be rather small.

IC2 represents a common mode annual signal, with a uniform spatial response (i.e., all the GNSS stations move toward the same direction) in the vertical component. Seasonal vertical displacements are interpreted in the literature as caused by loading due to mass redistribution in the shallow Earth crust and surface (e.g., Amos et al., 2014; Argus et al., 2014; Borsa et al., 2014; Dong et al., 2002; Tregoning, 2005). IC2 describes large vertical seasonal displacements, with median amplitude of ~6.3 mm in the vertical component. In the horizontal components, IC2 is associated with much smaller annual displacements, where the median amplitudes are ~1.1 mm and 0.7 mm in the N-S and E-W direction, respectively. The IC2 vertical component describes uplift of the GNSS network as temperature rises, while when the temperature decreases the sites subside. Since the temporal evolution of IC2 is in phase with the temperature (see Figure 5) we do not exclude that monument thermal expansion may also have an effect on GPS height changes.

We compare the temporal evolution of IC2 with products of global reanalysis models estimating the redistribution of fluids at the Earth's surface. In particular, Figure 5 shows V2 compared to the temporal evolution of hydrological loading displacements estimated from the ERA-interim (European Centre for Medium-Range Weather Forecasts, ECMWF reanalysis) model (Berrisford et al., 2009; Dee et al., 2011), using predictions provided by http://loading.u-strasbg.fr (Gegout et al., 2010; see also Serpelloni et al., 2018 for a similar application), and with the sum of the soil moisture and the snow water equivalent in the first 2 m, estimated by GLDAS-Noah (Rodell et al., 2004). Clearly, V2 is temporally correlated with ERA-interim displacements and anti-correlated with soil moisture, suggesting that IC2 is associated with surface hydrological mass loading (SHL) processes.

We observe a strong agreement between vertical displacements associated with IC2 and the ones calculated from the ERA-interim dataset (Figure 5) both in terms of temporal evolution (Pearson correlation coefficient = 0.8, with no significant time lags between the two curves), and amplitude. In fact, the mean seasonal amplitude of the vertical displacements caused by surface hydrological loading according to the ERA-interim model is 5.1 mm, which is just 1.2 mm less than the median value of the seasonal displacement associated with IC2. As regard the horizontal displacements, the north component of the displacements associated with IC2 still well correlates with predictions from the ERA-interim model, which is however poor for the east-west displacements, as already observed in Serpelloni et al. (2018). This discrepancy is likely due to limitations of assuming an elastic spherical Earth model, which does not take into account lateral heterogenities of the Earth's elastic properties (Chanard et al., 2018).

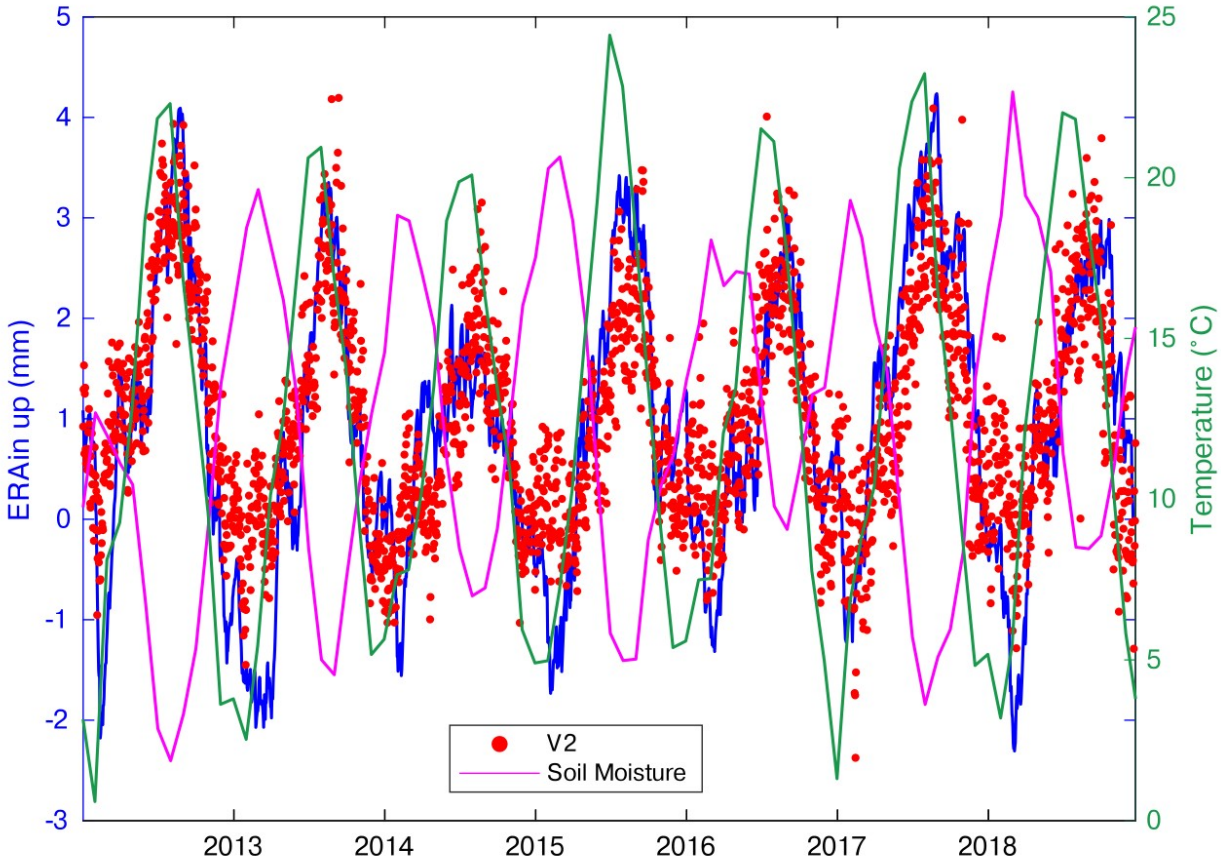

Figure 5. Red: V2 (sign reversed to indicate maximum uplift/subsidence during positive/negative peak values); Blue: mean vertical displacements caused by surface hydrological loading using the ERA-interim model (http://loading.u-strasbg.fr); magenta: soil moisture in the first 2 m estimated by GLDAS-Noah (Rodell et al., 2004); green: mean monthly temperature (GHCN Gridded data provided by the NOAA/OAR/ESRL PSL, Boulder, Colorado, USA, from their Web site at https://psl.noaa.gov/; (Fan & van den Dool, 2008). For all the datasets, we considered mean values in a box with limits: lon. 12.00-14.50 °E; lat. 42.00-44.00 °N.

As regards IC3, we test the hypothesis that this multi-annual deformation signal is associated with changes in groundwater content, as deformation associated with this process has been shown to affect the horizontal components of displacement with peculiar temporal and spatial signatures (e.g., Silverii et al., 2016; Serpelloni et al., 2018).

We use the lumped parameter hydrological model GR5J (Pushpalatha et al., 2011) to quantify daily total water storage (TWS) changes of 5 hydrological basins (Tevere, Nera, Tronto, Aterno, Pescara; see Section S3 in the supporting information for the map of the basins). Figure 6 shows TWS changes estimated for the 5 basins compared with V3 (see Table S1 for Pearson correlation coefficients and time lags) and with liquid water equivalent thickness (LWE), estimated by GRACE measurements processed at JPL using the Mascon approach (Version2/RL06, Watkins et al., 2015). Since there are only 5 GRACE-FO data available during the time period covered by GNSS time series, and the gap between GRACE and GRACE-FO is about 1 year, we do not consider GRACE-FO data to compute correlations between GRACE and V3.

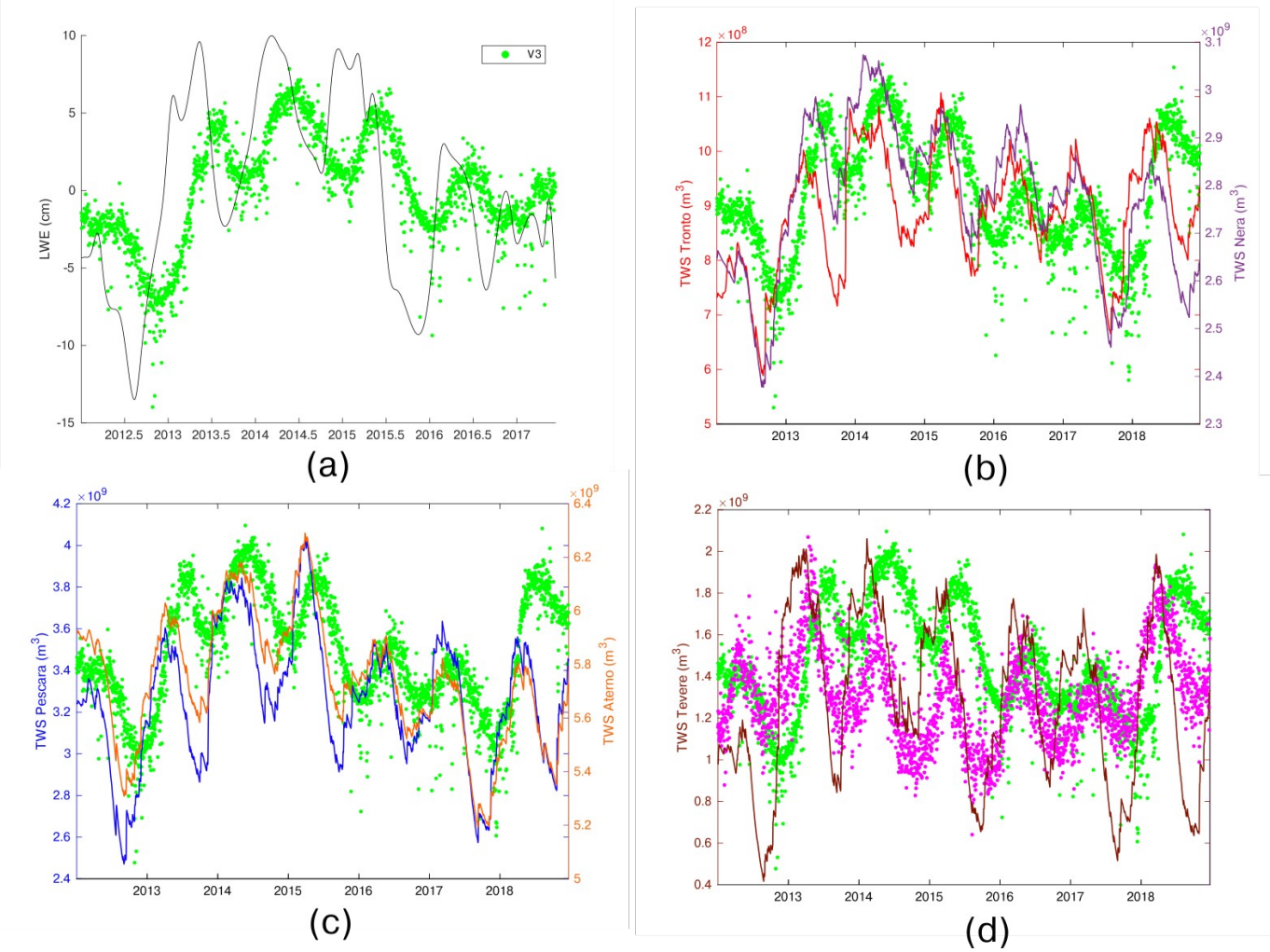

Figure 6. a) Comparison between LWE (in grey) from GRACE data and V3 (in green). Comparison between V3 and TWS changes computed in the hydrological basins (see Figure S3 in the supplementary material) of Tronto (in red) and Nera (in purple) (b), Pescara (in blue) and Aterno (in orange) (c). d) Comparison among TWS changes (in brown) computed in the Tevere basin and V3 (in green), V4 (in magenta).

LWE and TWS estimates do not take into account only the superficial water accumulation, as SHL models do, but also consider the effect of the deep waters. While SHL is almost spatially uniform, since it is mainly caused by the soil moisture, the accumulation of water at depth is much more heterogeneous, especially in carbonatic mountainous regions where significant groundwater flows are present.

20

A possible interpretation of IC2 and IC3 is that precipitation water, once removed the runoff and the evapotranspiration contributions, is partially absorbed by the first 1-2 m of soil, causing the displacements associated with IC2, which, in fact, are not significantly delayed with respect to the displacements caused by SHL. The remaining portion of precipitation may penetrate, depending on the hydro-geological properties of the subsurface, hundreds of meters until reaching a less permeable layer, accumulating water and causing the ground displacements associated with IC3. The duration of this percolation process causes a temporal delay between TWS variations and the displacements caused by it (i.e displacements associated with IC3; see also Table S1 for the time lag values), which happen when the water level of the aquifer finally increases.

As regards IC4, its interpretation is less straightforward. We observe that the TWS computed in the Tevere basin is the one that differs the most from the others (Figure 6): it has the lowest correlation with V3 among the basins considered (Table S1), but the highest one, when considering V4 (Table S2). Our interpretation is that IC3 alone is not sufficient to well reproduce the displacements associated with TWS changes in all the basins considered, in particular in the Tevere which include a significant number of GNSS stations; so that IC4 is needed.

4. Postseismic relaxation

The post seismic relaxation is mapped in the first independent component with two post seismic decays, the first following the Amatrice event and the second one following the Visso and Norcia events (Figure 3a and 7). Explaining the whole post-seismic sequence with a single IC indicates a limitation of the signal separations. In fact, we would expect from a physical point of view at least three regions independently activated by afterslip, surrounding the corresponding mainshocks distributions. We made an attempt to separate these expected relaxations performing an ICA on the time series filtered from the seasonal components retrieved in the first analysis (those discussed in Section. 3), but no further ICs related to post-seismic relaxation processes could be extracted (more details of this analysis can be found in the supporting material, Section S4). Therefore, in this work we consider IC1 as representative of the whole post-seismic deformation and we will discuss the limitations associated with this interpretation in Section 5.

The straightforward interpretation of a post-seismic relaxation process is represented by the occurrence of afterslip on faults. In this study we consider as primary faults those structures

already introduced in Section 1, namely the M. Vettore fault, its antithetic fault and the Laga Mountains fault (see also Figure 1). As mentioned in Section 1, the segmentation of this fault system is not unequivocally defined in the literature, therefore we explain the data following the basic principle to keep the faults' geometry as simple as possible, considering also the number of GNSS stations available. In order to take into account the four Mw > 5 events of January 2017, we extend the model down to the Campotosto fault segment. The post-seismic displacement recorded at the GPS sites in the Campotosto and Paganica area suggest a potential partial aseismic reactivation of the Paganica fault (see supplementary material S5 for more details).

We adopt the dip angles of the main co-seismic studies (Cheloni et al., 2017, 2019; Walters et al., 2018). The northern master fault here considered, resembles the M. Vettore fault from Cheloni et al. (2019) but it is furtherly extended along the strike direction as suggested by the presence of seismicity, and from now on we will refer to it simply as *M. Vettore fault*. For similar reasons, we consider a fault antithetical to the M. Vettore fault which has the same dip and strike angle as in Cheloni et al. (2017, 2019) and Walters et al. (2018) but is extended northwards. The southern master fault here considered unites part of the Gorzano fault in the Cheloni et al. (2017)s' notation (the Laga fault in Walters et al., 2018s' notation) and the Campotosto fault from Gualandi et al. (2014) and will be simply referred to as *Campotosto fault*. The Paganica fault is included following the Gualandi et al. (2014)s' geometry. Recent studies (e.g. Vuan et al., 2017; Michele et al., 2020) agree that the down-dip extension of the faults activated during the seismic sequence is bounded at depth by a subhorizontal thick layer of seismicity (Section 1) at a depth of about 10 km, which is consistent with the thickness of the brittle crust estimated by Boncio et al. (2004) for this area. All the faults are discretized in grids of patches of about 2x2 km^2 (Figure 8).

For the slip inversion we follow the conceptual scheme proposed by Kositsky & Avouac (2010) and adapted to the ICA decomposition by Gualandi et al. (2016). In practice, we invert the spatial pattern relative to the post-seismic IC and then we recombine the retrieved spatial slip distribution with the corresponding weight Σ and temporal function V. The linear system we are dealing with is described by the relation

$$d = U_1 = Gm \quad (3)$$

where the data vector d is the spatial deformation associated with the IC1, G stands for the

Green's functions for the fault system, m = (m_{strike} , m_{dip}) is the afterslip spatial distribution along the strike and the dip directions. The inversion follows the least squares formulation of Tarantola (2005) for linear problems:

$$m=m_0+C_{m0}\,G^T\,(GC_{m0}\,G^T+C_d)^{-1}(d-Gm_0) \quad (4)$$

$$C_m=C_{m0}-C_{m0}\,G^T\,(GC_{m0}\,G^T+C_d)^{-1}\,GC_{m0} \quad (5)$$

where m0 and Cm0 represent respectively the a priori model (null as in Radiguet et al., 2011) and its covariance matrix, G are the Green's functions for a homogeneous elastic half-space, d is the data vector, and Cd the corresponding covariance matrix. We impose an additional positivity constraint to account for the dip-slip tectonic setting (i.e. $m_{dip}\leq 0$). We follow, for the a priori model covariance matrix, the formalism of Radiguet et al. (2011), which considers the spatial correlation of slip on patches to decay exponentially. Provided that A and B are two fault patches at a distance d_AB :

$$C^{AB}_{m0}=(\sigma_m\,\lambda_0\,/\lambda)^2\,e^{-d\_AB/\lambda} \quad (6)$$

where λ is the characteristic decay length, λ_0 is a scaling length factor fixed to the root square of the average of the patches' area, σ_m is a standard deviation of the a priori model parameters. The inversion needs to be regularized determining the values (λ , σ_m). The regularization parameters (λ , σ_m) associated with each fault depend on the dimension of the fault itself, therefore a unique set of values cannot be selected for the whole fault system. They are fixed seeking the best compromise between a physically acceptable solution (i.e. compatible with the tectonic setting) and the misfit with the data, and they resulted in a λ=2*λ_0 and a priori standard deviation σ_m= 0.71 for the M. Vettore and its antithetic fault and σ_m=1 for the Campotosto and the Paganica faults. The preferred solution results in the afterslip distribution shown in Figure 8: it satisfactorily reproduces the data, with an almost perfect reconstruction of the displacement pattern in the epicentral area, whereas farther GPS sites show a weaker agreement (Figure 8).

This model shows the occurrence of slip on the deepest portion of the M. Vettore fault below the co-seismic ruptures of the Amatrice and Norcia earthquakes, with a maximum slip > 40 cm and a prevalent normal mechanism (Figure 8a), while below the Visso area transcurrent slip reaches up to ~25-30 cm. Contextually the antithetic fault, activated by the Mw 5.4 event that occurred one hour after the Amatrice main event (Chiaraluce, Di Stefano, et al., 2017), accommodates normal slip (~25 cm) in its deepest part, where the fault meets the M. Vettore main fault. The Campotosto fault accommodates some slip about 10 km south of the town of Amatrice with a maximum slip of ~25 cm and, with a similar intensity, about 10 km southwards. Our solution suggests the presence of aseismic slip on the northernmost edge of the Paganica fault, which was partially activated by the 2009 L'Aquila earthquake in a different area as shown in Figure 8d (Gualandi et al., 2014; Ragon et al., 2019).

As it can be observed from Figure 8, the afterslip mechanism is not sufficient to explain the ~2.3 years cumulative displacement recorded by the whole GPS network. Remarkably, the displacement produced at sites farther from the epicentral area during the post-seismic phase appears to have a signal to noise ratio > 1 (see error ellipse in Figure 4), however they are generally underestimated by the modeled afterslip distribution. In order to better highlight this fact, we compare the elastic response of the GPS stations to a homogeneous slip of 1 m on a 60 km long, 10 km deep rectangular fault plane, which represents an along-strike extension of the major structures described in Cheloni et al. (2017, 2019), with the L2 norm relative to the IC1 spatial response at the studied stations (a more detailed description can be found in Supplementary material S6). This procedure allows us to identify those sites (red triangles in Figure S10a) that cannot be modeled only through slip on the major structures involved in the seismic sequence ("far-field" sites): indeed we notice from Figure S10b that the elastic afterslip model systematically underestimates the IC1 displacement at far-field sites, suggesting that a purely elastic mechanism is not sufficient to justify the displacement records of the whole dataset. As Figure 8 shows, this fact remains true in spite of the strong concentration of afterslip on the deepest patches of the high angle faults.

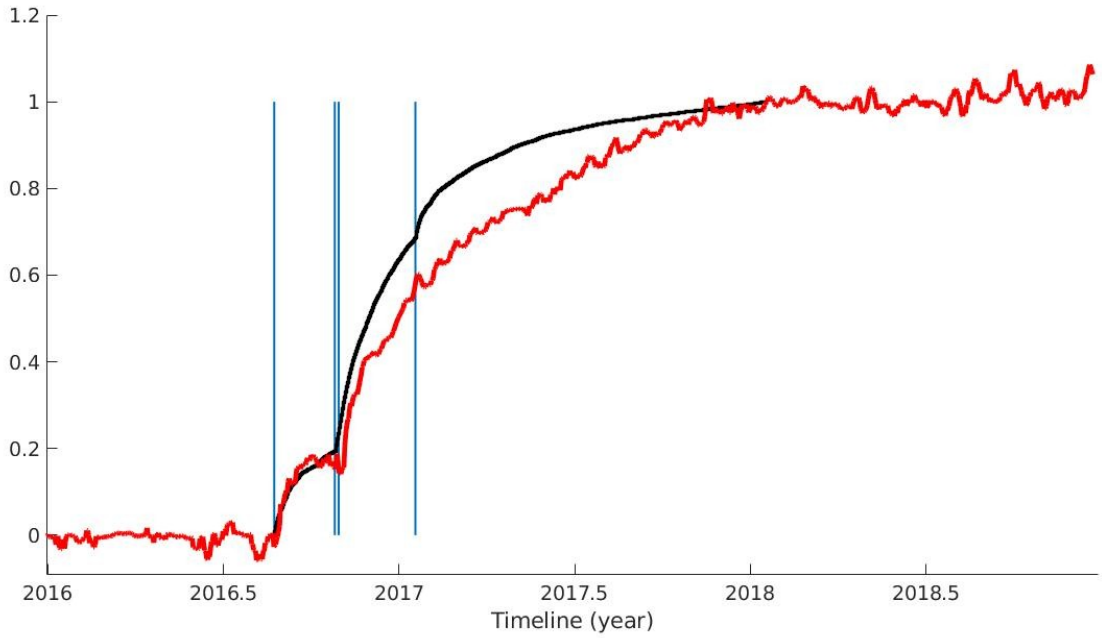

505

Figure 7. In Figure the normalized cumulative number of aftershocks from the catalogue described in Michele et al. (2020) (black line) and the normalized filtered post-seismic evolution (red line). Vertical lines mark the epochs respectively of the Amatrice, Visso, Norcia and the January 2017 Campotosto earthquakes.

25

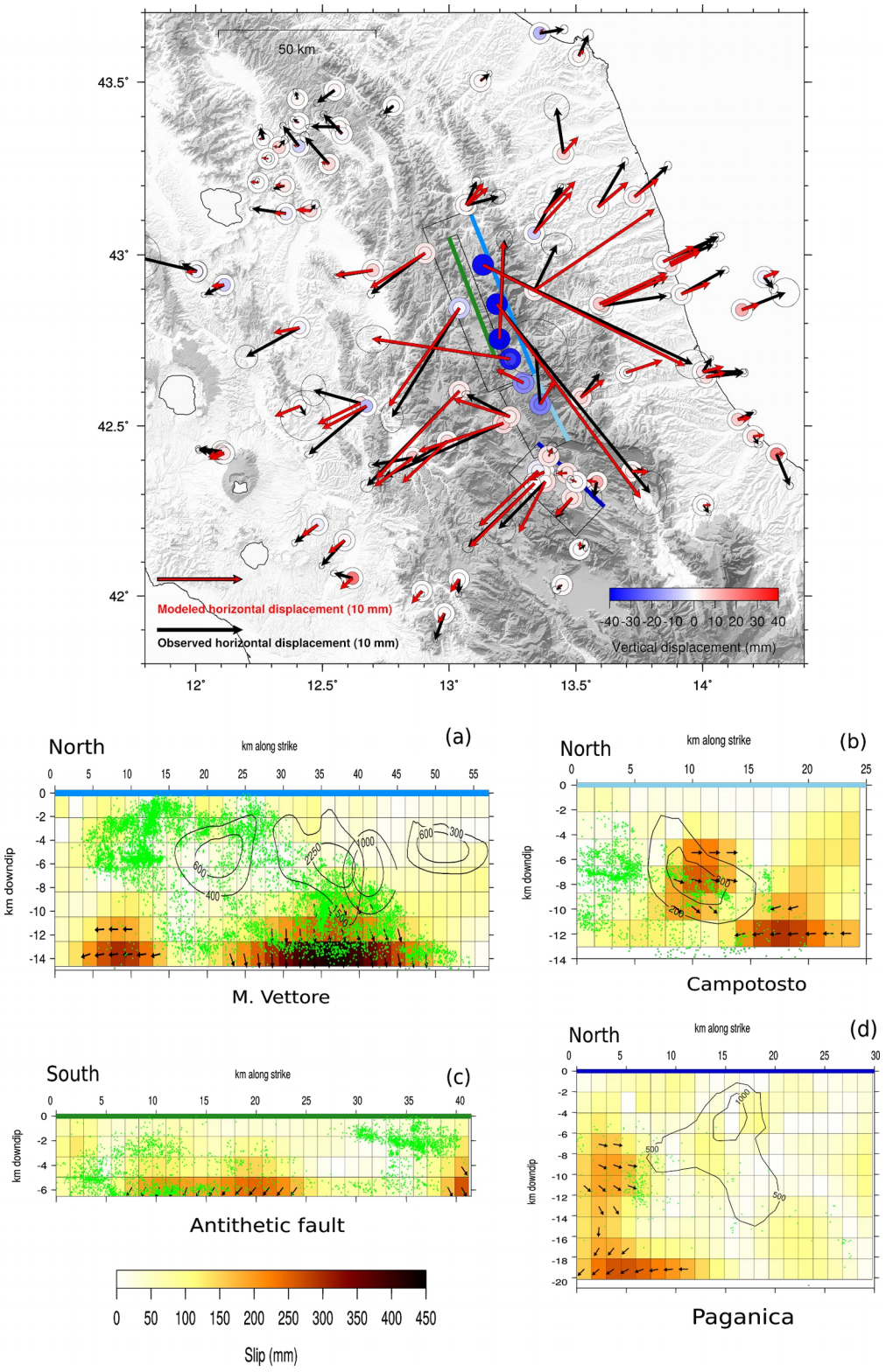

Figure 8. Map: black and red arrows represent respectively the observed and the modeled horizontal post-seismic cumulative displacement on the 24th of August 2016 - January 2019 time

interval, whereas inner and outer circles represent respectively the observed and the modeled vertical post-seismic cumulative displacement. Solid lines show the surface projection of the high faults described in Section 4. The faults' traces are coloured as in panels (a, b, c, d) which show the afterslip distribution on the M. Vettore, Campotosto, antithetic and Paganica faults, respectively, in a strike-dip reference system (slip in mm). Co-seismic contours on the M. Vettore fault are from Cheloni et al. (2017, 2019), on the Campotosto fault from Cheloni et al. (2019a), on the Paganica fault are from Gualandi et al. (2014)

4.1 The shear zone as a planar surface

As many authors show (e.g., Chiaraluce, Di Stefano, et al., 2017; Michele et al., 2020), the ~2-3 km-thick subhorizontal layer of seismicity (i.e. shear zone) played an important role during the seismic sequence. Vuan et al. (2017) suggest that aftershocks nucleating within such volume may be triggered by afterslip and Pousse-Beltran et al. (2020) infer a possible contribution of the shear zone to the displacement field. To further investigate its potential role during the post-seismic phase, we carry out the inversion of our dataset following the same procedure described in Section 4, including the shear zone as two planar surfaces. We model it according to the interpretations shown in figure 10b of Michele et al. (2020) and in figure 1 of Vuan et al. (2017). Such model of the shear zone consists of a ramp-flat fault divided in a low-angle east dipping plane and an almost flat detachment, respectively east and west of the Apennines chain, and the two surfaces are discretized into patches of about 3x3 km^2 (Figure 9e, f; Figure 10b)

When we include the shear zone in the inversion of the data, slip on the four high-angle faults (Figure 8) is not concentrated on the deeper patches only but it occurs on shallower patches as well, thus slightly involving areas already co-seismically activated. This is true in particular for the M. Vettore and its antithetic fault (Figure 9a and c), where afterslip is more distributed and its maximum intensity is reduced (max of slip ~20 cm). On the other hand, on the southern structures (i.e. the Campotosto and Paganica faults, Figure 9b and d) we observe a reduction in the amount of slip that they accommodate, but the inclusion of the shear zone does not substantially change the areas involved in the post-seismic phase (for a comparison between the

two inversion models see Figure S16 in the supplementary material).

Moreover the western, flat, part accommodates slip in an area that would correspond to the down-dip prosecution of the M. Vettore fault slipping area, reaching the maximum (~10 cm) on its deepest edge (Figure 9e). The eastern part of the shear zone (Figure 9f) shows a concentration of afterslip on the deepest patches as well but with greater intensities (~18-20 cm). For what concerns the data reconstruction (Figure 10a) we find a slightly better reproduction of the displacement for some near field sites, with respect to the model of Section 4 (Figure S17 of Supplementary material). As regard the far-field stations, on the Adriatic side we find an improvement in the fit (WRMSE improvement ~16.5%, see Tab. S3 of Supplementary material) whereas for the Thyrrenian side this model only marginally improves the fit at far-field stations (WRMSE improvement ~0.5%, Tab. S3 of Supplementary material). Since the fit to the data on the whole dataset results to be generally improved (WRMSE improvement ~6%, Tab. S3 of Supplementary material) and contextually we observe a reduction of afterslip at the base of the faults, the inversion that includes the shear zone (Figure 9) results to be our preferred solution.

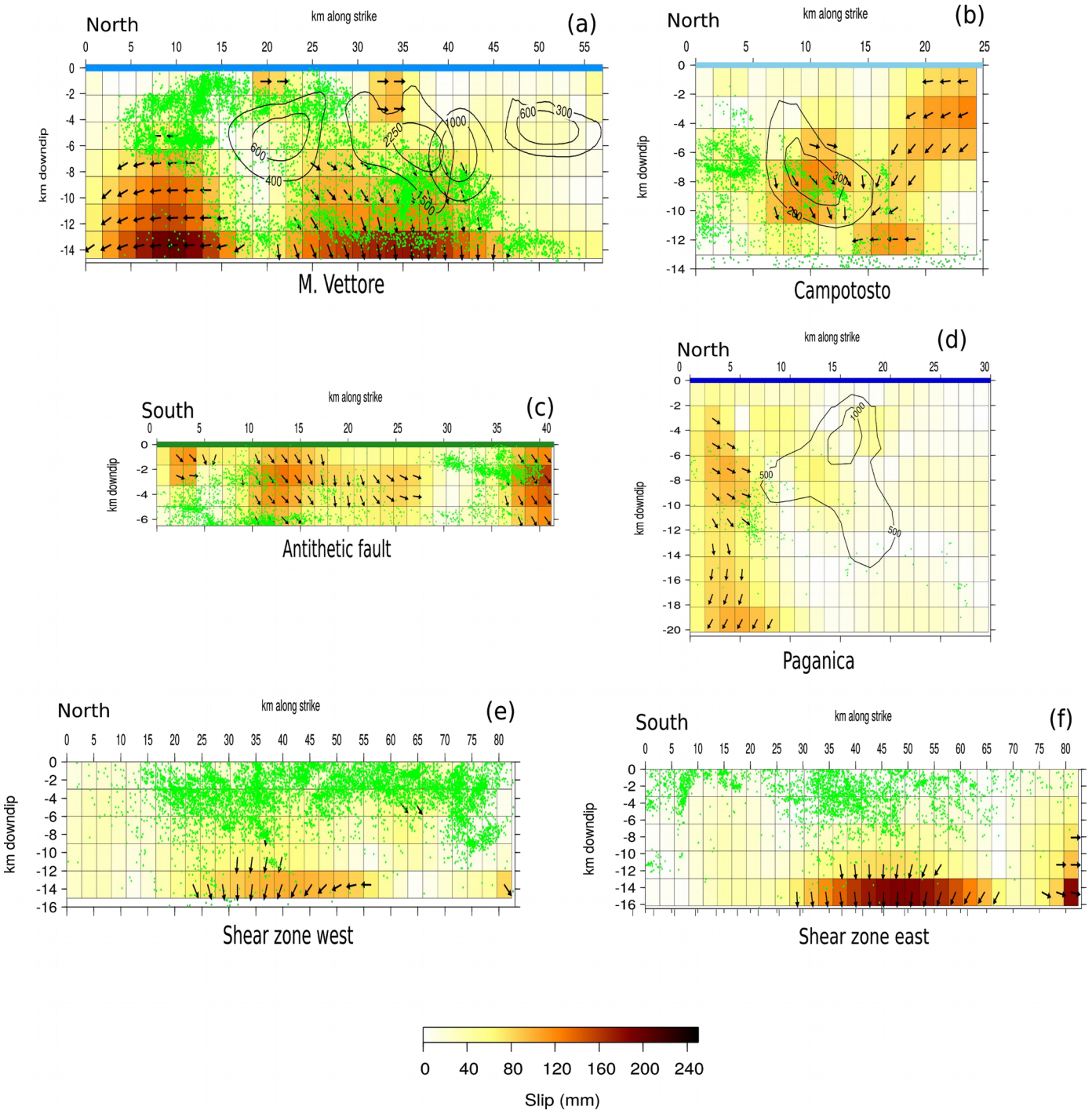

Figure 9. Panels (a, b, c, d) show the afterslip distribution respectively on the M. Vettore, Campotosto, antithetic and Paganica faults in a strike-dip reference system. Panels (e) and (f) show the afterslip distribution on the western and eastern segments of the shear zone (slip in mm).

Co-seismic contours on the M. Vettore fault are from Cheloni et al. (2017, 2019), on the Campotosto fault from Cheloni et al. (2019a), on the Paganica fault are from Gualandi et al. (2014).

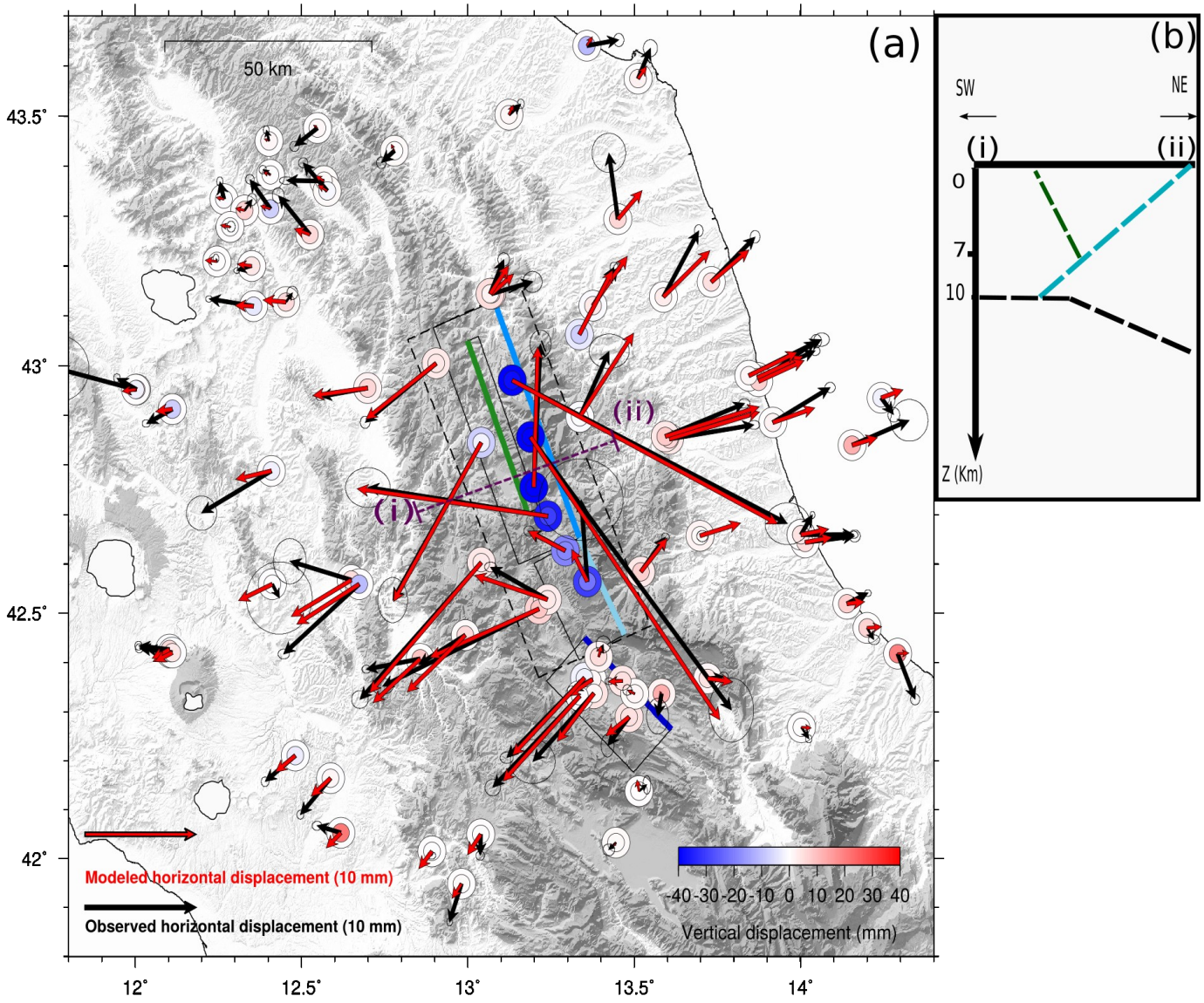

565 **Figure 10.** (a): black and red arrows represent respectively the observed and the modeled horizontal post-seismic cumulative displacement, whereas inner and outer circles represent respectively the observed and the modeled vertical post-seismic cumulative displacement. Solid lines show the surface projection of the high faults described in Section 4 and dashed lines the surface projection of the shear zone as described in Section 4.1. The faults' traces are coloured as

30

in panels (a, b, c, d) of Figure 9. (b): we show a cross-section of the fault system along the (i)-(ii) line.

4.2 Viscoelastic relaxation

From Figure 10a we notice a general underestimate of the displacement pattern recorded at far-field GPS sites with much of the afterslip localized in the deepest portions of the faults. As it is suggested by Riva et al. (2007) for the Colfiorito seismic sequence, afterslip at the base of the seismogenic layer might reflect a rheological discontinuity between the upper brittle crust and the underlying layers, herein referred to as the brittle-ductile transition. Furthermore, as many authors (e.g. Perfettini & Avouac, 2007) showed, a correlation in time between afterslip and the cumulative number of aftershocks exists. In our case, this remains true up to a few months after the 30th of October earthquake only (Figure 7), corroborating the hypothesis of other postseismic mechanisms acting after the Norcia mainshock besides afterslip.

Thus, following also previous authors (Pousse-Beltran et al., 2020), we investigate a possible contribution of the viscoelastic lower crust and upper mantle to the displacement field. We use the open-source software RELAX 1.0.7 (Barbot & Fialko, 2010). For simplicity, we consider here as an initial stress perturbation the one generated by the coseismic slip distribution of the major event of the sequence (i.e. the Norcia Mw 6.5 earthquake) as described in Cheloni et al. (2019). We model the viscoelastic medium through Maxwell rheologies even though we are aware of the potential importance of power-law rheologies in controlling viscoelastic relaxation (e.g. Freed & Burgmann 2004). Due to the length of our post-seismic time series (～2 years) and the relaxation rates in the order of a few millimetres per year characteristics of moderate earthquakes (Riva et al., 2007), it is possible that our data cannot properly point out the differences with other rheologies. The rheological profile we implement (Figure 11a) consists of a brittle upper crust (elastic parameters $\lambda=\mu=30$ GPa) which overlays the lower crust and the lithospheric mantle located below 33 km depth (Pousse-Beltran et al., 2020).

As already acknowledged by Freed et al. (2006), when we use stress driven models (such as ours)

to study surface deformations from viscoelastic relaxation, a central issue is to justify the far-field observations without overshooting the near-field data: too low viscosities and/or too thick viscoelastic layers can easily reproduce the far-field data but they greatly overestimate the near-field data (and vice versa). The tests we performed suggest viscosity values in the range of $10^{18} < \eta_{lc} < 10^{19}$ Pa s for the lower crust, and a thickness of about 18 km. Taking $\eta_{lc} < 10^{18}$ Pa s, we observe a non-monotonic temporal evolution of the displacement at some GPS sites (supplementary material S7) which differs from IC1. Moreover, due to the short relaxation time (in the order of 0.1 yr) we predict a cm-scale post seismic displacement, which is not justified by our data. Hence, we fix the viscosity of the lower crust $\eta_{lc} = 5x10^{18}$ Pa s, and the viscosity of the mantle $\eta_m = 10^{21}$ Pa s. Remarkably, the mantle is located too deep and its viscosity is too high for its effect to be observable on our dataset (Riva et al., 2007).

However, several seismological studies (e.g. Tesauro et al., 2008; Di Stefano et al., 2009; Molinari and Morelli, 2011; Molinari et al., 2015) highlight in this sector of the central Apennines a heterogeneity of the crust thicknesses showing a positive gradient for the depth of the lower crust starting from the western Tyrrhenian side up to the eastern Adriatic side, which is consistent with the eastward deepening of the brittle-ductile transition proposed by Carminati et al. (2001), Carannante et al. (2013), Vuan et al. (2017), and modeled by Albano et al. (2020). To simulate this feature, we consider a second model in which the upper crust has a depth of 11 km on the western side of the Apennines, below which it increases to 15 km of depth, affecting the entire eastern side (Figure 11b). The map in Figure 11 shows the horizontal displacement field deriving from the relaxation of the viscoelastic lower crust, for a variable (red arrows) and constant (blue arrows) brittle-ductile transition depth. The ~2 years long cumulative vertical displacement resulting from the models (~3 mm) is below the threshold of detection of GPS for all the sites away from the epicentral area and it is therefore not represented in Figure 11. In the Adriatic side the two models are equivalent as well as the displacements they produce in the far-field, which agree in direction with IC1. West of the M. Vettore fault the constant-thickness model provides smaller displacements both in near and far field, coherently with a thicker brittle crust. Accordingly, the model with uniform thicknesses (Figure 11a) allows us to find the best compromise between the near-field and the far-field data, namely to explain the missing displacement at far-field sites while not overestimating near-field observations which are already well modeled by afterslip (see Figure

10).

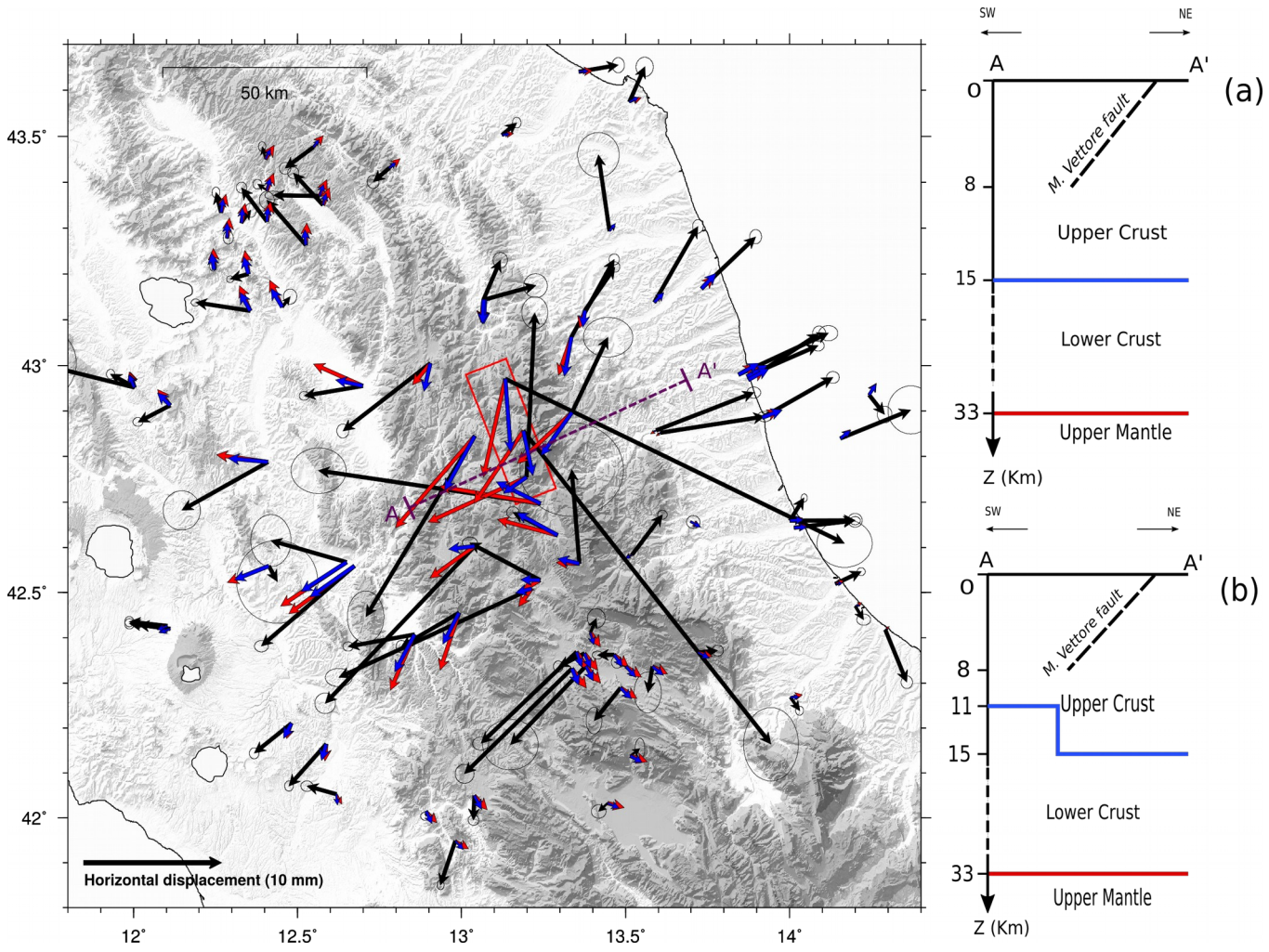

Figure 11. In map we compare the post-seismic IC (black arrows) and the viscoelastic relaxation field after 2.1 years from the 30th of October Norcia mainshock (blue arrows for the model with a constant brittle-ductile transition's depth, red arrows for the model with a variable transition depth). The red box marks the surface projection of the (Cheloni et al., 2019)s' masterfault. (a) and (b): cross sections along the AA' line respectively for the model with constant and variable brittle-ductile transition's depth.

5. Discussion

In this work we analyze the displacement time-series of GPS sites active during and after the 2016-2017 Central Italy seismic sequence adopting a blind-source-separation algorithm based on variational bayesian ICA (vbICA). The analysis on the 2012-2019 time-span allows us to highlight one post-seismic component (IC1, Figure 3) plus three hydrological, seasonal, components (IC 2, 3, 4; Figure 3). The presence of a spatially-uniform vertical displacement signal, associated with the superficial hydrological loading, is consistent with other results, being usually the largest source of non-tectonic seasonal deformation (Michel et al., 2018, Serpelloni et al., 2018). The other two hydrological components represent displacements caused by underground water content variations, which can cause mm-scale horizontal displacements as already observed by Silverii et al. (2016) and Devoti et al. (2018) in the Apennines, and by Devoti et al. (2015), Serpelloni et al. (2018) and Pintori et al. (2021) in the Southern Alps. An additional analysis performed on the pre-seismic time-span (Section 2.1) does not show components that can be clearly associated with transient tectonic deformations. In particular we do not find evidence of a preparatory phase prior to the Amatrice mainshock (supplementary material S2), similar to the one described in Vičič et al. (2020).

The separation of non-tectonic sources of deformation is an important task, especially when dealing with mm-scale post-seismic displacements. This proved to be very important, for example, for the stations located in the Paganica area: such GPS sites, in fact, appear to be highly influenced by the multi-annual hydrological component (IC3), which shows a prevalent NE-SW horizontal deformation signature, consistent with the direction of the tectonic deformation in this area (Figure 4). However, the vbICA well separates the tectonic and non-tectonic signals, and neglecting a post-seismic contribution to the displacement of these sites leads to a bad modelization of the time series for the time period after the Norcia mainshock (see Figure S7 in the supporting material). Excluding the Paganica fault in the inversion implies a strong concentration of slip (supplementary material S5 and Figure S9a) on the southern edge of the Campotosto fault (i.e. as close as possible to the GPS sites location), which seems unlikely, considering the difference in magnitude between the events nucleated on the Campotosto fault

and those nucleated on the M. Vettore fault. Furthermore, slip on the Campotosto fault alone underestimates the displacement measured at the GPS sites in the Paganica area (Figure S9b). The Paganica fault, responsible for the 2009 L'Aquila earthquake, was not activated by the mainshocks of the 2016-2017 seismic sequence, but GPS displacements in the area suggest that this fault accommodated a few cm of slip (Figure 9d) between the end of 2016 and 2019. Calculating the stress perturbation, in terms of Coulomb Failure Function variation (DCFF), due to the main events of the sequence, as modeled by Cheloni et al. (2017, 2019, 2019a) on the six fault planes considered for the afterslip model (Figure S18 in the Supplementary material), we obtain positive values for the Paganica fault (DCFF ∼ 0.02-0.05 MPa) favoring slip on this structure. This finding highlights how faults interaction needs to be taken into account if we want to attempt a deterministic modelization of the seismic cycle.

As mentioned in Section 4, the temporal evolution of post-seismic deformation over the studied time-span is described by a single IC. Following Michel et al. (2018), we perform an iterative application of the ICA algorithm (see Supplementary material S4) that should enhance the accuracy of the extraction of post-seismic ICs in tectonically complex regions but, in our case, it does not lead to the separation of additional post-seismic components. The fact that the post-seismic relaxation is described solely by IC1 brings along some limitations: (i) in terms of afterslip, since the 2016-2017 seismic sequence was characterized by several mainshocks, describing their post-seismic phase only through the IC1 means that we cannot get any insight on the possible spatial migration or different activation times of the various faults involved in the seismic sequence. Our analysis is limited to a stationary spatial response of the slip, not allowing us to determine when the different parts of the faults actually began to slip. (ii) Three mechanisms primarily drive the post-seismic relaxation of stress: afterslip, poroelastic rebound, and viscoelastic flow. In this study we considered at least two of them (afterslip and viscoelastic flow) to be active, but we are not able to separate them one from the other as instead achieved with a similar approach, for example, in the post-seismic deformation study of the Mw 7.2 El Mayor-Cucapah earthquake (Gualandi et al., 2020). The simultaneous action of afterslip and viscoelasticity is also supported by the different decay describing the cumulative number of aftershocks and the temporal evolution of the post-seismic deformation signal (Figure 7). The reason why the ICA does not separate such mechanisms can be due to the short time span here

35

considered, and longer time-series will help to address this problem in the future. As a consequence we cannot exactly establish the relative contribution of the various deformation mechanisms to the total measured displacement field.

5.1 Afterslip Remarks

The afterslip distribution obtained including the four high angle faults only (Figure 8) results in a high concentration of afterslip at the base of the structures which, however, is not sufficient to explain the displacements observed at sites far from the epicentral area (red triangles in Figure S10a of the supplementary material) as we show in Section 4. The fact that the displacement measured at such far-field sites results to be statistically meaningful (as discussed in Section 2.1) drives our choice to add complexities to the initial model (Figure 8). First we attempt to investigate a contribution of the shear zone highlighted by seismicity, as suggested by Vuan et al. (2017) and Pousse-Beltran et al. (2020). The inclusion of the shear zone in the inversion leads to a better fit of the far-field GPS stations, as well as to a different slip distribution. In particular, we find a reduction of the afterslip at the bottom edges of the high angle faults (Section S8 of supplementary material) that is likely compensated by the slip accommodated by the bottom edge of the shear zone itself (Figure 9e and 9f). We can compare our preferred solution (Figure 9) with results obtained by Pousse-Beltran et al. (2020). The latter, using InSAR measurements integrated by near-field GPS stations, modeled slip on the M. Vettore and its antithetic fault with a geometry similar to that of Cheloni et al. (2019). Our faults, and in particular the M. Vettore fault and its antithetic fault, share the same orientation (dip and strike), but following the seismicity pattern their length along strike is extended. Therefore we can compare the Pousse-Beltran et al. (2020)s' slip distribution (figure S21 in Pousse-Beltran et al., 2020s' supplementary material) and the afterslip we retrieve on the four high angle faults (i.e. the M. Vettore, the Campotosto, the Paganica and the antithetic fault). Pousse-Beltran et al. (2020) found two main slipping areas, which are mapped on the M. Vettore fault (Figure 9a) between 40 - 45 km along strike, 0 - 2 km downdip (shallow slip in the area of Arquata del Tronto, see Section 1); and between 38 - 40 km along strike, 4 - 8 km downdip (slip in the Castelluccio area, see Section 1). On the contrary, our preferred solution does not suggest significant shallow slip below Arquata. Some shallow slip is observed on the M. Vettore fault between 30 - 35 km along strike (Figure 9a), about 10 km NE of the shallow slipping area of Pousse-Beltran et al. (2020). The second slipping zone (i.e. the one

in the Castelluccio area) is less certain, as claimed by the authors themselves, and involves areas that ruptured co-seismically during the Amatrice and the Norcia mainshocks. Our preferred solution does not show such overlapping, as afterslip on the M. Vettore fault is mainly accommodated outside the co-seismic areas (Figure 9a). Moreover the maximum amount of slip that Pousse-Beltran et al. (2020) retrieve (∼16 cm) is less than what we have observed in our study (~ 24 cm): this can partly be explained by the shorter time span considered by Pousse-Beltran et al. (2020) (i.e. from November 1 2016 to February 11 2017) and by the fact that the GPS dataset we employ covers a much wider area than the interferograms used in Pousse-Beltran et al. (2020). Therefore our model demands greater intensities of slip to explain the far-field stations. Figure 9b shows that the northern slipping area on the Campotosto fault overlaps with the co-seismic slip distribution of Cheloni et al. (2019a). However their solution is derived from InSAR data that encompassed the displacement of the first month after the January 2017 mainshocks. We estimate that in that time period (i.e. up to February 11) about 8% of the moment released is due to post-seismic relaxation. For what concerns the shear zone, it accommodates a few cm of slip on the eastern, slightly E-dipping, side (Figure 9f). Such concentration of slip far from the co-seismic slip distribution is likely driven in the inversion by displacements measured at sites towards the Adriatic coast. The stress perturbation due to the mainshocks of the 2016-2017 sequence on those deep patches results to be slightly>0 (DCFF∼ 0.05-0.1 MPa, Figure S18 supplementary material), therefore in principle slip in that area is not forbidden.

The equivalent seismic moment associated with the postseismic phase (up to January 2018) is $M_0^{geodetic}$ = 6.25x10^{18} Nm (for a rigidity modulus = 30 GPa) that corresponds to a Mw 6.5. This value may be compared with the seismic moment released by aftershocks. To this aim, we consider the seismic catalogue described by Michele et al. (2020) and convert the reported ML into Mw using the relation Mw-ML proposed by Munafò et al. (2016) for small events. The moment released by aftershocks up to January 2018 is $M_0^{aftershocks}$ = 4.60x10^{17} Nm, meaning that the post-seismic deformation was dominated by aseismic motion. As regard the spatial relationships among afterslip, aftershocks and coseismic slips, aftershocks on the Campotosto and antithetic faults overlap only partially with the patches undergoing postseismic slip (Fig 9 b and c). On the M. Vettore fault (Figure 9a) a first cluster of aftershocks is located on the bottom

edge of the Amatrice and Norcia co-seismic ruptures where a large amount of afterslip is accommodated; whereas a second cluster is located in the shallower portion of the fault around the Visso slipping area. The majority of the aftershocks of this second cluster occurs outside the patches undergoing afterslip, which might be due to a lack of GPS coverage in that area.

5.2 Viscoelastic Remarks

The maximum value of afterslip of our preferred solution is located at the base of the high-angle faults, and, following Riva et al. (2007), who studied the 1997 Umbria-Marche seismic sequence, this might be symptomatic of a rheological discontinuity decoupling the seismogenic upper crust from a viscoelastic lower crust. According to Boncio et al. (2004) beneath this sector of the Apennines the active faults in the seismogenic layer detach into a layer dominated by aseismic plastic flow passing through a broad transition zone. Such detachment is illuminated by a high seismicity rate discussed by Vuan et al. (2017) and, following Chiaraluce, Barchi, et al. (2017), interpreted as the top of the brittle-ductile transition. Flat detachments can mark the presence of the brittle-ductile transition within the crust (Carcione et al., 2014; Fayon et al., 2000; Jolivet et al., 2010; Platt et al., 2015; Rabillard et al., 2018). According to Nespoli et al. (2019) the fault dip angle is expected to drastically decrease just below the brittle-ductile transition. Below the detachments, which can be interpreted as ductile shear zones (Rabillard et al., 2018), an elasto-plastic rheology can be assumed and rocks behave like viscoelastic materials (Carcione et al., 2014; Fayon et al., 2000). The brittle-ductile transition in this sector of the Apennines deepens going from west to east (e.g., Carminati et al., 2001; Carannante et al., 2013): having fixed the rheological profile in this way, taking $\eta_{lc} = 5x10^{18}$ Pa s and about 18-22 km of thickness for the lower crust, we obtain a displacement field consistent with the geodetic observations. Such setting is in line with model LC18 of Riva et al. (2007). We can further simplify such model and take a constant brittle-ductile transition at 15 km depth (Section 4.2) matching the near- and far-field post-seismic displacements slightly better. As shown in Riva et al. (2007), lowering η_{lc} below 10^{18} Pa s leads to a worsening of the fit, in agreement with our findings (Supplementary S7). On the other hand, Riva et al. (2007) suggest a slightly thinner viscoelastic layer (about 12 km) which is likely compensated by their lower viscosity ($\eta = 10^{18}$ Pa s). As a matter of fact, a trade-off between the thickness of the viscoelastic layer and its viscosity exists. Pousse-Beltran

et al. (2020) modeled a viscoelastic relaxation following the Norcia earthquake as well, but they found an opposite vertical polarity (i.e. uplift) and therefore discharged viscoelasticity as a possible driving mechanism for post-seismic deformation. We impute this fact to the rheological profiles they implemented, that accounts for a $\partial\eta/\partial z<0$ and, according to Hetland & Zhang (2014), if a high viscosity layer is placed between the elastic layer and the underlying substrates, the vertical post-seismic and coseismic deformations exhibit an opposite polarity. Both our viscoelastic models consider the thick layer of seismicity that bounds the high-angle normal faults to be elastic on the time scale of the analysis. Hetland & Zhang (2014) showed that if the co-seismic rupture does not entirely break the seismogenic layer then the unruptured portion behaves like a viscoelastic material with very high viscosity. Our tests suggest that the lower bound for the viscosity of the volume of seismicity described by Vuan et al. (2017) is 10^{20} Pa s, and lower viscosities would produce unobserved effects at near-field GPS stations.

In light of the considerations discussed in this Section, we propose that viscoelastic relaxation of the lower crust may be a mechanism contributing to the measured post-seismic displacements, but a deeper understanding is limited by several factors. For instance the length of the post-seismic time series analyzed is short (about 2 years) with respect to the typical time scales of viscoelastic processes, bearing also in mind that moderate events (such as the Mw 6.5 Norcia earthquake) lead to deformation rates in the order of few mm/yr (Riva et al., 2007). Furthermore, a major problem in understanding the post-seismic response of the lithosphere to an earthquake is the uniqueness of the explanation. Since the vbICA separates only one post-seismic component, a clear distinction between afterslip and viscoelastic relaxation contribution proved to be a challenging task. We suggest that both afterslip and viscoelastic relaxation acted during the post-seismic phase of the sequence and one should be careful in preferring one mechanism to the other because of the good agreement with the observations (Freed et al., 2006). The good reproduction of GPS displacements by afterslip is not surprising, as the inversion is not constrained by physical processes such as coseismic stress changes, whereas the misfit produced by the viscoelastic model can be explained by the simplifications made in our forward models to the real earth's case.

6. Conclusions

Exploiting GPS ground displacement time-series we study the post-seismic phase of the 2016-2017 Central Italy seismic sequence. We separate the post-seismic tectonic deformation signal from other hydrological deformation signals, the first being mapped in one single component despite the occurrence of at least three mainshocks. We find evidence of displacement related to post-seismic relaxation as far as ~90 km from the epicentral area, up to offshore stations in the Adriatic Sea. We exploit the high accuracies and temporal resolution offered by continuous GPS measurements in order to investigate the different mechanisms that caused post-seismic ground deformation. Afterslip is by far the most important process, explaining the majority of the measured displacements cumulated in 28 months after the Amatrice mainshock. We find that taking into account only the faults that hosted the mainshocks of the sequence leads to a bad modelization of the displacements observed at GPS sites in the Paganica area and at far-field sites, which drives our choice to invert for slip also on the Paganica fault and on the shear zone, respectively. The fact that the Paganica fault (unruptured in the co-seismic phase of the sequence) accommodated cm-scale slip in the post-seismic phase, highlights how interaction among faults has to be taken into account while attempting a deterministic modelization of the earthquake cycle.

Given the afterslip concentration at the base of the seismogenic faults, the different temporal evolution of geodetic deformation and cumulative number of aftershocks and the discrepancies between measured and afterslip-modeled displacements, a viscoelastic contribution cannot be ruled out. In particular, we deem the relaxation of the lower crust to be a contributing mechanism in the 2 years following the Amatrice-Visso-Norcia seismic sequence. Bearing in mind the limits of the data and of our interpretation, we propose an afterslip model that is consistent with the co-seismic ruptures on the structures activated during the 2016-2017 seismic sequence. Furthermore, we provide some preliminary values of the viscosity and thickness of the lower crust, leaving further investigations to future studies, which might consider an afterslip + viscoelastic joint inversion of possibly longer time series.

Data availability statement

We use publicly available raw GNSS data. Raw GPS displacement time series are available on

40

https://doi.org/10.5281/zenodo.4633475; the GPS displacement time series used in input to vbICA are available on https://doi.org/10.5281/zenodo.4633412. The seismic catalogue is taken from Michele et al. (2020) and available at https://doi.org/10.5281/zenodo.3712731. The precipitation, temperature, and river flow data used to implement the hydrological model are available at https://annali.regione.umbria.it/, http://www.sir.toscana.it/consistenza-rete, https://console.regione.marche.it/ (http://app.protezionecivile.marche.it/sol/indexjs.sol?lang=it), for the Umbria, Toscana and Marche region, respectively. Data for the Abruzzo region are available under request to the REGIONE ABRUZZO "Dipartimento delle Opere Pubbliche, Governo del Territorio e Politiche Ambientali Servizio Programmazione Attività di Protezione Civile Ufficio Idrografico e Mareografico" (idrografico@regione.abruzzo.it). Extraterrestrial irradiance data are available at http://www.soda-pro.com/web-services/radiation/extraterrestrial-irradiance-and-toa. Drainage direction maps used to define river basins are available at www.hydrosheds.org/page/availability. Global datasets used for the hydrological load model are taken from https://grace.jpl.nasa.gov/data/get-data/jpl_global_mascons/ (GRACE), https://disc.gsfc.nasa.gov/datasets/GLDAS_NOAH025_3H_2.1/summary (GLDAS); http://loading.u-strasbg.fr (ERA-interim model); mean monthly temperature: GHCN Gridded data provided by the NOAA/OAR/ESRL PSL, Boulder, Colorado, USA, from their Web site at https://psl.noaa.gov/. A version of the vbICA software modified to take into account missing data is available at the Zenodo repository doi 10.5281/zenodo.4322548; the MATLAB code used to compute the TWS can be found at http://dx.doi.org/10.17632/m5p5xmrr7k.1. The software Relax used to model the viscoelastic relaxation is available at https://geodynamics.org/cig/software/relax/.

References

Albano, M., Barba, S., Bignami, C., Carminati, E., Doglioni, C., Moro, M., Saroli, M., Samsonov, S., Stramondo, S., (2020). Numerical analysis of interseismic, coseismic and post-seismic phases for normal and reverse faulting earthquakes in Italy, *Geophysical Journal International*, Volume 225, Issue 1, April 2021, Pages 627–645, https://doi.org/10.1093/gji/ggaa608

Amato, A., Azzara, R., Chiarabba, C., Cimini, G. B., Cocco, M., Di Bona, M., et al. (1998). The

1997 Umbria-Marche, Italy, Earthquake Sequence: A first look at the main shocks and aftershocks. *Geophysical Research Letters*, *25*(15), 2861–2864. https://doi.org/10.1029/98GL51842

Amos, C. B., Audet, P., Hammond, W. C., Bürgmann, R., Johanson, I. A., & Blewitt, G. (2014). Uplift and seismicity driven by groundwater depletion in central California. *Nature*, *509*(7501), 483–486. https://doi.org/10.1038/nature13275

Argus, D. F., Fu, Y., & Landerer, F. W. (2014). Seasonal variation in total water storage in California inferred from GPS observations of vertical land motion. *Geophysical Research Letters*, *41*(6), 1971–1980. https://doi.org/10.1002/2014GL059570

Barani, S., Mascandola, C., Serpelloni, E., Ferretti, G., Massa, M., & Spallarossa, D. (2017). Time–space evolution of seismic strain release in the area shocked by the august 24–october 30 central italy seismic sequence. *Pure and Applied Geophysics*, *174*(5), 1875–1887. https://doi.org/10.1007/s00024-017-1547-5

Barbot, S., & Fialko, Y. (2010). A unified continuum representation of post-seismic relaxation mechanisms: semi-analytic models of afterslip, poroelastic rebound and viscoelastic flow. *Geophysical Journal International*, *182*(3), 1124–1140. https://doi.org/10.1111/j.1365-246X.2010.04678.x

Boncio, Paolo & Lavecchia, Giusy. (2000). A geological model for the Colfiorito earthquakes (September-October 1997, central Italy). Journal of Seismology. 4. 345-356. 10.1023/A:1026509717771.

Boncio, P., Lavecchia, G., & Pace, B. (2004). Defining a model of 3D seismogenic sources for Seismic Hazard Assessment applications: The case of central Apennines (Italy). *Journal of Seismology*, *8*(3), 407–425. https://doi.org/10.1023/B:JOSE.0000038449.78801.05

Borsa, A. A., Agnew, D. C., & Cayan, D. R. (2014). Remote Hydrology. Ongoing drought-induced uplift in the western United States. *Science*, *345*(6204), 1587–1590. https://doi.org/10.1126/science.1260279

Carannante, S., Monachesi, G., Cattaneo, M., Amato, A., and Chiarabba, C. (2013), Deep structure and tectonics of the northern-central Apennines as seen by regional-scale tomography and 3-D located earthquakes, *J. Geophys. Res. Solid Earth*, 118, 5391– 5403, doi:10.1002/jgrb.50371.

Carcione, J. M., Poletto, F., Farina, B., & Craglietto, A. (2014). Simulation of seismic waves at the

earth's crust (brittle–ductile transition) based on the Burgers model. *Solid Earth*, *5*(2), 1001–1010. https://doi.org/10.5194/se-5-1001-2014

Carminati, E., Toniolo Augier, F. & Barba, S. (2001) Dynamic modelling of stress accumulation in Central Italy: role of structural heterogeneities and rheology. Geophys. J. Int., 144, 373390. doi:10.1046/j.1365-246x.2001.00323.x

Chanard, K., Fleitout, L., Calais, E., Rebischung, P., & Avouac, J.-P. (2018). Toward a Global Horizontal and Vertical Elastic Load Deformation Model Derived from GRACE and GNSS Station Position Time Series. *Journal of Geophysical Research: Solid Earth*, *123*(4), 3225–3237. https://doi.org/10.1002/2017JB015245

Chan, K., Lee, T.-W., & Sejnowski, T. J. (2003). Variational Bayesian Learning of ICA with Missing Data. *Neural Computation*, *15*(8), 1991–2011. https://doi.org/10.1162/08997660360675116

Cheloni, Daniele, D'Agostino, N., Scognamiglio, L., Tinti, E., Bignami, C., Avallone, A., et al. (2019a). Heterogeneous Behavior of the Campotosto Normal Fault (Central Italy) Imaged by InSAR GPS and Strong-Motion Data: Insights from the 18 January 2017 Events. *Remote Sensing*, *11*(12), 1482. https://doi.org/10.3390/rs11121482

Cheloni, D., De Novellis, V., Albano, M., Antonioli, A., Anzidei, M., Atzori, S., et al. (2017). Geodetic model of the 2016 Central Italy earthquake sequence inferred from InSAR and GPS data. *Geophysical Research Letters*, *44*(13), 6778–6787. https://doi.org/10.1002/2017GL073580

Cheloni, D., Falcucci, E., & Gori, S. (2019). Half-graben rupture geometry of the 30 october 2016 m_w 6.6 mt. vettore-mt. bove earthquake, central italy. *Journal of Geophysical Research: Solid Earth*, *124*(4), 4091–4118. https://doi.org/10.1029/2018JB015851

Cheloni, D., Serpelloni, E., Devoti, R., D'Agostino, N., Pietrantonio, G., Riguzzi F., Anzidei, M., Avallone, A., Cavaliere, A., Cecere, G., D'Ambrosio, C., Esposito, A., Falco, L., Galvani, A., Selvaggi, G., Sepe, V., Calcaterra, S., Giuliani, R., Mattone, M., Gambino, P., Abruzzese, L., Cardinale, V., Castagnozzi, A., De Luca, G., Massucci, A., Memmolo, A., Migliari, F., Minichiello, F., Zarrilli, L. (2016). GPS observations of coseismic deformation following the 2016, August 24, Mw 6 Amatrice earthquake (central Italy): data, analysis and preliminary fault model.

Chiaraluce, L., Amato, A., Cocco, M., Chiarabba, C., Selvaggi, G., Di Bona, M., Piccinini, D., Deschamps, A., Margheriti, L., Courboulex, F., Ripepe, M.; Complex Normal Faulting in the

Apennines Thrust-and-Fold Belt: The 1997 Seismic Sequence in Central Italy. *Bulletin of the Seismological Society of America* 2004;; 94 (1): 99–116. doi: https://doi.org/10.1785/0120020052

Chiaraluce, L. (2012). Unravelling the complexity of Apenninic extensional fault systems: A review of the 2009 L'Aquila earthquake (Central Apennines, Italy). *Journal of Structural Geology*, *42*, 2–18. https://doi.org/10.1016/j.jsg.2012.06.007

Chiaraluce, L., Ellsworth, W. L., Chiarabba, C., & Cocco, M. (2003). Imaging the complexity of an active normal fault system: The 1997 Colfiorito (central Italy) case study. *Journal of Geophysical Research*, *108*(B6). https://doi.org/10.1029/2002JB002166

Chiaraluce, L., Di Stefano, R., Tinti, E., Scognamiglio, L., Michele, M., Casarotti, E., et al. (2017). The 2016 central italy seismic sequence: A first look at the mainshocks, aftershocks, and source models. *Seismological Research Letters*, *88*(3), 757–771. https://doi.org/10.1785/0220160221

Chiaraluce, L., Barchi, M. R., Carannante, S., Collettini, C., Mirabella, F., Pauselli, C., & Valoroso, L. (2017). The role of rheology, crustal structures and lithology in the seismicity distribution of the northern Apennines. *Tectonophysics*, *694*, 280–291. https://doi.org/10.1016/j.tecto.2016.11.011

Choudrey, R. (2002). Bayesian Independent Component Analysis.

Civico, R., Pucci, S., Villani, F., Pizzimenti, L., De Martini, P. M., Nappi, R., & the Open EMERGEO Working Group. (2018). Surface ruptures following the 30 October 2016M_w 6.5 Norcia earthquake, central Italy. *Journal of Maps*, *14*(2), 151–160. https://doi.org/10.1080/17445647.2018.1441756

D'Agostino, N. (2014). Complete seismic release of tectonic strain and earthquake recurrence in the Apennines (Italy). *Geophysical Research Letters*, *41*(4), 1155–1162. https://doi.org/10.1002/2014GL059230

Davis, J. L., Wernicke, B. P., & Tamisiea, M. E. (2012). On seasonal signals in geodetic time series. *Journal of Geophysical Research*, *117*(B1). https://doi.org/10.1029/2011JB008690

Dee, D. P., Uppala, S. M., Simmons, A. J., Berrisford, P., Poli, P., Kobayashi, S., et al. (2011). The ERA-Interim reanalysis: configuration and performance of the data assimilation system. *Quarterly Journal of the Royal Meteorological Society*, *137*(656), 553–597. https://doi.org/10.1002/qj.828

Devoti, R., D'Agostino, N., Serpelloni, E., Pietrantonio, G., Riguzzi, F., Avallone, A., et al. (2017). A combined velocity field of the mediterranean region. *Annals of Geophysics*, *60*(2). https://doi.org/10.4401/ag-7059

Devoti, R., Riguzzi, F., Cinti, F.R., Ventura, G. (2018); Long-term strain oscillations related to the hydrological interaction between aquifers in intra-mountain basins: A case study from Apennines chain (Italy), Earth and Planetary Science Letters, 501, 1-12, https://doi.org/10.1016/j.epsl.2018.08.014.

Devoti, R., Zuliani, D., Braitenberg, C., Fabris, P., Grillo, B. (2015); Hydrologically induced slope deformations detected by GPS and clinometric surveys in the Cansiglio Plateau, southern Alps, Earth and Planetary Science Letters, 419, 134-142, https://doi.org/10.1016/j.epsl.2015.03.023.

Di Stefano, R., E. Kissling, C. Chiarabba, A. Amato, and D. Giardini (2009), Shallow subduction beneath Italy: Three-dimensional images of the Adriatic-European-Tyrrhenian lithosphere system based on high-quality P wave arrival times, J. Geophys. Res., 114, B05305, doi:10.1029/2008JB005641

Dong, D., Fang, P., Bock, Y., Cheng, M. K., & Miyazaki, S. (2002). Anatomy of apparent seasonal variations from GPS-derived site position time series. *Journal of Geophysical Research*, *107*(B4), ETG 9-1-ETG 9-16. https://doi.org/10.1029/2001JB000573

EMERGEO W.G. : Pucci, S., De Martini, P.M., Civico, R., Nappi, R., Ricci, T., Villani, F., Brunori, C.A., Caciagli, M., Sapia, V., Cinti, F.R. , Moro, M., Di Naccio, D., Gori, S., Falcucci, E., Vallone, R., Mazzarini, F., Tarquini, S., Del Carlo, P., Kastelic, V., Carafa, M., De Ritis, R., Gaudiosi, G., Nave, R., Alessio, G., Burrato, P., Smedile, A., Alfonsi, L., Vannoli, P., Pignone, M., Pinzi, S., Fracassi, U., Pizzimenti, L., Mariucci, M.T., Pagliuca, Sciarra, N., A., Carluccio, R., Nicolosi, I., Chiappini, M., D'Ajello Caracciolo, F., Pezzo, G.,Patera, A. , Azzaro, R., Pantosti,D., Montone, P., Saroli, M., Lo Sardo, L., Lancia, M.. Coseismic effects of the 2016 Amatrice seismic sequence: first geological results. Annals of Geophysics (2016). https://doi.org/10.4401/ag-7195

Fan, Y., & van den Dool, H. (2008). A global monthly land surface air temperature analysis for 1948–present. *Journal of Geophysical Research*, *113*(D1).

45

https://doi.org/10.1029/2007JD008470

Falcucci, E., Gori, S., Galadini, F., Fubelli, G., Moro, M., Saroli, M., (2016) Active faults in the epicentral and mesoseismal Ml 6.0 24, 2016 Amatrice earthquake region, central Italy. Methodological and seismotectonic issues, Annals of Geophysics. https://doi.org/10.4401/ag-7266

Fayon, A. K., Peacock, S. M., Stump, E., & Reynolds, S. J. (2000). Fission track analysis of the footwall of the Catalina detachment fault, Arizona: Tectonic denudation, magmatism, and erosion. *Journal of Geophysical Research*, *105*(B5), 11047–11062. https://doi.org/10.1029/1999JB900421

Ferrarini, F., Lavecchia, G., de Nardis, R., & Brozzetti, F. (2015). Fault Geometry and Active Stress from Earthquakes and Field Geology Data Analysis: The Colfiorito 1997 and L'Aquila 2009 Cases (Central Italy). *Pure and Applied Geophysics*, *172*(5), 1079–1103. https://doi.org/10.1007/s00024-014-0931-7

Freed, A.M. & Burgmann, R., (2004). Evidence of power-low flow in the Mojave desert mantle, Nature, 430, 548–551.

Freed, A. M., Bürgmann, R., Calais, E., Freymueller, J., & Hreinsdóttir, S. (2006). Implications of deformation following the 2002 Denali, Alaska, earthquake for postseismic relaxation processes and lithospheric rheology. *Journal of Geophysical Research*, *111*(B1). https://doi.org/10.1029/2005JB003894

Galadini, F., Falcucci, E., Gori, S., Zimmaro, P., Cheloni, D., & Stewart, J. P. (2018). Active faulting in source region of 2016–2017 central italy event sequence. *Earthquake Spectra*, *34*(4), 1557–1583. https://doi.org/10.1193/101317EQS204M

Galli, P., Galadini, F., Pantosti, D.; Twenty years of paleoseismology in Italy, Earth-Science Reviews, Volume 88, Issues 1–2, (2008), Pages 89-117, ISSN 0012-8252, https://doi.org/10.1016/j.earscirev.2008.01.001.

Galvani, A., Anzidei, M., Devoti, R., Esposito, A., Pietrantonio, G., Pisani, A.R., Riguzzi, F., Serpelloni, E., (2013). The interseismic velocity field of the central Apennines from a dense GPS network. Ann Geophys-Italy 55. doi:10.4401/ag-5634

Gegout, P., Boy, J. P., Hinderer, J., & Ferhat, G. (2010). Modeling and Observation of Loading Contribution to Time-Variable GPS Sites Positions. In S. P. Mertikas (Ed.), *Gravity, Geoid*

and Earth Observation: IAG Commission 2: Gravity Field, Chania, Crete, Greece, 23-27 June 2008 (Vol. 135, pp. 651–659). Berlin, Heidelberg: Springer Berlin Heidelberg. https://doi.org/10.1007/978-3-642-10634-7_86

Gualandi, Adriano, Avouac, J.-P., Galetzka, J., Genrich, J. F., Blewitt, G., Adhikari, L. B., et al. (2016). Pre- and post-seismic deformation related to the 2015, Mw7.8 Gorkha earthquake, Nepal. *Tectonophysics*. https://doi.org/10.1016/j.tecto.2016.06.014

Gualandi, A, Serpelloni, E., & Belardinelli, M. E. (2014). Space-time evolution of crustal deformation related to the Mw 6.3, 2009 L'Aquila earthquake (central Italy) from principal component analysis inversion of GPS position time-series. *Geophysical Journal International*, *197*(1), 174–191. https://doi.org/10.1093/gji/ggt522

Gualandi, A, Serpelloni, E., & Belardinelli, M. E. (2016). Blind source separation problem in GPS time series. *Journal of Geodesy*, *90*(4), 323–341. https://doi.org/10.1007/s00190-015-0875-4

Gualandi, A, Liu, Z., & Rollins, C. (2020). Post-large earthquake seismic activities mediated by aseismic deformation processes. *Earth and Planetary Science Letters*, *530*, 115870. https://doi.org/10.1016/j.epsl.2019.115870

Hetland, E. A., & Zhang, G. (2014). Effect of shear zones on post-seismic deformation with application to the 1997 Mw 7.6 Manyi earthquake. *Geophysical Journal International*, *198*(1), 259–269. https://doi.org/10.1093/gji/ggu127

Huang, M., Fielding, E. J., Liang, C., Milillo, P., Bekaert, D., Dreger, D., & Salzer, J. (2017). Coseismic deformation and triggered landslides of the 2016 *M* 6.2 Amatrice earthquake in Italy. *Geophysical Research Letters*, *44*(3), 1266–1274. https://doi.org/10.1002/2016GL071687

Jolivet, L., Labrousse, L., Agard, P., Lacombe, O., Bailly, V., Lecomte, E., et al. (2010). Rifting and shallow-dipping detachments, clues from the Corinth Rift and the Aegean. *Tectonophysics*, *483*(3–4), 287–304. https://doi.org/10.1016/j.tecto.2009.11.001

Kositsky, A. P., & Avouac, J. P. (2010). Inverting geodetic time series with a principal component analysis-based inversion method. *Journal of Geophysical Research*, *115*(B3). https://doi.org/10.1029/2009JB006535

Lavecchia, Giusy & Federica, Ferrarini & Brozzetti, Francesco & Nardis, Rita & Boncio, Paolo & Chiaraluce, Lauro. (2012). From surface geology to aftershock analysis: Constraints on the

geometry of the L'Aquila 2009 seismogenic fault system. Italian Journal of Geosciences. 131. 330-347. 10.3301/IJG.2012.24.

Lavecchia, G., Castaldo, R., de Nardis, R., De Novellis, V., Ferrarini, F., Pepe, S., et al. (2016). Ground deformation and source geometry of the 24 August 2016 Amatrice earthquake (Central Italy) investigated through analytical and numerical modeling of DInSAR measurements and structural-geological data. *Geophysical Research Letters*, *43*(24), 12,389-12,398. https://doi.org/10.1002/2016GL071723

Maubant, L., Socquet, A., Hollingsworth, J., Pathier, E., & Pousse-Beltrán, L. (2017). The Seismic Sequence of the Norcia Earthquake, Italy 2016, seen by geodesy. In Cargese, 2nd of October – 6th of October 2017. France.

Michele, M., Chiaraluce, L., Di Stefano, R., & Waldhauser, F. (2020). Fine-scale structure of the 2016–2017 central italy seismic sequence from data recorded at the italian national network. *Journal of Geophysical Research: Solid Earth*, *125*(4). https://doi.org/10.1029/2019JB018440

Michel, S., Gualandi, A., & Avouac, J.-P. (2018). Interseismic coupling and slow slip events on the Cascadia megathrust. *Pure and Applied Geophysics*, 1–25. https://doi.org/10.1007/s00024-018-1991-x

Molinari, I., & Morelli, A. (2011). EPcrust: a reference crustal model for the European Plate. *Geophysical Journal International*, *185*(1), 352–364. https://doi.org/10.1111/j.1365-246X.2011.04940.x

Molinari, I., J. Verbeke, L. Boschi, E. Kissling, and A. Morelli (2015), Italian and Alpine three-dimensional crustal structure imaged by ambient-noise surface-wave dispersion, Geochem. Geophys. Geosyst., 16, 4405–4421, doi:10.1002/2015GC006176.

Munafò, I., Malagnini, L., & Chiaraluce, L. (2016). On the Relationship betweenM_w andM_L for Small Earthquakes. *Bulletin of the Seismological Society of America*, *106*(5), 2402–2408. https://doi.org/10.1785/0120160130

Nespoli, M., Belardinelli, M. E., & Bonafede, M. (2019). Fault dip variations related to elastic layering. *Geophysical Journal International*. https://doi.org/10.1093/gji/ggz505

Palano, M., Pezzo, G., Serpelloni, E., Devoti, R., D'Agostino, N., Gandolfi, S., et al. (2020). Geopositioning time series from offshore platforms in the Adriatic Sea. *Scientific Data*, *7*(1), 373. https://doi.org/10.1038/s41597-020-00705-w

Papadopoulos, G. A., Ganas, A., Agalos, A., Papageorgiou, A., Triantafyllou, I., Kontoes, C., et al. (2017). Earthquake Triggering Inferred from Rupture Histories, DInSAR Ground Deformation and Stress-Transfer Modelling: The Case of Central Italy During August 2016–January 2017. *Pure and Applied Geophysics*, *174*(10), 3689–3711. https://doi.org/10.1007/s00024-017-1609-8

Perfettini, H., & Avouac, J. P. (2007). Modeling afterslip and aftershocks following the 1992 Landers earthquake. *Journal of Geophysical Research*, *112*(B7). https://doi.org/10.1029/2006JB004399

Pintori, F., Serpelloni, E., Longuevergne, L., Garcia, A., Faenza, L., D'Alberto, L., et al. (2021). Mechanical response of shallow crust to groundwater storage variations: inferences from deformation and seismic observations in the eastern southern alps, italy. *Journal of Geophysical Research. Solid Earth*, *126*(2). https://doi.org/10.1029/2020JB020586

Pizzi, A., Galadini, F. Pre-existing cross-structures and active fault segmentation in the northern-central Apennines (Italy). Tectonophysics, Volume 476, Issues 1–2, 2009, Pages 304-319, ISSN 0040-1951, https://doi.org/10.1016/j.tecto.2009.03.018.

Pizzi, A., Di Domenica, A., Gallovič, F., Luzi, L., & Puglia, R. (2017). Fault segmentation as constraint to the occurrence of the main shocks of the 2016 central italy seismic sequence. *Tectonics*. https://doi.org/10.1002/2017TC004652

Platt, J. P., Behr, W. M., & Cooper, F. J. (2015). Metamorphic core complexes: windows into the mechanics and rheology of the crust. *Journal of the Geological Society*, *172*(1), 9–27. https://doi.org/10.1144/jgs2014-036

Porreca, M., Minelli, G., Ercoli, M., Brobia, A., Mancinelli, P., Cruciani, F., et al. (2018). Seismic Reflection Profiles and Subsurface Geology of the Area Interested by the 2016-2017 Earthquake Sequence (Central Italy). *Tectonics*, *37*(4), 1116–1137. https://doi.org/10.1002/2017TC004915

Pousse-Beltran, L., Socquet, A., Benedetti, L., Doin, M., Rizza, M., & D'Agostino, N. (2020). Localized afterslip at geometrical complexities revealed by insar after the 2016 central italy seismic sequence. *Journal of Geophysical Research: Solid Earth*, *125*(11). https://doi.org/10.1029/2019JB019065

Pucci, S., De Martini, P. M., Civico, R., Villani, F., Nappi, R., Ricci, T., et al. (2017). Coseismic ruptures of the 24 August 2016, *M* 6.0 Amatrice earthquake (central Italy). *Geophysical*

Research Letters, *44*(5), 2138–2147. https://doi.org/10.1002/2016GL071859

Pushpalatha, R., Perrin, C., Le Moine, N., Mathevet, T., & Andréassian, V. (2011). A downward structural sensitivity analysis of hydrological models to improve low-flow simulation. *Journal of Hydrology*, *411*(1–2), 66–76. https://doi.org/10.1016/j.jhydrol.2011.09.034

Rabillard, A., Jolivet, L., Arbaret, L., Bessière, E., Laurent, V., Menant, A., et al. (2018). Synextensional granitoids and detachment systems within cycladic metamorphic core complexes (aegean sea, greece): toward a regional tectonomagmatic model. *Tectonics*, *37*(8), 2328–2362. https://doi.org/10.1029/2017TC004697

Radiguet, M., Cotton, F., Vergnolle, M., Campillo, M., Valette, B., Kostoglodov, V., & Cotte, N. (2011). Spatial and temporal evolution of a long term slow slip event: the 2006 Guerrero Slow Slip Event. *Geophysical Journal International*, *184*(2), 816–828. https://doi.org/10.1111/j.1365-246X.2010.04866.x

Ragon, T., Sladen, A., & Simons, M. (2019). Accounting for uncertain fault geometry in earthquake source inversions – II: application to the Mw 6.2 Amatrice earthquake, central Italy. *Geophysical Journal International*, *218*(1), 689–707. https://doi.org/10.1093/gji/ggz180

Riva, R. E. M., Borghi, A., Aoudia, A., Barzaghi, R., Sabadini, R., & Panza, G. F. (2007). Viscoelastic relaxation and long-lasting after-slip following the 1997 Umbria-Marche (Central Italy) earthquakes. *Geophysical Journal International*, *169*(2), 534–546. https://doi.org/10.1111/j.1365-246X.2007.03315.x

Roberts, S., & Choudrey, R. (2003). Data decomposition using independent component analysis with prior constraints. *Pattern Recognition*, *36*(8), 1813–1825. https://doi.org/10.1016/S0031-3203(03)00002-5

Rodell, M., Houser, P. R., Jambor, U., Gottschalck, J., Mitchell, K., Meng, C. J., et al. (2004). The global land data assimilation system. *Bulletin of the American Meteorological Society*, *85*(3), 381–394. https://doi.org/10.1175/BAMS-85-3-381

Rovida, A. N., Locati, M., Camassi, R. D., Lolli, B., & Gasperini, P. (2019). Catalogo Parametrico dei Terremoti Italiani CPTI15, versione 2.0. https://doi.org/10.13127/CPTI/CPTI15.2

Sani, F., Vannucci, G., Boccaletti, M., Bonini, M., Corti, G., & Serpelloni, E. (2016). Insights into the fragmentation of the Adria Plate. *Journal of Geodynamics*, *102*, 121–138. https://doi.org/10.1016/j.jog.2016.09.004

Scognamiglio, L., Tinti, E., Casarotti, E., Pucci, S., Villani, F., Cocco, M., et al. (2018). Complex

fault geometry and rupture dynamics of the m_w 6.5, 30 october 2016, central italy earthquake. *Journal of Geophysical Research: Solid Earth*, *123*(4), 2943–2964. https://doi.org/10.1002/2018JB015603

Serpelloni, Enrico, Faccenna, C., Spada, G., Dong, D., & Williams, S. D. P. (2013). Vertical GPS ground motion rates in the Euro-Mediterranean region: New evidence of velocity gradients at different spatial scales along the Nubia-Eurasia plate boundary. *Journal of Geophysical Research: Solid Earth*, *118*(11), 6003–6024. https://doi.org/10.1002/2013JB010102

Serpelloni, E, Pintori, F., Gualandi, A., Scoccimarro, E., Cavaliere, A., Anderlini, L., et al. (2018). Hydrologically Induced Karst Deformation: Insights From GPS Measurements in the Adria-Eurasia Plate Boundary Zone. *Journal of Geophysical Research: Solid Earth*, *123*(5), 4413–4430. https://doi.org/10.1002/2017JB015252

Serpelloni, E., Casula, G., Galvani, A., Anzidei, M., & Baldi, P. (2006). Data analysis of Permanent GPS networks in Italy and surrounding region: application of a distributed processing approach. Annales de Geophysique, 49, 897–928. https://doi.org/10.4401/ag-4410

Silverii, F., D'Agostino, N., Métois, M., Fiorillo, F., & Ventafridda, G. (2016). Transient deformation of karst aquifers due to seasonal and multiyear groundwater variations observed by GPS in southern Apennines (Italy). *Journal of Geophysical Research: Solid Earth*, *121*(11), 8315–8337. https://doi.org/10.1002/2016JB013361

Tarantola, A., 2005. Inverse Problem Theory and Methods for Model Parameter Estimation. SIAM.

Tesauro, M., M. K. Kaban, and S. A. P. L. Cloetingh (2008), EuCRUST-07: A new reference model for the European crust, Geophys. Res. Lett., 35, L05313, doi:10.1029/2007GL032244.

Tinti, E., Scognamiglio, L., Michelini, A., & Cocco, M. (2016). Slip heterogeneity and directivity of the *M* 6.0, 2016, Amatrice earthquake estimated with rapid finite-fault inversion. *Geophysical Research Letters*, *43*(20), 10,745-10,752. https://doi.org/10.1002/2016GL071263

Tregoning, P. (2005). Effects of atmospheric pressure loading and seven-parameter transformations on estimates of geocenter motion and station heights from space geodetic observations. *Journal of Geophysical Research*, *110*(B3). https://doi.org/10.1029/2004JB003334

Valoroso, L., Chiaraluce, L., Piccinini, D., Di Stefano, R., Schaff, D., & Waldhauser, F. (2013). Radiography of a normal fault system by 64,000 high-precision earthquake locations: The 2009 L'Aquila (central Italy) case study. *Journal of Geophysical Research: Solid Earth*, *118*(3), 1156–1176. https://doi.org/10.1002/jgrb.50130

Verdecchia, A., Pace, B., Visini, F., Scotti, O., Peruzza, L., & Benedetti, L. (2018). The Role of Viscoelastic Stress Transfer in Long-Term Earthquake Cascades: Insights After the Central Italy 2016-2017 Seismic Sequence. *Tectonics*, *37*(10), 3411–3428. https://doi.org/10.1029/2018TC005110

Vičič, B., Aoudia, A., Borghi, A., Momeni, S., & Vuan, A. (2020). Seismicity rate changes and geodetic transients in central apennines. *Geophysical Research Letters*, *47*(22). https://doi.org/10.1029/2020GL090668

Villani, F., Civico, R., Pucci, S., Pizzimenti, L., Nappi, R., De Martini, P. M., & Open EMERGEO Working Group. (2018). A database of the coseismic effects following the 30 October 2016 Norcia earthquake in Central Italy. *Scientific Data*, *5*, 180049. https://doi.org/10.1038/sdata.2018.49

Vuan, A., Sugan, M., Chiaraluce, L., & Di Stefano, R. (2017). Loading rate variations along a midcrustal shear zone preceding the *m* 6.0 earthquake of 24 august 2016 in central italy. *Geophysical Research Letters*, *44*(24). https://doi.org/10.1002/2017GL076223

Walters, R. J., Gregory, L. C., Wedmore, L. N. J., Craig, T. J., McCaffrey, K., Wilkinson, M., et al. (2018). Dual control of fault intersections on stop-start rupture in the 2016 Central Italy seismic sequence. *Earth and Planetary Science Letters*, *500*, 1–14. https://doi.org/10.1016/j.epsl.2018.07.043

Wang, L., Gao, H., Feng, G., & Xu, W. (2018). Source parameters and triggering links of the earthquake sequence in central Italy from 2009 to 2016 analyzed with GPS and InSAR data. *Tectonophysics*, *744*, 285–295. https://doi.org/10.1016/j.tecto.2018.07.013

Watkins, M. M., Wiese, D. N., Yuan, D.-N., Boening, C., & Landerer, F. W. (2015). Improved methods for observing Earth's time variable mass distribution with GRACE using spherical cap mascons. *Journal of Geophysical Research: Solid Earth*, *120*(4), 2648–2671. https://doi.org/10.1002/2014JB011547

Xu, G., Xu, C., Wen, Y., & Jiang, G. (2017). Source Parameters of the 2016–2017 Central Italy Earthquake Sequence from the Sentinel-1, ALOS-2 and GPS Data. *Remote Sensing*, *9*(11),

1182. https://doi.org/10.3390/rs9111182

References from Supporting Information

Altamimi, Z., Collilieux, X., & Métivier, L. (2011). ITRF2008: An improved solution of the international terrestrial reference frame. Journal of Geodesy, 85, 457–473. https://doi.org/10.1007/s00190-011-0444-4

Bevis, M., Brown, A., 2014. Trajectory models and reference frames for crustal motion geodesy. J Geodesy 88, 283–311. doi:10.1007/s00190-013-0685-5

Boehm, J., Heinkelmann, R., & Schuh, H. (2007). Short note: A global model of pressure and temperature for geodetic applications. Journal of Geodesy, 81, 679–683. https://doi.org/10.1007/s00190-007-0135-3

Dong, D., Fang, P., Bock, Y., Webb, F., Prawirodirdjo, L., Kedar, S., & Jamason, P. (2006). Spatiotemporal filtering using principal component analysis and Karhunen-Loeve expansion approaches for regional GPS network analysis. Journal of Geophysical Research, 111, B03405. (B4),2075 https://doi.org/10.1029/2005JB003806

Dong, D., Herring, T., & King, R. (1998). Estimating regional deformation from a combination of space and terrestrial geodetic data. Journal of Geodesy, 72(4), 200–214. https://doi.org/10.1007/s001900050161

Herring, T. A., King, R. W., Floyd, M. A., & McClusky, S. C. (2018). Introduction to GAMIT/GLOBK, Release 10.7. Retrieved from http://geoweb.mit.edu/gg/Intro_GG.pdf

Lagler, K., Schindelegger, M., Böhm, J., Krásná, H., & Nilsson, T. (2013). GPT2: Empirical slant delay model for radio space geodetic techniques. Geophysical Research Letters, 40, 1069–1073. https://doi.org/10.1002/grl.50288

Lyard, F., Lefevre, F., Letellier, T., & Francis, O. (2006). Modelling the global ocean tides: Modern insights from FES2004. Ocean Dynamics,56, 394–415. https://doi.org/10.1007/s10236-006-0086-x

Petrie, E. J., King, M. A., Moore, P., & Lavallée, D. A. (2010). Higher-order ionospheric effects on the GPS reference frame and velocities. Journal of Geophysical Research, 115, B03417. https://doi.org/10.1029/2009JB006677

Schmid, R., Rothacher, M., Thaller, D., & Steigenberger, P. (2005). Absolute phase center

corrections of satellite and receiver antennas. GPS Solutions, 9, 283–293. https://doi.org/10.1007/s10291-005-0134-x

Schmid, R., Steigenberger, P., Gendt, G., Ge, M., & Rothacher, M. (2007). Generation of a consistent absolute phase-center correction model for GPS receiver and satellite antennas. Journal of Geodesy, 81, 781–798. https://doi.org/10.1007/s00190-007-0148-y

Tape, C., Musé, P., Simons, M., Dong, D., Webb, F., 2009. Multiscale estimation of GPS velocity fields. Geophysical Journal International 179, 945–971. doi:10.1111/j.1365-246X.2009.04337.x

Journal of Geophysical Research: Solid Earth

Supporting information for

Post-Seismic Deformation Related to the 2016 Central Italy Seismic Sequence from GPS Displacement Time-Series

E. Mandler[1], *L. Anderlini*[2], *A. Gualandi*[3], *F. Pintori*[3], *E. Serpelloni*[3] and *M. E. Belardinelli*[1]

1: Dipartimento di Fisica e Astronomia, Settore di Geofisica, Università di Bologna, Bologna, Italy

2: Istituto Nazionale di Geofisica e Vulcanologia (INGV), Bologna, Italy,

3: Istituto Nazionaledi Geofisica e Vulcanologia (INGV), Osservatorio Nazionale Terremoti, Italy

Contents of this file

Introduction

The supporting information details some methodology and presents some intermediate results.

S1. GNSS data analysis

S.1.1. GNSS dataset and data processing

The position time-series have been obtained adopting a three-step procedure approach, as in Serpelloni et al. (2006, 2018), that includes: 1) raw phase data reduction, 2) combination of loosely constrained network solutions and reference frame definition and 3) time-series analysis, including velocity estimates and spatial filtering of common mode errors.

The raw GPS observables have been analyzed using the 10.70 version of the GAMIT/GLOBK package (Herring et al., 2018) adopting standards defined in the framework of the IGS “Repro2 campaign” (http://acc.igs.org/reprocess2.html). The GAMIT software is used to estimate station positions, atmospheric delays, satellite orbits, and Earth orientation parameters from ionosphere-free linear combination of GPS phase observables using double differencing techniques to eliminate phase biases caused by drifts in the satellite and receiver clock oscillators. GPS pseudo-range observables are used to constrain clock timing offsets and to improve automated editing of the phase data, assisting in the resolution of integer phase ambiguities. GPS phase data are weighted according to an elevation-angle-dependent error model (Herring et al., 2018) using an iterative analysis procedure whereby the elevation dependence is determined from the observed scatter of phase residuals. In this analysis the satellites orbit parameters are tightly constrained to the IGS final products. We use the IGS absolute antenna phase center model for both satellite and ground-based antennas, which improves the accuracy of estimates for the vertical components of site position by mitigating reference frame scale and atmospheric mapping function errors (Schmid et al., 2005, 2007). While the first-order ionospheric delay is eliminated by the ionosphere-free linear combination, the second-order ionospheric corrections are applied based on the formulation of (Petrie et al., 2010), using IONEX files from the Center for Orbit Determination in Europe (CODE). The tropospheric delay is modeled as piecewise linear model and estimated using the Vienna Mapping Function 1 (VMF1; Boehm et al., 2007) with a 10° cutoff. We use the Global Pressure and Temperature 2 (GPT2; Lagler et al., 2013) model to provide a priori hydrostatic delays. The pole tide was also corrected in GAMIT by IERS standards. The Earth Orientation Parameters (EOP) are tightly constrained to priori values obtained from IERS Bulletin B. Non-tidal atmospheric loading and ocean tidal loading

are corrected using MIT filtered atmospheric displacements files (available at ftp://everest.mit.edu/pub/GRIDS) and the FES2004 (Lyard et al., 2006) model, respectively. The International Earth Rotation Service (IERS) 2003 model for diurnal and semidiurnal solid Earth tides was set. Because of the large number of stations included in our Euro-Mediterranean GPS processing (~3000), this step is performed for several sub-networks, each made by <50 stations, with each sub-network sharing a set of high-quality IGS stations, which are used as tie-stations in the combination step.

In the second step we use the ST_FILTER program of the QOCA software (http://qoca.jpl.nasa.gov), which adopts a Kalman filter estimation algorithm (Dong et al., 1998, 2002), to combine all the daily loosely constrained solutions with the global solution of the IGS network made available by MIT (http://sopac.ucsd.edu), and simultaneously realize a global reference frame by applying generalized constraints (Dong et al., 1998). Specifically, we define the reference frame by minimizing the velocities of the IGS core stations (http://igscb.jpl.nasa.gov), while estimating a seven- parameter transformation with respect to the GPS realization of the ITRF2008 frame (Altamimi et al., 2011), i.e., the IGb08 reference frame.

In the third step we analyze the position time series in order to perform de-trending and filtering of common mode noise signals, and realize the displacement time-series to be used as input of the vbICA (see Section 2.1). Because of the presence of non-linear signals (i.e., the post-seismic transients) and of short time-series (e.g., those installed soon after the Amatrice mainshock) for which the linear tectonic trend is difficult to determine, we use a constrained non-linear least-squares estimator, with linear trends constrained to apriori values. We model the time-series with a classic trajectory model (Bevis & Brown, 2014) estimating for offsets due to stations equipment changes and earthquakes, annual and semi-annual periodic signals, a linear velocity term and an exponential term describing the post-seismic transient displacements. Remarkably, in order to remove the linear trend from short time series (with the first epoch after 2013), an interpolated velocity field was constructed by modeling the velocities of those stations having time series longer than 5 yrs adopting a multiscale approach (Tape et al., 2009). These modeled values are used as a-priori velocities in the time-series analysis. Hence, for short time series, the linear trend was constrained to be close to the a-priori value (in a range of ±30% for the horizontal components, and ±50% for the vertical component); whereas for long time series (first epoch prior to 2013) it is left as a free parameter. In order to better assess the offsets, the estimate is forced to be close to the difference between the median value of the few positions after the jump and the median value of the few positions prior to it in a range of ± the mean value

of displacement errors. This can help in better constraining the offset that could otherwise affect the post-seismic assessment. The model derived from the combination of these signals (red lines in Fig. S1) is then subtracted from the position time series in order to get the residual positions. The residual time-series are then used to estimate the Common Mode Error (CME) performing a Principal Component Analysis (PCA), as described in Dong et al. (2006). The PCA is performed at a continental-scale, over the same area used by Serpelloni et al. (2013), and the first two PCs are here considered as CME. Moreover, during this step, all GPS stations interested by past earthquakes have been excluded from the PCA. This prevents the removal of the eventual more localized signals of geophysical interests recorded by the GPS stations in the study region, since the PCA detects the signals common to a much larger region. As a result, after removing the CME, the typical repeatability in our analysis is ~1 mm for the horizontal components, and ~3 mm for the vertical component, with a 30% gain in the daily repeatability and a significant improvement of the signal to noise ratio. After the spatial filtering, the estimated seasonal motions are added back to the filtered time-series, obtaining position time series with a reduced scatter around the adopted model which are used as input of the blind source separation analysis performed with the vbICA method (see Section 2.1).

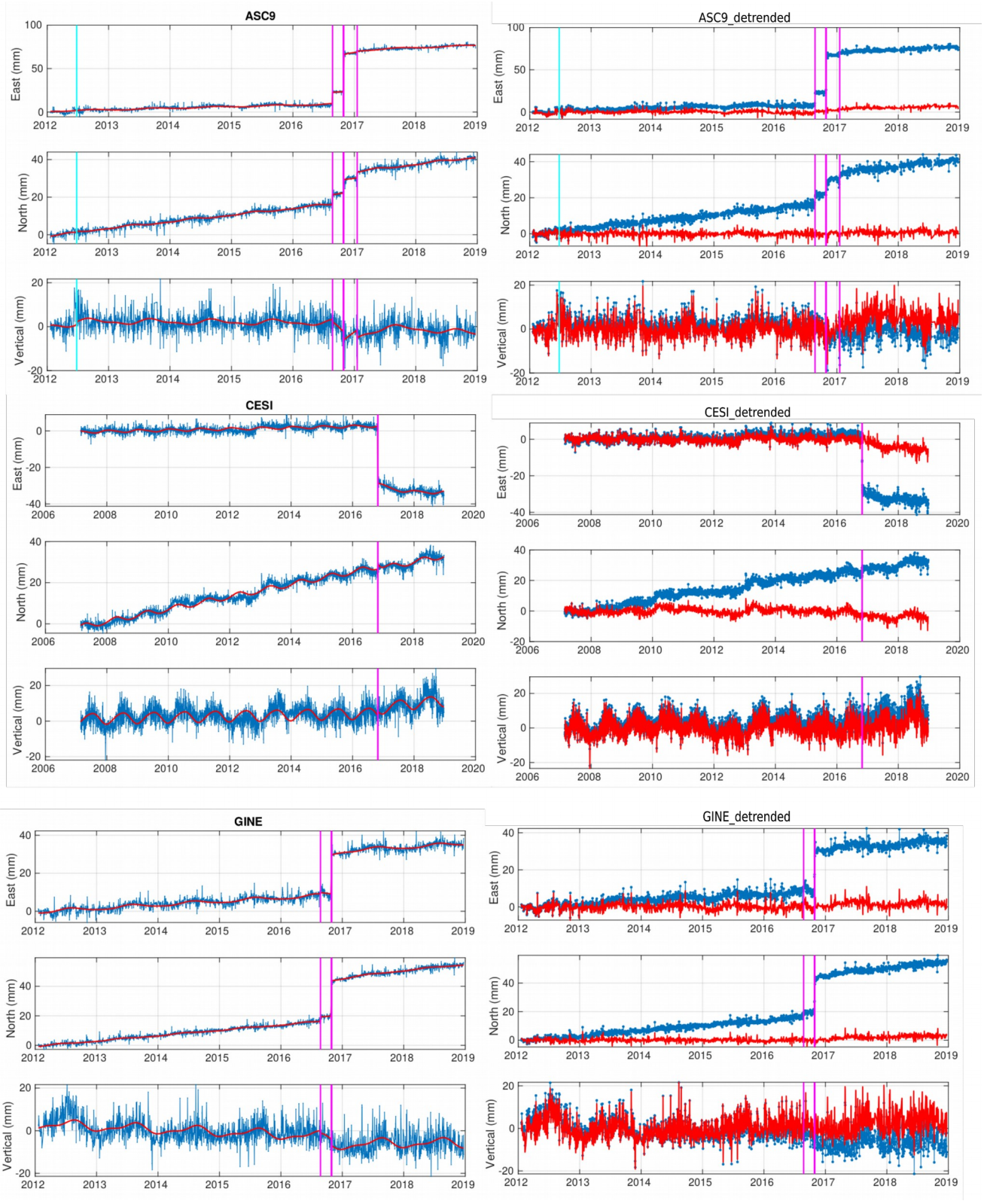

Figure S1. Left column panels show an example of fit to the time-series of ASC9, CESI and GINE sites (red lines); right column shows the raw time-series (light blue curves) and the detrended time-series (red curves) for the same sites. Magenta vertical lines mark the earthquakes epoch, whereas light blue vertical lines the instrumental offsets epoch.

S.1.2. ICA uncertainty

In this section we describe the novel procedure adopted in this study to associate a more realistic uncertainty with the independent components. We proceed as follows: we perform 100 ICA decompositions, each time randomly perturbing the original GPS time series assuming a nominal Gaussian uncertainty at each available epoch. We refer to these 100 decompositions as ICA_{rand}. Differently from the more common Principal Component Analysis (PCA), a problem with the ICA is that the ordering of the ICs is not well defined. Fortunately, the extracted ICs are sufficiently robust with respect to the random perturbations imposed, and we can thus sort the ICs ordering them on the base of the correlation between their temporal sources and the original sources obtained not perturbing the data (i.e. the decomposition shown in Figures 3A and 4 of main text). We estimate the uncertainty on the spatial pattern U, the weights Sigma and the temporal functions V considering how spread their values are across the 100 decompositions. In practice, we calculate the sample variance for each element of each matrix. This procedure provides larger uncertainties with respect to those outputted by the vbICA code, and we consider them to reflect more realistically the uncertainty in the data.

S2. Pre-seismic analysis

In this section we show the components retrieved by the analysis of the pre-seismic phase of the Amatrice-Visso-Norcia seismic sequence. The time dependence of the independent components (Fig. S2 panel a, b, c, d) does not highlight the occurrence of any geodetic transient; their spatial response (lower panel) is generally sparse and it does not support the presence of any ongoing localized tectonic process in the preparatory phase of the 2016-2017 seismic sequence.

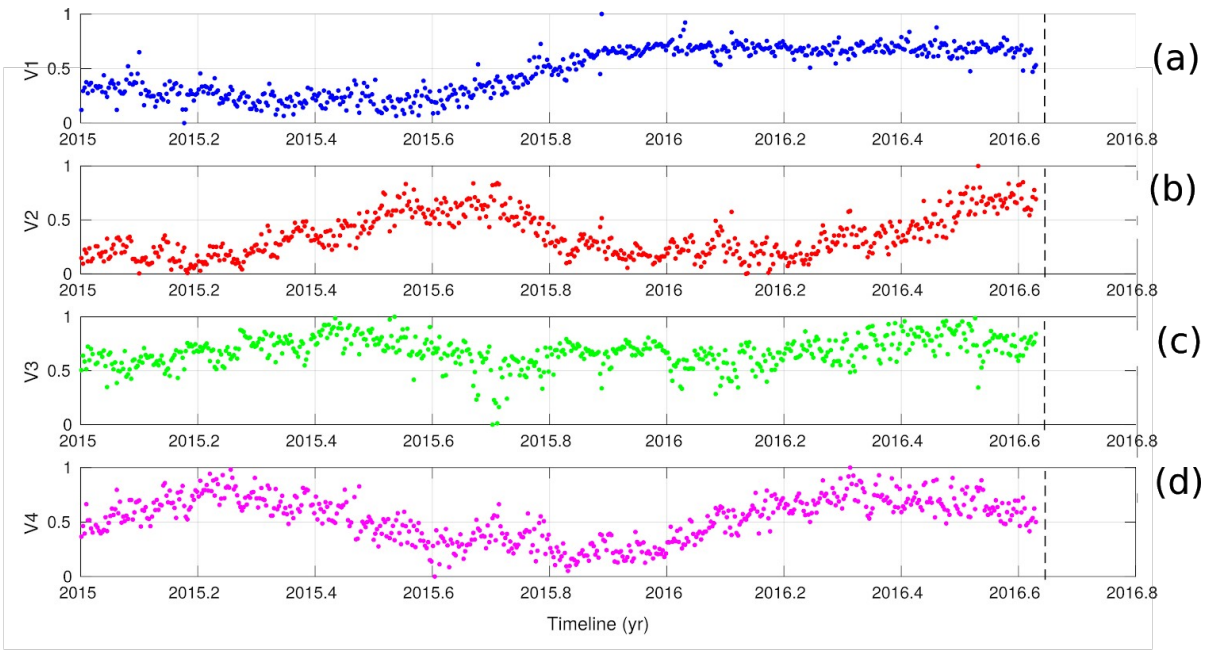
V1
V2
V3
V4
(a)
(b)
(c)
(d)
2015
2015.2
2015.4
2015.6
2015.8
2016
2016.2
2016.4
2016.6
2016.8
Timeline (yr)

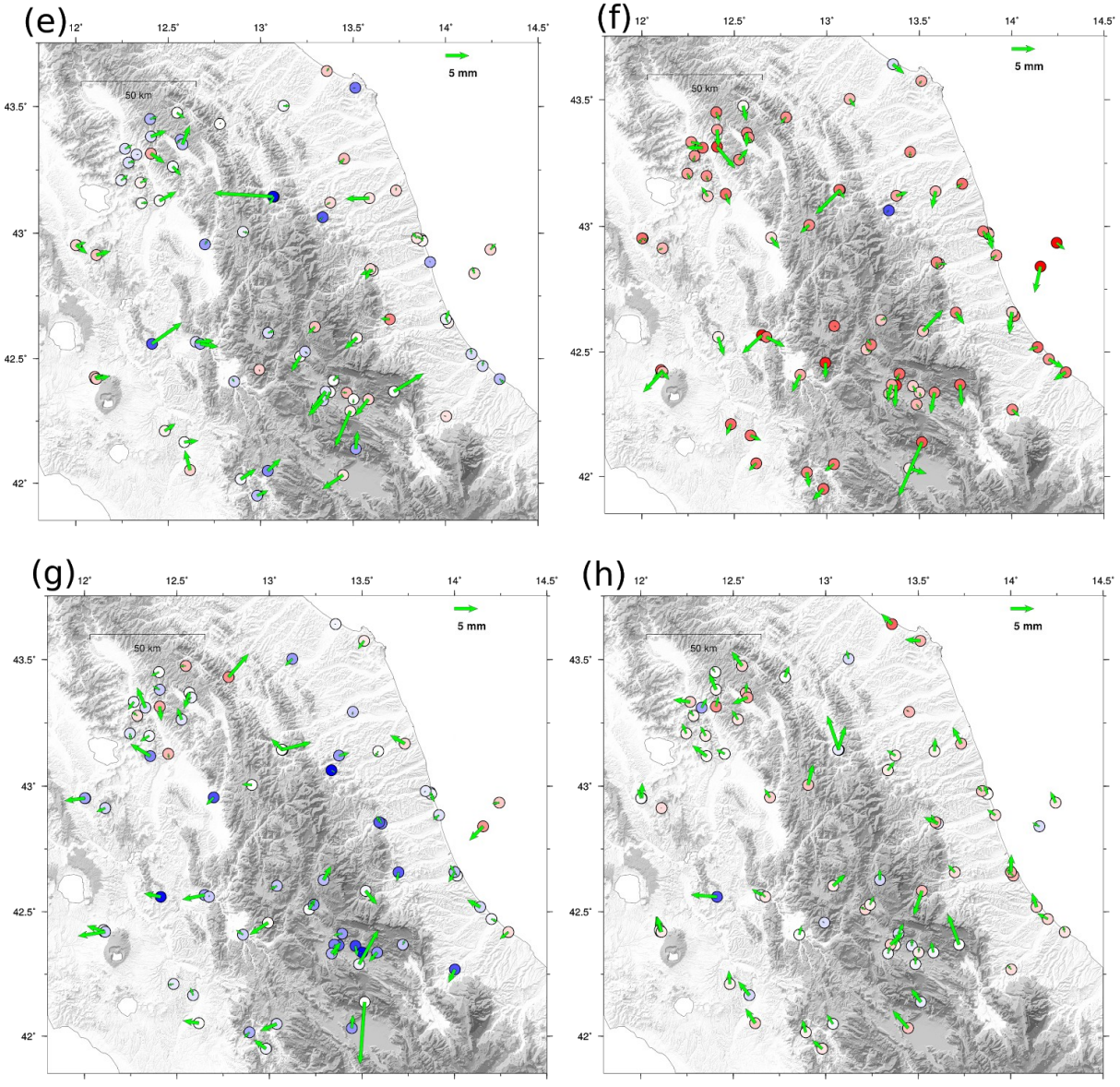
(e)
(f)
(g)
(h)
5 mm
50 km
12°
12.5°
13°
13.5°
14°
14.5°
43.5°
43°
42.5°
42°

Fig. S2. Temporal evolution and dimensional spatial response of IC1 (a, e), IC2 (b, f), IC3 (c, g), IC4 (d, h) of the analysis on the pre-seismic phase (time span 2015-2016.64). Vertical dashed lines in panels (a, b, c, d) mark the 24th of August mainshock. In the lower panels the spatial responses to the sources of deformation are given in mm.

S3. Hydrological analysis

Figure S3 shows the 5 hydrological basins considered, defined using the drainage direction maps (www.hydrosheds.org/page/availability) and watershed outlets located at the river discharge measurements on the Tevere, Nera, Tronto, Pescara and Aterno rivers.

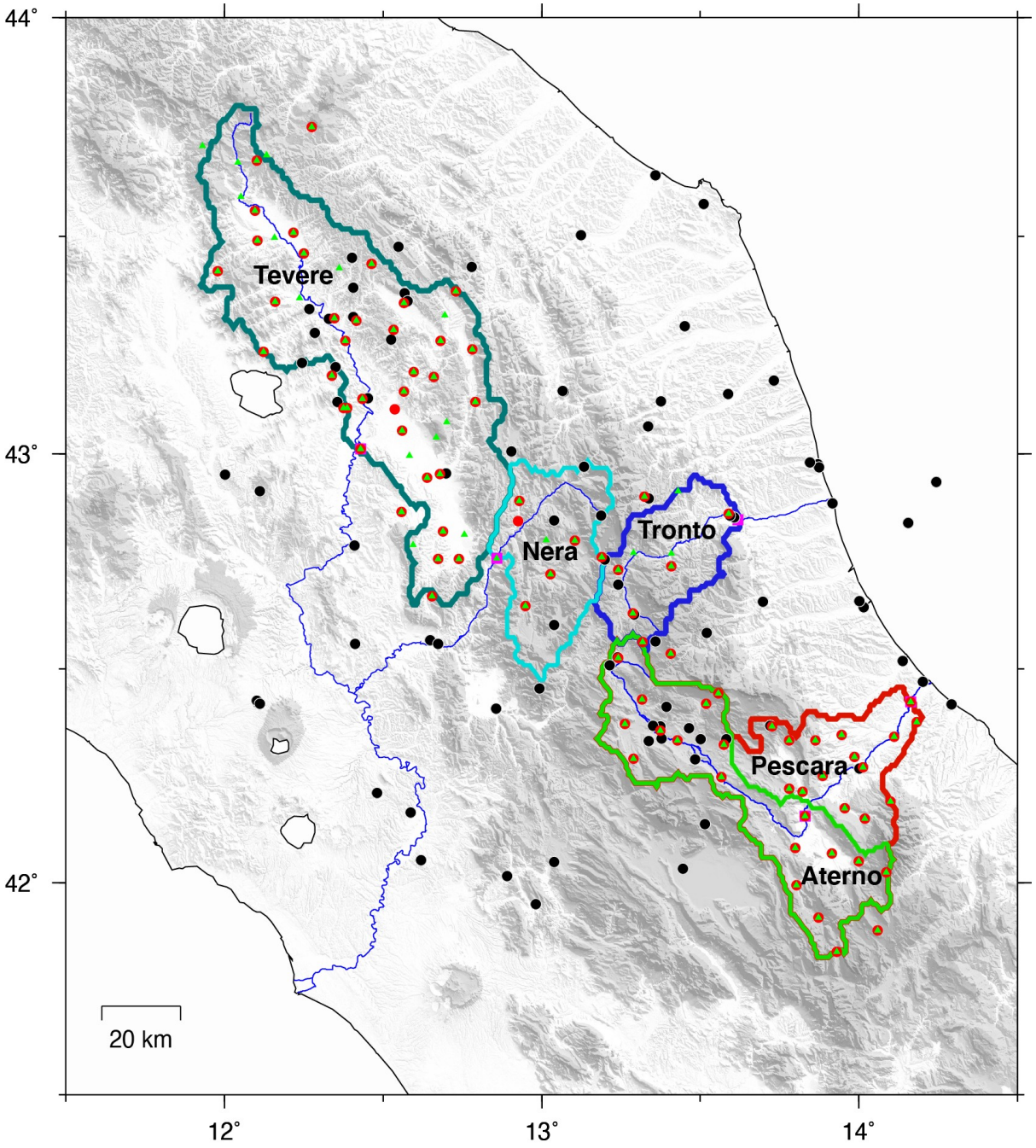

Figure S3. Hydrological basins of the Tevere (dark green), Nera (cyan), Tronto (blue), Aterno (light green), Pescara (red) rivers. Black dots: GNSS stations; purple squares: river gauging stations; green triangles: pluviometers; red circles: thermometers.

The Tables S1 and S2 show the cross-correlation between TWS and V3, V4 (Fig. 6 main text) respectively. The time lag that maximizes the correlation is reported, too.

Hydrological Basin	Pearson Correlation Coefficient TWS - V3	Lag (days)
Tevere	0.7077	110
Tronto	0.7528	93

Pescara	0.7374	79
Aterno	0.7606	63
Nera	0.7404	82

Table S1. Pearson cross-correlation coefficient between TWS computed in the hydrological basins and V3 (Fig. 6 main text). TWS anticipates V3 by a number of days estimated in the third column. Both TWS and V3 have been detrended.

Hydrological Basin	Pearson Correlation Coefficient TWS - V4	Lag (days)
Tevere	0.4831	20
Tronto	0.4144	8
Pescara	0.3043	6
Aterno	0.2128	9
Nera	0.2163	10

Table S2. Pearson cross-correlation coefficient between TWS computed in the hydrological basins and V4 (Fig. 6 main text). TWS anticipates V4 by a number of days estimated in the third column. Both TWS and V4 have been detrended.

S4. Post-seismic re-analysis

In this section we show the results for the vbICA performed on the residual time series where the hydrological components, described in Section 3 of the main text, are removed from the original time series. Since we are focusing our attention on the post-seismic phase only, we analyze the time span 2016-2019, and the vbICA is performed by fixing the number of ICs L=3 as suggested by an F-test. In the following images we show the results of this decomposition: the post-seismic relaxation is still clear (IC1, Fig. S4) and it explains the majority of the variance of the data (S_1=1523 mm); the second component (IC2, Fig. S5) shows a non monotonic evolution that does not match with what we observe in the post-seismic time series. Moreover its relative importance in explaining the data variance is limited (S_2=403 mm), therefore we neglect it as a contributing source of the post-seismic relaxation. The IC3 (Fig. S6) shows a periodical behaviour in its temporal part and for this reason we consider it as due to incomplete correction of the hydrological signals.

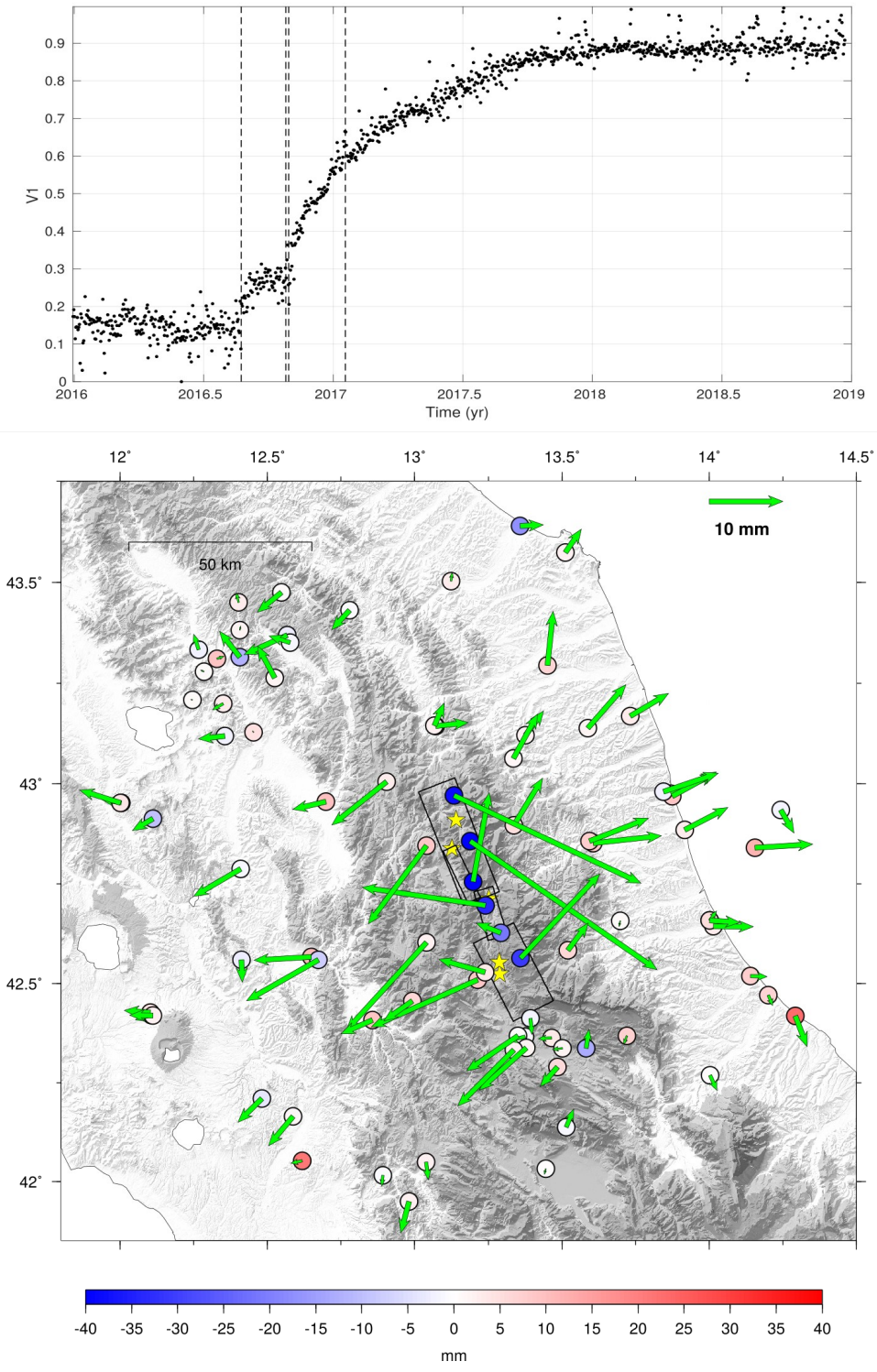

Fig S4. The IC1 (upper panel = temporal evolution, lower panel = spatial pattern) of the analysis on the post-seismic phase of the time series filtered from the hydrological components. Yellow stars show the epicenters of the mainshocks while the black boxes show the location of the faults responsible for the 2016-2017 sequence as in Cheloni et al. (2017, 2019).

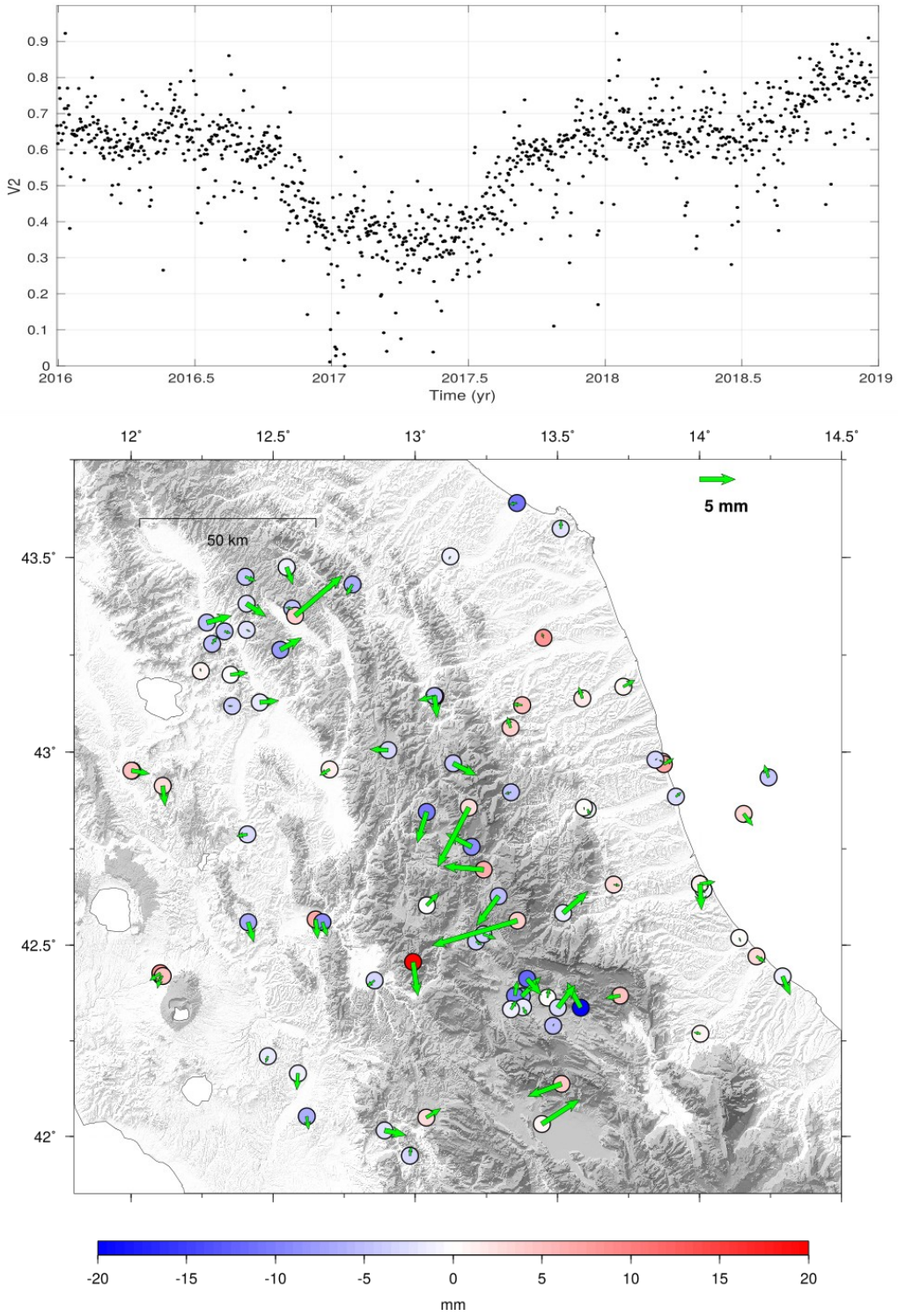

Fig S5. The IC2 (upper panel = temporal evolution, lower panel = spatial pattern) of the analysis on the post-seismic phase of the time series filtered from the hydrological components.

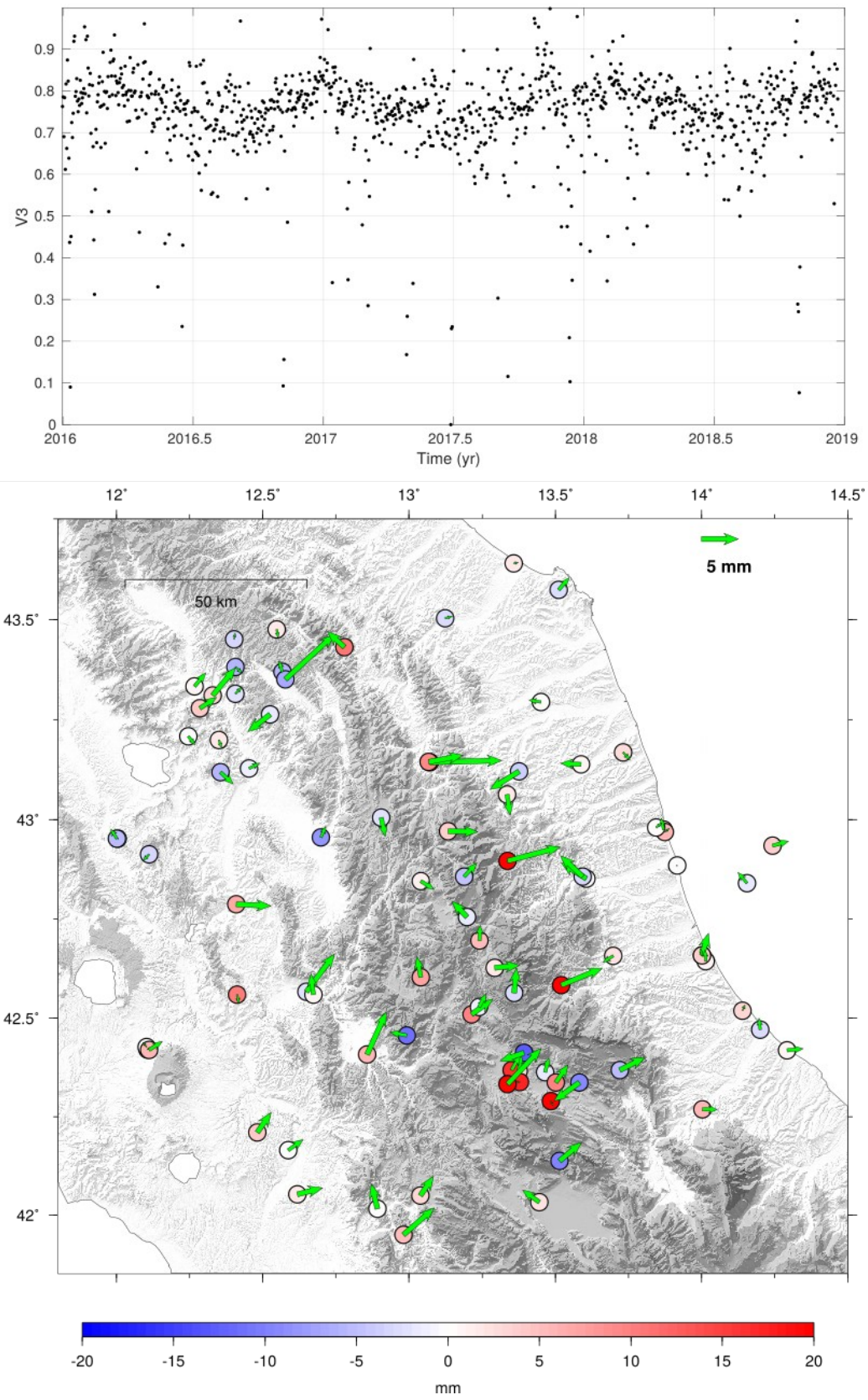

Fig S6. The IC3 (upper panel = temporal evolution, lower panel = spatial pattern) of the analysis on the post-seismic phase of the time series filtered from the hydrological components.

S5- Paganica sites: post-seismic separation and effects on the slip inversion

In this section we show the importance of a correct separation among tectonic and non-tectonic sources for the sites in the Paganica area, and how the post-seismic displacement associated with these sites implies the inclusion of the Paganica fault in the inversion. GPS stations in the Paganica area are heavily affected by the IC3 (Fig. 4 main text) as it is quite clear from the raw time-series (Fig. S7); however to neglect a post-seismic contribution to the total displacement leads to a bad data modelization (fig. S7). To double check this fact we subtracted the hydrological ICs from the raw data. The residuals show a mm-scale post-seismic transient (fig. S8) consistent with the spatial displacement associated with the IC1 (fig. 4a main text). Once we have validated the separation of the post-seismic displacement associated with the sites in the Paganica area, we show that such displacement requires to include the Paganica fault in the inversion (Fig. S9), which is carried out following the procedure described in Section 4 of main text. We notice from Figure S9a the strong concentration of slip (up to 35 cm) on the southern edge of the Campotosto fault which is likely driven by the position of the GPS sites with respect to the fault. Despite the presence of such concentration of slip, we notice that the displacement at the Paganica sites is largely underestimated (Fig. S9b).

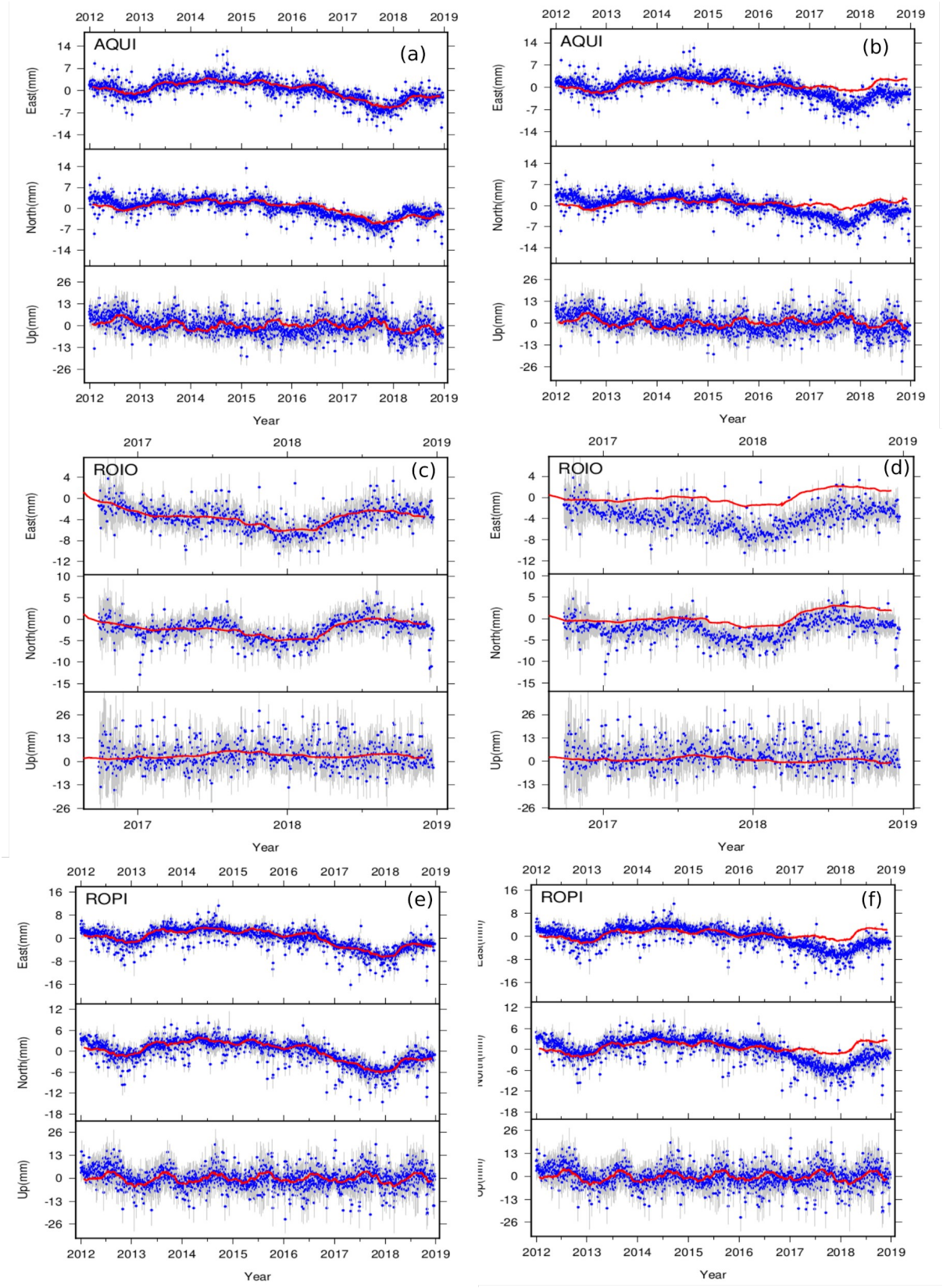

Fig S7. Comparison of AQUI, ROIO, ROPI time-series reconstruction using all of the ICs (panels a, c, e) and using only the non-tectonic components (panels b, d, f). Blue dots show the raw data while red lines the ICA modelization.

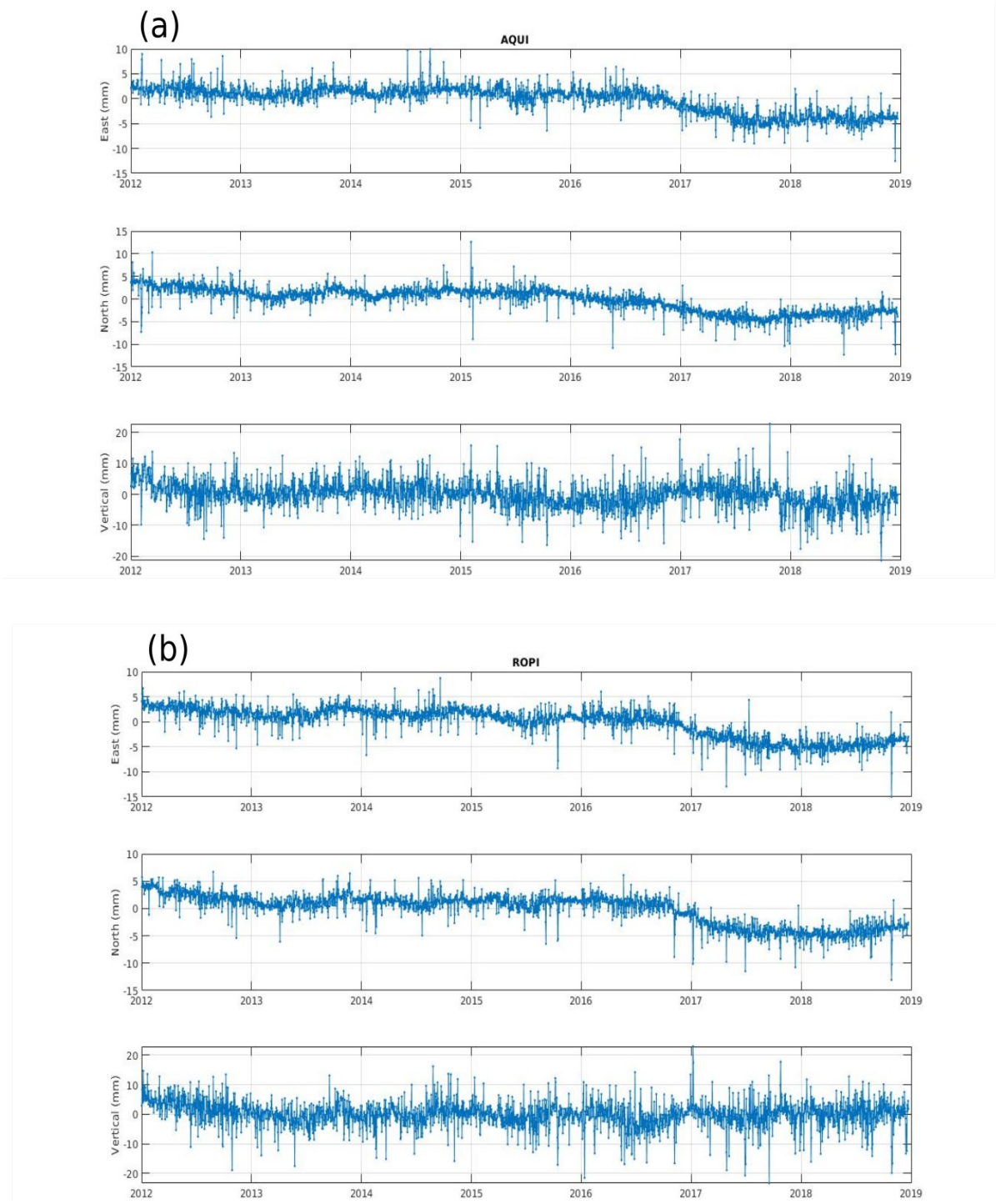

Fig S8. In figure the residuals among the raw time series and the IC 2, 3, 4, for the GPS stations AQUI (a), ROPI (b). In the post-seismic phase they show a mm-scale deformation prevalently SW-oriented, consistent with the direction and intensity of the spatial part of the IC1.

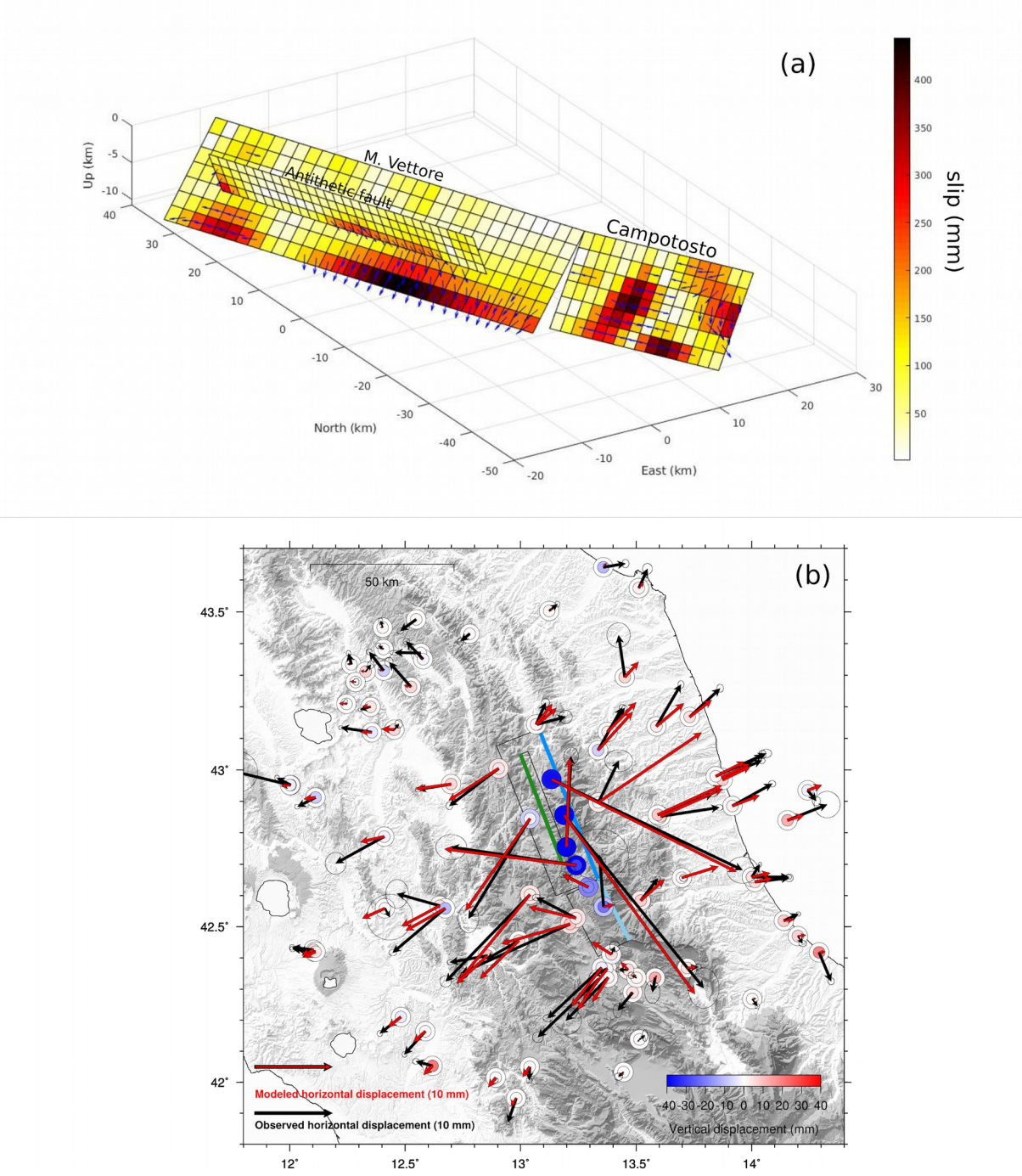

Figure S9. (a): Slip distribution on the M. Vettore fault, the antithetic fault and the Campotosto fault; (b): map of the data modelization for the inversion with the Paganica fault not included. Faults' traces are colored as in Figure 8 of the main text.

S6. Far- and Near-field separation

To discriminate between near and far fields, namely which stations are more affected by slip on

faults, we proceed as follows. We solve the forward problem relative to a 60 km long, 10 km deep, rectangular fault plane uniformly slipping by 1 m and embedded in a homogeneous elastic half-space. This dislocation represents an along-strike extension of the major structures described in Cheloni et al. (2017, 2019), centered on the seismicity pattern that followed the seismic sequence (Figure S10a). The calculated displacement at the GPS locations basically consists in the Green's function response, and it is made of a three components vector per station j: $Gj=[G_{je}, G_{jn}, G_{ju}]^T$, j=1, ..., N_{stn}. We compare the L2 norm of such vector normalized by the maximum value retrieved for all the stations, $gj = |Gj| / \max\{|Gi|\}_{i=1}^{Nstn}$ for $j=1,..,N_{stn}$, with the normalized L2 norm relative to the spatial post-seismic response at the studied stations, $uj = |Uj| / \max\{|Ui|\}_{i=1}^{Nstn}$ for $j=1,..,N_{stn}$. In order to better identify the GPS sites that are most affected by the slip on the fault (i.e. near field stations) we consider a local reference frame with origin in the center of the rectangular plane used for the forward model. We define the horizontal plane by the x-axis parallel to the fault strike and the y-axis perpendicular to it. In Figure S10b we plot g (blue) and u (orange) with respect to the distance (from the origin) normalized to a characteristic length for x-axis (the half length of the fault trace, i.e. 30 km) and the y-axis (two times the depth of fault, i.e. 20 km). This normalization is chosen to take into consideration not only the main deformation signal along the extensional direction, but also a possible heterogeneous elastic response along the strike direction due to the complex faults system involved. We observe that the two signals show spatial decays that differ from each other for normalized distances greater than 2. For such distances u is systematically higher than the elastic response g, suggesting that the displacement recorded at these GPS sites cannot be described solely by afterslip. We therefore consider this threshold value of normalized distance equal to 2 in order to distinguish GPS sites into two groups: i) the near field group, for distances less than the threshold value and ii) the far field group, for greater distances (Figure S10).

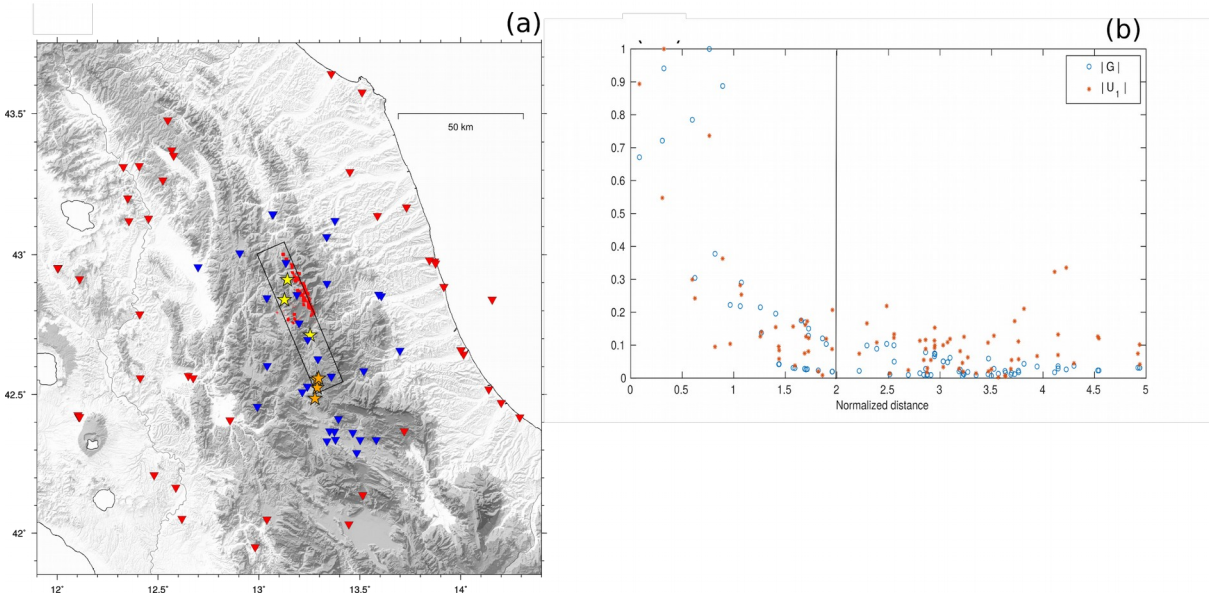

Figure S10. Panel (a) shows the near field and far field GPS stations' position (respectively blue and red triangles), the Amatrice, Visso and Norcia earthquakes (yellow stars) and the January 2017 Campotosto events (orange stars). The black rectangle represents the fault used to distinguish stations in the near field from those in the far field. Panel (b) shows g (blue circles) and u (orange dots) vs the normalized distance. The vertical line marks the threshold distance.

S7. Viscoelastic time series

In this section we show the time series obtained from the Relax simulation which considers a viscoelastic lower crust with $\eta_{lc} = 10^{17}$ Pa s. In particular we show in map the deformation pattern after 2 years from the 30th of October mainshock, and we report the results for some of the sites with a non-monotonic evolution in time.

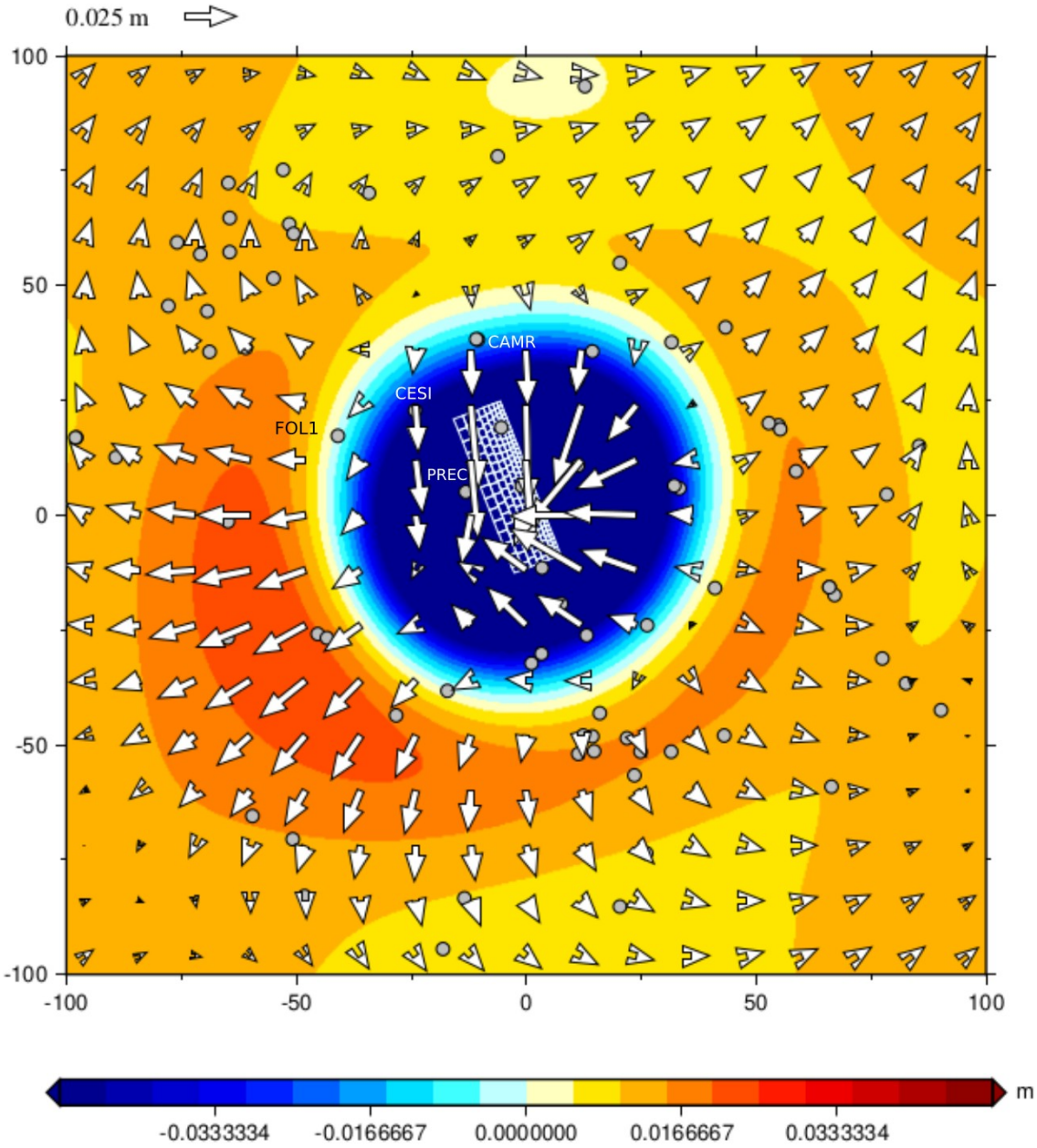

Fig S11. In map the viscoelastic displacement pattern deriving from the model with $\eta_{lc}=10^{17}$ Pa s 2 years after the Norcia mainshock. White grid shows the source fault as in Cheloni et al. (2019), grey circles mark the position of the GPS sites. Lengths along the x and y-axis are in km from the origin (lon=13.2°, lat=42.8°).

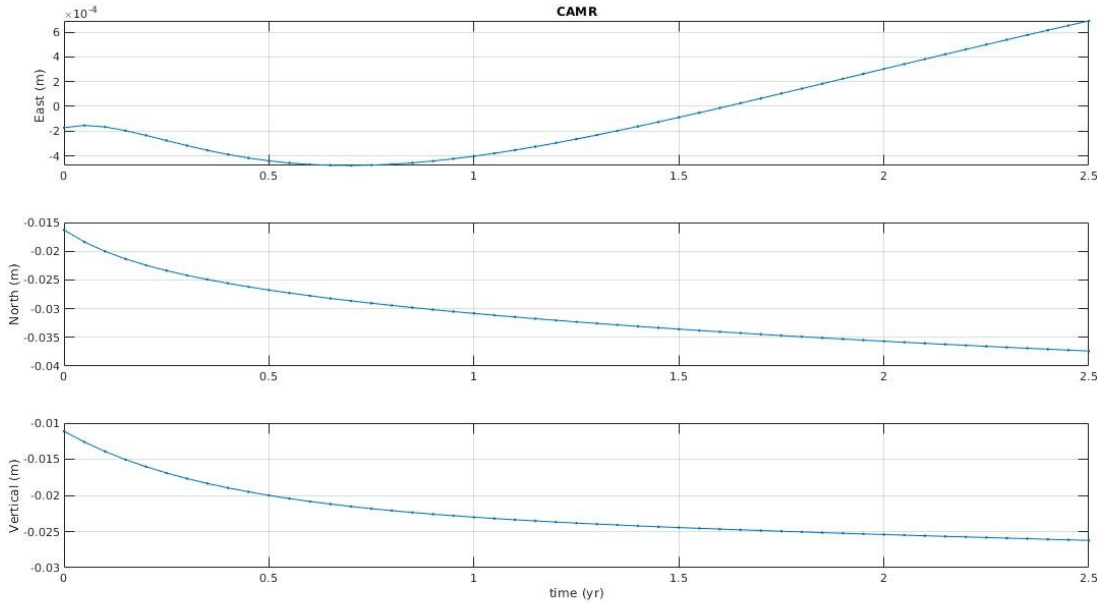

Fig S12. In figure the time series for CAMR GPS site. Displacement is in meters while time is in years measured from the Norcia earthquake epoch.

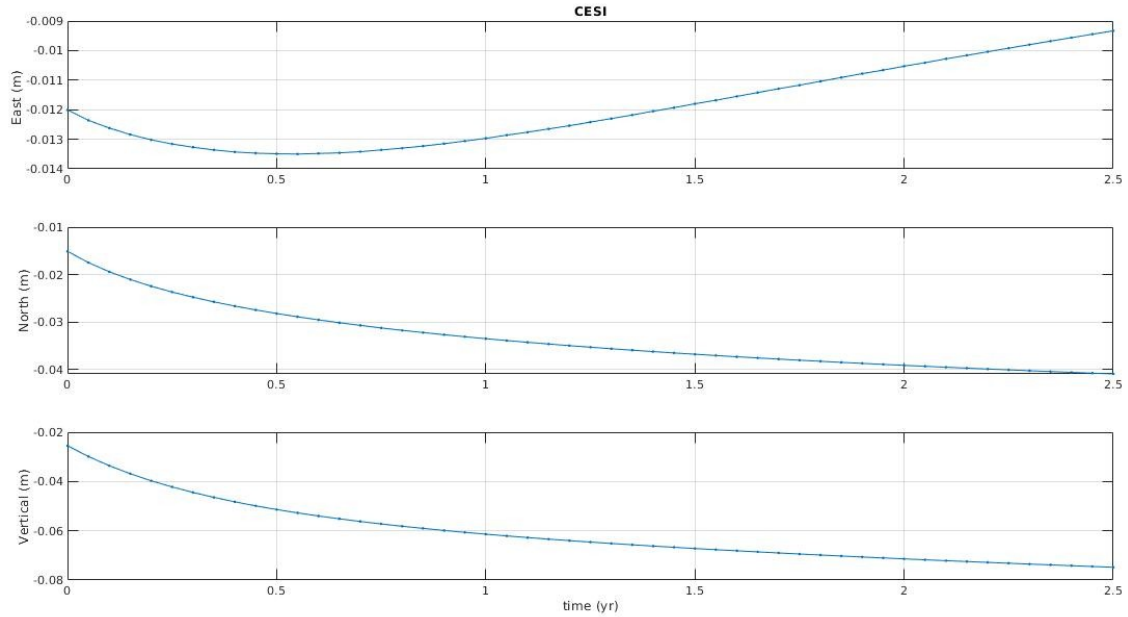

Fig S13. In figure the time series for CESI GPS site. Displacement is in meters while time is in years measured from the Norcia earthquake epoch.

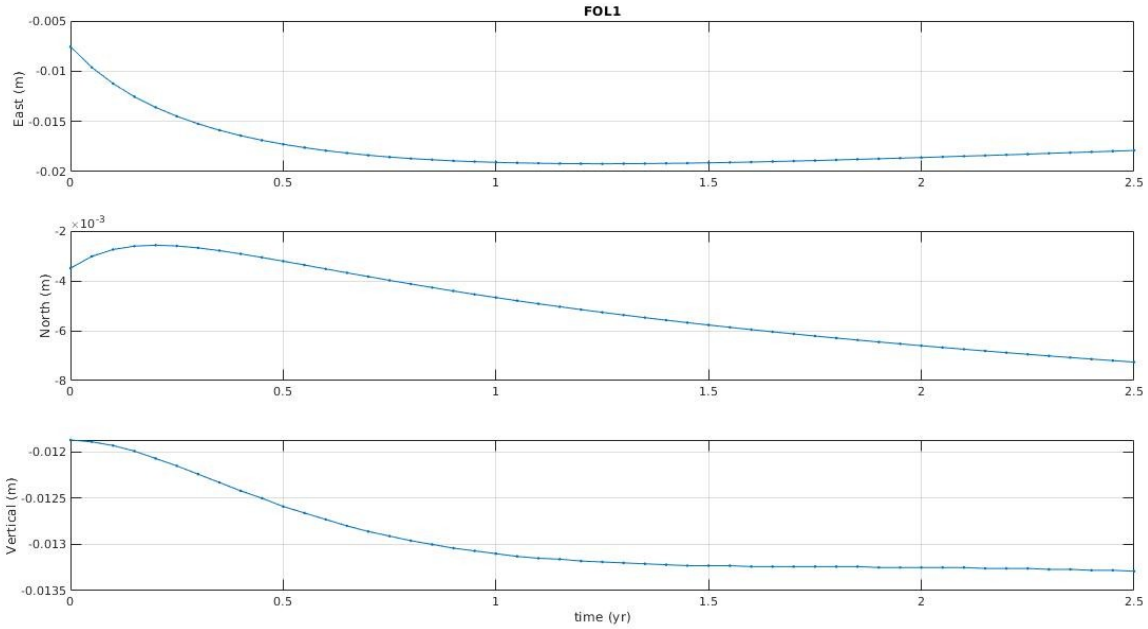

Fig S14. In figure the time series for FOL1 GPS site. Displacement is in meters while time is in years measured from the Norcia earthquake epoch.

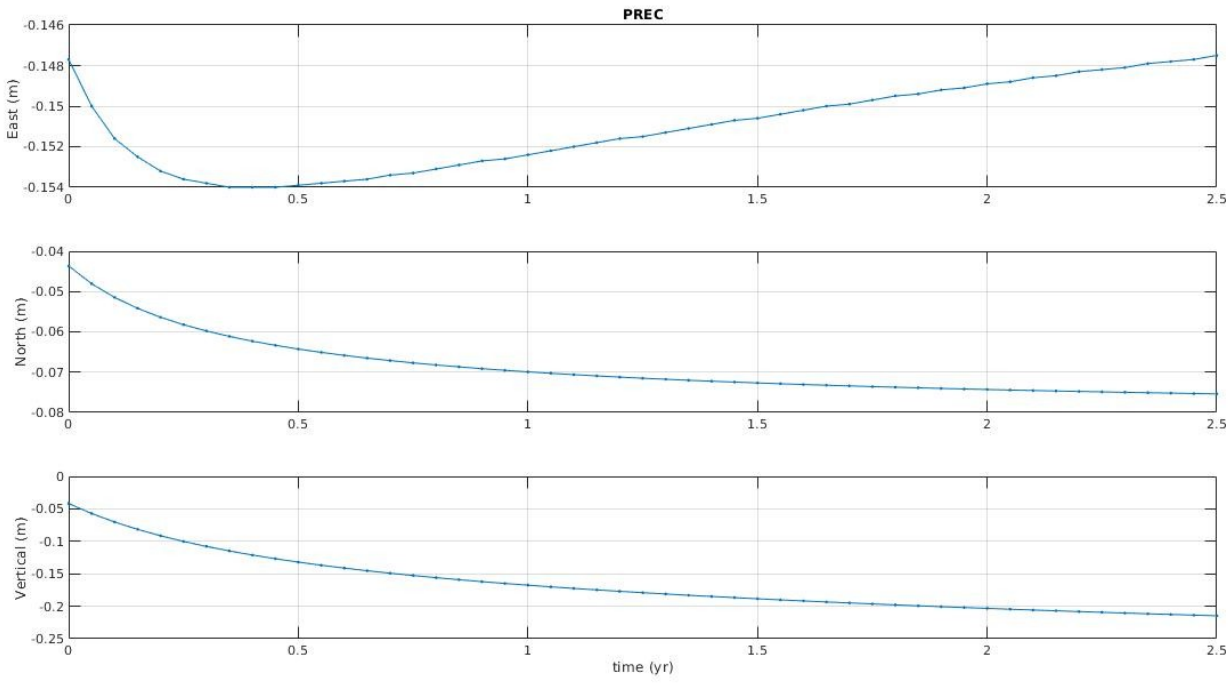

Fig S15. In figure the time series for PREC GPS sites. Displacement is in meters while time is in years measured from the Norcia earthquake epoch.

S8. Comparison between the afterslip models

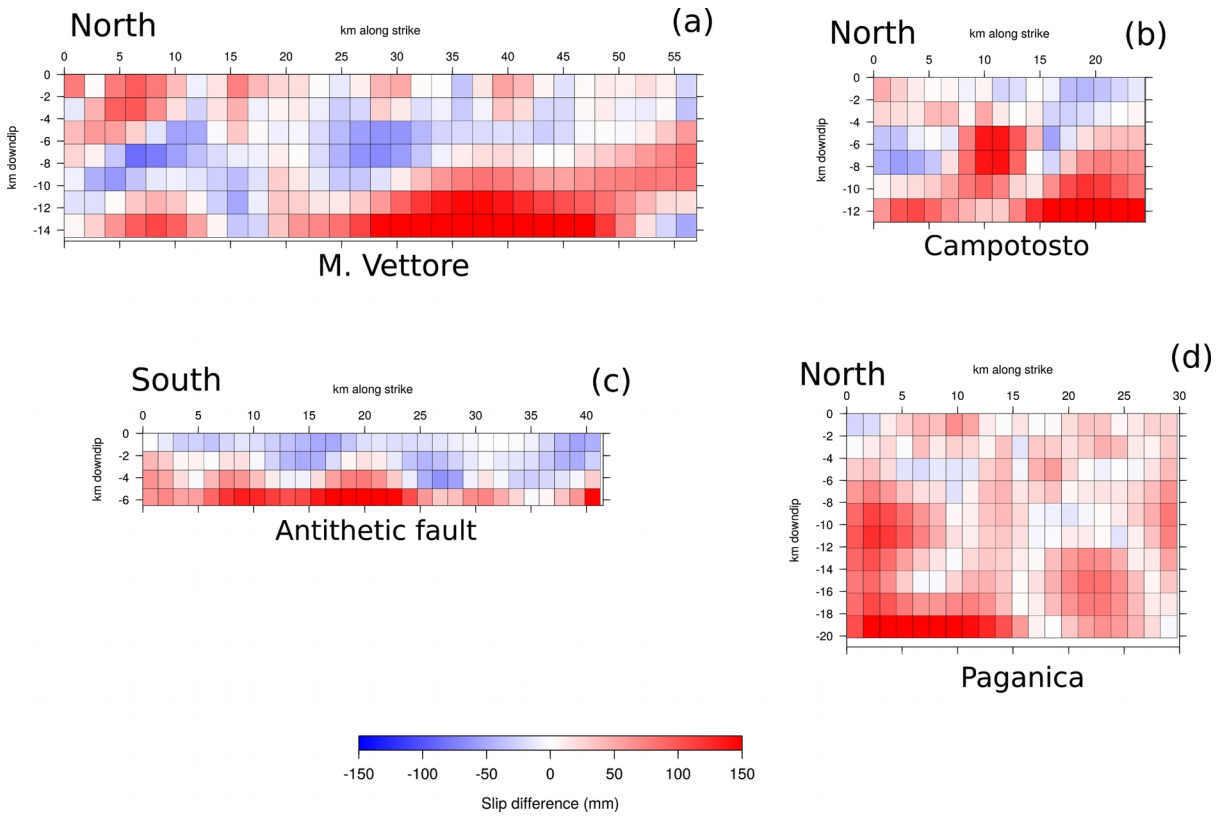

Fig S16. Figure shows the difference of slip magnitude (in mm) between the afterslip solutions of Section 4 and 4.1, main text, in a strike-dip reference system for (a) the M. Vettore, (b) the Campotosto, (c) the antithetic fault and (d) the Paganica fault.

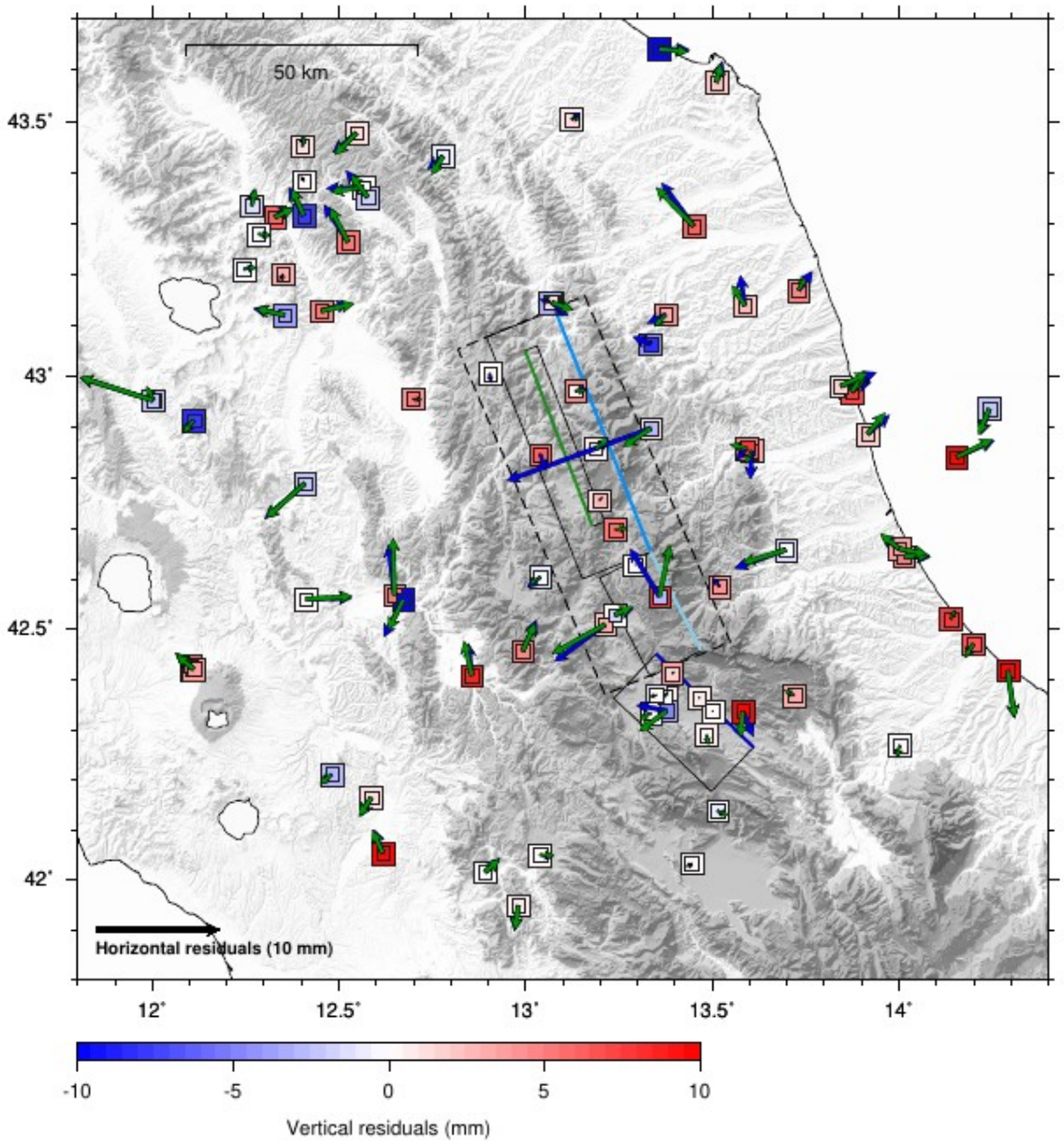

Fig S17- In map the residuals between the observed and the modeled horizontal (arrows) and vertical (squares) components of the post-seismic cumulative displacement are shown. Blue arrows and inner squares are for the model without the shear zone; green arrows and outer squares for the model with the shear zone included.

Model	$WRMSE^{TOT}$ (mm)	$WRMSE^{E}$ (mm)	$WRMSE^{W}$ (mm)	$WRMSE^{N.F.}$ (mm)
Section 4	429	181	181	67
Section 4.1	405	151	180	74

Tab S3. Weighted root mean square error (WRMSE) for the two afterslip models described in Section 4 and 4.1, main text. WRMSE are computed on the cumulative post-seismic displacement in the time span 25th of August 2016 - 2019 on the whole dataset ($WRMSE^{TOT}$), on the two subsets of GPS stations east and west of the fault system (respectively $WRMSE^{E}$ and $WRMSE^{W}$) and on the near field GPS stations ($WRMSE^{N.F.}$).

S9. Coulomb Failure Function variation

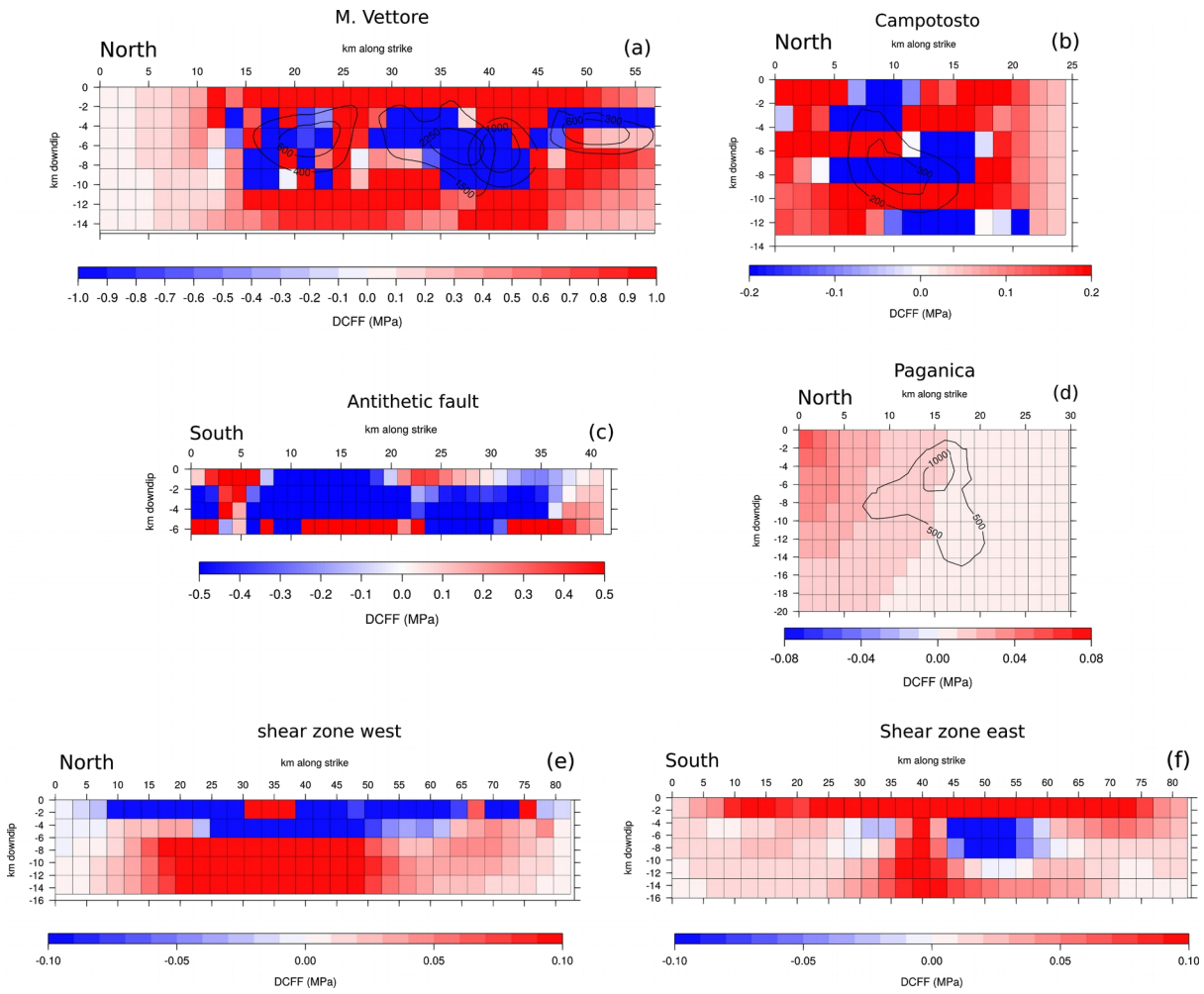

Fig S18. The Coulomb failure function variation (DCFF) on the M. Vettore fault (a), Campotosto fault (b), antithetic fault (c) , Paganica fault (d), western and easter side of the shear zone (e) and (f), related to the main events of the 2016-2017 sequence (Section 1, main text) as modeled by Cheloni et al. (2017, 2019, 2019a). Co-seismic contours on the M.

Vettore fault are from (Cheloni et al., 2017, 2019), on the Campotosto fault from (Daniele Cheloni et al., 2019), on the Paganica fault are from (Gualandi et al., 2014). Note the different scale below each fault plane (units of MPa).